Design of a linear cascade test section for NICFD experiments in the ORCHID facility

Master Thesis Aerospace Engineering

Gerwin van den Heuvel

Delft University of Technology

TU Delft

Design of a linear cascade test section for NICFD experiments in the ORCHID facility

by

Gerwin van den Heuvel

to obtain the degree of Master of Science
at the Delft University of Technology,
to be defended publicly on 10 October, 2025 at 9:30.

Student number:	5004888	
Project duration:	January 7, 2025 – Octobr 10, 2025	
Thesis committee:	Dr. ir. A. Cappiello,	TU Delft, Supervisor
	Dr. ir. M. Pini,	TU Delft, Chair
	Dr. ir. A. H. van Zuijlen,	TU Delft, Examiner

Cover: Mach number contour of flow through the linear cascade test section

An electronic version of this thesis is available at: `http://repository.tudelft.nl/`.

Data and tools produced for this work are stored in the research repository of the Propulsion & Power Group.

TU Delft

Preface

Before starting this journey, I had never heard of Organic Rankine Cycle heat recovery and I had only glanced at the *ORCHID* facility during a different project. Although I wondered about its purpose, I quickly moved on. Little did I know that I would spend nine months researching the design of a new test section for this facility. I am very grateful to have had the opportunity to learn so much about this amazing topic. I am even more grateful for all the people who supported me throughout this process, without whom I would not have been able to successfully complete this work.

First of all, I would like to thank my daily supervisor Dr. Alessandro Cappiello for his guidance throughout this project. Thank you for always being available with valuable advice, feedback, and fresh insights, without which I would not have been able to create this work.

I also thank my supervisor, Dr. Matteo Pini, for introducing me to the topic of this thesis and entrusting me with it. I am also very grateful for your guidance and feedback, especially on the research goals and approach.

In addition, I want to thank Dr. Adam Head for taking the time to sort through a large amount of files to provide me valuable data and literature for my work, for sharing some of his extensive experience with the ORCHID facility, and for giving me a tour of the facility. In addition, my thanks go out to Matteo Majer and Evert Bunschoten for helping me resolve the issues I ran into when working on the SU2 simulations.

Furthermore, I want to express my gratitude to the members of the examination committee for taking the time to evaluate this work.

Finally, a heartfelt thank you to my loving girlfriend Fleur for supporting and motivating me throughout my studies and for providing feedback on this report. Thank you to my family for their continuous support. Lastly, I want to thank my friends, most of whom also worked tierlessly besides me on their own theses, for their support and much needed distractions.

Gerwin van den Heuvel
Delft, September 2025

Abstract

Reducing primary energy consumption is crucial to lower greenhouse gas emissions, limit global warming, and improve energy independence. Beyond cutting demand, improving power plant efficiency by using waste heat recovery systems can further reduce primary energy use. Organic Rankine Cycle (ORC) systems can recover energy from low temperature sources, such as industrial waste heat or geothermal heat, using organic fluids with low boiling points. ORCs can also recover heat from internal combustion engines, but for transport applications, they must be miniaturised (mini-ORCs). For this, high pressure ratio single-stage turbines are used to achieve the required power density. However, high pressure ratios in combination with low speed of sound in organic fluids result in supersonic flows, causing trailing edge shocks, which lower turbine efficiency. Optimising turbine design for supersonic organic flows is essential for large-scale and efficient mini-ORC deployment.

Improving ORC turbine efficiency requires design tools and guidelines validated for the nonideal compressible fluid dynamics (NICFD) conditions of organic fluids, which arise due to the high molecular complexity and density of these fluids. To develop these, the Propulsion & Power research group at Delft University of Technology has built the Organic Rankine Cycle Hybrid Integrated Device (*ORCHID*) test rig. Following initial studies using a planar converging-diverging nozzle test section, the next step is to test a stator row to investigate complex flows containing wakes and trailing-edge shocks. The objective of this thesis is to determine an optimal linear stator cascade test section design for the *ORCHID* facility, to allow experiments to: *(1)* develop and validate stator design guidelines and models, *(2)* validate the capacity of numerical models to accurately predict flow features such as boundary layer transition and shock-boundary layer interaction, and *(3)* to validate modelling assumptions such as adiabatic flow.

To achieve this objective, this work starts with a review of the literature on existing NICFD experiments. This includes a comprehensive review and selection of measurement techniques, based on the experimental goals. Next, cascade geometries are designed based on three expansion conditions with increasingly nonideal fluid properties. To ensure a fair loss comparison between different cascade designs, constant non-dimensional properties are set, including: Reynolds number, Mach number, and trailing edge-to-pitch ratio. Finally, CFD analyses are performed to investigate flows through both infinite cascade and finite test section cascade. The results are first used to compare flows through infinite cascades in order to investigate the effect of nonideality on the flow structure. Then, finite cascade flows are compared to their infinite cascade counterparts, in order to determine the optimal number of passages and outlet geometry for the test section. During this final analysis, it is critical to determine whether the cascade blade loading in the centre passage (measurement passage) resembles that of an annular (infinite) cascade in order to achieve the first experimental goal mentioned previously.

The results of infinite cascade simulations show a reduction in the cascade exit flow angle with increasing nonideality, presumably caused by the increase in fluid density. The results of the analysis of the test section show a strong influence of the bottom tailboard behind the cascade on the exit flow angle. Incorrect alignment of this tailboard can cause the trailing edge shockwaves to have a different angle compared to the infinite cascade, changing the blade loading. Increasing the number of passages from five to seven does not seem to improve the resemblance between the centre passage blade loading and the infinite cascade blade loading. Interestingly, the blade loading resemblance to the infinite cascade appears to worsen in passages further away from the bottom tailboard, suggesting that a three-passage cascade might perform better than a five-passage cascade. Critically, the strong influence of the angle of the bottom tailboard on the cascade blade loading does not allow rotation of this tailboard to redirect the wall-reflected shock waves.

Contents

List of Figures

List of Tables

Nomenclature

Abbreviations

Abbreviation	Definition
ASTER	Asymmetric Shock Tube for Experiments on Rarefaction waves
BZT	Bethe, Zel'dovich, Thompson (fluid)
cp	critical point
CEoS	Cubic Equation of State
CFD	Computational Fluid Dynamics
CLOWT	Closed Loop Organic vapour Wind Tunnel
DES	Detached-Eddy Simulation
EoS	Equation of State
FAST	Flexible Asymmetric Shock Tube
GWP	Global Warming Potential
HEoS	Helmholtz-energy Equation of State
HMC	High Molecular Complexity (fluid)
HWA	Hot-Wire Anemometry
iPRSV	improved Stryiek-Vera Peng-Robinson
ICL	Imperial College London
LDV	Laser Doppler Velocimetry
LES	Large-Eddy Simulation
LMC	Low Molecular Complexity (fluid)
LUT	Look-Up Table
MEoS	Multi-parameter Equation of State
MoC	Method of Characteristics
NICFD	Non-Ideal Compressible Fluid Dynamics
NIST	National Institute of Standards and Technology
NRBC	Non-Reflective Boundary Condition
ORC	Organic Rankine Cycle
ORCHID	Organic Rankine Cycle Hybrid Integrated Device
PR	Peng-Robinson
PIV	Particle Image Velocimetry
ps	pressure-side
RANS	Reynolds-Averaged Navier-Stokes
REFPROP	Reference Fluid Thermodynamic and Transport Properties Database
SF	Safety Factor
ss	suction-side
TROVA	Test Rig for Organic Vapours

Symbols

Symbol	Definition	Unit
A	*(1)* Helmholtz free energy	[J]
	(2) Area	[m^2]
a	*(1)* Molecular attraction parameter	[–]
	(2) Specific Helmholtz energy	[$\mathrm{J \cdot mol^{-1}}$]
b	Co-volume parameter	[–]
C	Stator vane chord length	[m]
C_{ax}	Stator vane axial chord length	[m]
c	*(1)* Speed of sound	[$\mathrm{m \cdot s^{-1}}$]
	(2) Speed of light	[$\mathrm{m \cdot s^{-1}}$]
	(3) Absolute flow velocity	[$\mathrm{m \cdot s^{-1}}$]
	(4) Specific heat	[$\mathrm{J \cdot kg^{-1} \cdot K^{-1}}$]
c_0	Speed of light in vaccum	[$\mathrm{m \cdot s^{-1}}$]
h	Enthalpy	[J]
h_{bl}	Blade height	[m]
K	Gladstone-Dale constant	[$\mathrm{m^3 \cdot kg^{-1}}$]
M	Mach number	[–]
$\dot{m}$	Mass flow rate	[$\mathrm{kg \cdot s^{-1}}$]
n	Refraction index	[–]
n_{pass}	Number of (cascade) passages	[–]
P	Pressure	[$\mathrm{kg \cdot m^{-1} \cdot s^{-2}}$]
p	Stator cascade pitch	[m]
$\dot{Q}$	Thermal power	[$\mathrm{kW_{th}}$]
R	Specific gas constant	[$\mathrm{J \cdot K^{-1} \cdot mol^{-1}}$]
Re	Reynolds number	[–]
S	Stator vane pitch	[m]
s	Entropy	[$\mathrm{J \cdot K^{-1}}$]
t	Stator trailing edge thickness	[m]
T	Temperature	[K]
U	Internal energy	[J]
v	Velocity	[$\mathrm{m \cdot s^{-1}}$]
w	Width	[m]
x	x-direction (aligned with inflow direction	[–]
y	*(1)* y-direction	[–]
	(2) First cell height	[m]
Z	Compressibility factor	[–]
α	*(1)* Stator flow angle	[°]
	(2) Reduced Helmholz energy	[–]
β	*(1)* Stator blade metal angle	[°]
	(2) Pressure ratio	[–]
γ	Specific heat ratio	[–]
Γ	Fundamental derivative of gas dynamics	[–]
δ	Reduced density	[–]
η_{N}	Profile efficiency	[%]
μ	Dynamic viscosity	[$\mathrm{N \cdot s \cdot m^{-2}}$]
ν	Specific volume	[$\mathrm{m^3 \cdot kg^{-1}}$]
ρ	Density	[$\mathrm{kg \cdot m^{-3}}$]
σ	Solidity	[–]
τ	Inverse reduced temperature	[–]
Φ_{n}	Stator blade stagger angle	[°]
ϕ_{a}	Design flow angle	[°]
ϕ_{tb}	Tailboard angle	[°]

Subscripts

Subscript	Definition
1	Stator enterance (station)
2	Stator exit (station)
2D	2-dimensional
3D	3-dimensional
5pass	5-passage cascade
7pass	7-passage cascade
8	ORCHID regenerator outlet station
avg	Average
a	End of nozzle curve
c	Critical
casc	Cascade (test section)
exit	Cascade exit (directly behind the cascade)
ideal	”Ideal” expansion condition
in	Input
inlet	Test section inlet (station)
max	Maximum
min	Minimum
nonid	”Nonideal” expansion condition
nonm	”Nonmonotonic” expansion condition
noz	Nozzle (test section)
opt	Optimal
outlet	Test section outlet (station)
o	Start of nozzle curve (at throat)
p	Constant pressure process
PE	Post-Expansion
r	Reduced
s	Isentropic process
sat	Saturation
t	Total
te	Trailing edge
th	Throat (station)
ts	Total-to-static
v	Constant volume process

Superscripts

Superscript	Definition
$*$	Nozzle curve point before shifting with pitch
o	Ideal gas
r	Residual real gas component

1

Introduction

It is becoming increasingly important to reduce primary energy consumption. In the first place, reducing energy consumption will directly reduce greenhouse gas emissions, limiting global warming. Secondly, lower energy consumption will reduce energy imports, improving energy independence. In addition to lowering energy demand, increasing the efficiency of power plants will reduce primary energy consumption. One way of achieving this is to use waste heat recovery systems to convert waste heat into usable energy.

A key technology to recover waste energy from low temperature sources like industrial and geothermal heat are Organic Rankine Cycle (ORC) systems. These systems employ organic working fluids that have high molecular complexity and density. Critically, organic fluids have a low boiling point, which allows ORCs to recover energy from low-temperature heat sources.

Another application of ORCs is the heat recovery of internal combustion engines to reduce energy consumption in the transportation sector. For this application, ORCs must be miniaturised to be transportable. Mini-ORCs use high pressure ratio single-stage turbines in order to reach the required power density. The combination of a high pressure ratio and the low speed of sound in organic fluids results in supersonic flows in the turbine stator cascade. This causes trailing edge shock waves behind the stator vanes. These shocks affect the rotor flow field, significantly reducing turbine efficiency. For large-scale implementation of mini-ORCs, it is important to optimise the turbine design for supersonic flows of organic compounds to increase the turbine efficiency, directly improving the system efficiency.

1.1. Motivation

Improving the efficiency of ORC turbines requires reliable design methodologies, tools, and guidelines. However, readily available design methods and computational fluid dynamics (CFD) solvers validated for air have not yet been fully validated for ORC turbines. This is because organic fluids used in ORCs often operate in nonideal fluid dynamics (NICFD) domains. This means that conventional CFD solvers based on the ideal gas assumption are not applicable. Developments have been made on commercial and academic CFD solvers that allow numerical analysis of NICFD flows by implementing alternative equations of state to the ideal gas model. These include Peng-Robinson (PR)[1] and more accurate models of fluid property databases like *REFPROP*[2] and *CoolProp*[3].

Validation of these tools is critical to achieve reliable designs for ORC turbines. However, due to the challenging conditions associated with NICFD flows, experimental investigations to validate these CFD models are scarce. Challenges include high operating temperature and pressure, the need to adapt measurement techniques for organic vapour flows, and the fact that some organic fluids can be toxic or have a high Global Warming Potential (GWP). Despite these challenges, there are several facilities where NICFD experiments are performed.

To date, the Propulsion & Power group at Delft University of Technology has already made significant progress in the field of NICFD experiments. The first experiments were performed using a planar nozzle

test section in the specially designed ”Organic Rankine Cycle Hybrid Integrated Device” (*ORCHID*) test rig, discussed by Head [4]. The *ORCHID* is one of the most capable devices for NICFD experiments currently in operation. It can be used to perform fundamental experiments through a static test section and to perform complete turbine experiments, making it a hybrid device.

Bills [5], Hariharan [6], and Vello [7] developed a validation infrastructure for the open source CFD solver *SU2* and used the experimental data from the planar nozzle experiments to perform the first validation. The validation pathway envisioned in their work can be seen in Figure 1.1.

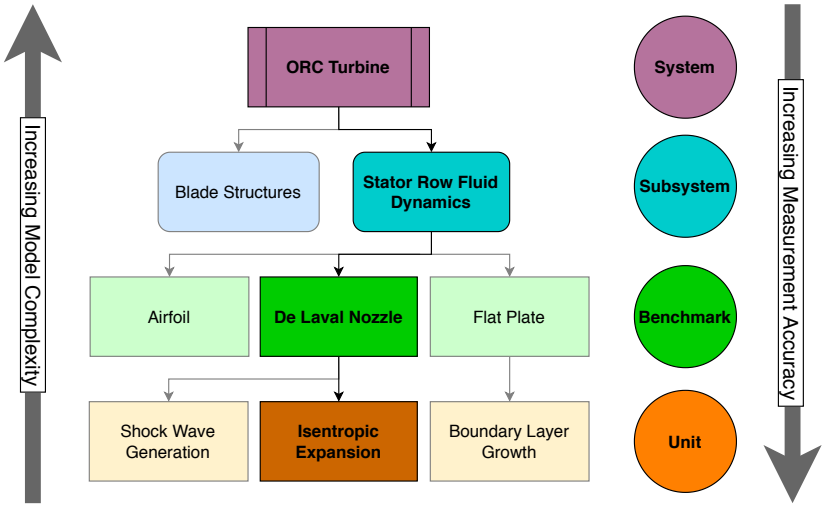

Figure 1.1: Breakdown of a turbo machine system with the validation route highlighted[5]

The pathway shows that the next step after the De Laval nozzle is to perform experiments on a stator row. This will allow for the investigation of a more complicated flow field, including wake effects and shock waves emanated by the stator trailing edge, which are not present in the nozzle tests. Furthermore, Rinaldi, Pecnik, and Colonna [8] show that stator losses in highly loaded ORC turbines account for approximately two-thirds of total turbine losses. This shows that efficient stator design is critical.

In addition to generating validation data for CFD tools, experiments using a stator cascade can also provide crucial data for the development or validation of stator design tools and guidelines. This requires the evaluation of different stator vane geometries. Experiments are also needed to validate modelling assumptions like the commonly used adiabatic flow assumption, as well as the ability of CFD tools to capture certain flow features in NICFD flows such as laminar to turbulent transition as suggested by Head [4].

In addition to ORC turbines, a stator cascade test section can also be used to evaluate stator vane designs for rocket engine turbo pumps. Although these pumps operate with different working fluids, relevant qualitative insights can still be gathered from these experiments. Due to the low speed of sound in organic fluids, it is comparatively easy to reach supersonic stator conditions, which are relevant for rocket turbo pumps. For rocket engines, mass, size, complexity, and cost drive turbo pump designs to minimise the number of stages. This, in turn, results in maximising the work extraction of a single turbine stage. In turbo pumps, the amount of work that can be extracted from a certain mass flow by one stage (called specific work) is dictated by the peripheral speed multiplied by the change in tangential velocity[9]. Maximising the specific work becomes important when mass flow rate must be minimised. This is the case for open cycle engine architectures, since these subtract fuel mass flow rate from the engine to operate. Essentially, wasting it. The risk of flow detachment dictates the maximum flow deviation. This leaves increasing the flow velocity as the only means of further increasing the specific work. This leads to the use of supersonic turbines in rocket engines.

The motivations mentioned above therefore call for the design and construction of a supersonic turbine stator-vane cascade for the *ORCHID* facility. Specifically, a linear cascade should be designed because it is most accessible to a wide range of measurement techniques.

1.2. Research Objective and Approach

Based on the motivations described above, the following research question is formulated:

What is the optimal design of a test section to investigate NICFD flows in a linear stator-vane cascade using the ORCHID facility?

To answer this research question, the following subquestions must be answered:

1. *What is the best measurement approach to acquire validation data which is unaffected by wall-reflected shock waves in on- and off-design conditions?*

   To awnser this question, first, the flow properties of interest must be identified. Then, the preferred measurement technique for each of these properties needs to be selected based on criteria such as cost, ease of implementation, and measurement uncertainty.

2. *How to design different linear stator cascades for different thermodynamic conditions, while maintaining the same blade height, Reynolds number and Mach number?*

   Since multiple thermodynamic fluid behaviours are of interest, multiple experimental conditions are needed and stator geometries must be designed. However, the test section is constrained to one blade height to avoid time-consuming modifications. Furthermore, since the cascade losses depend on the nondimensional Reynolds number, Mach number, and trailing edge thickness to pitch ratio, these must be similar between the different experiments. In this way, a comparison between the different experiments can be made. Finally, it must be ensured that none of the designs exceed the mass flow rate that can be provided by the *ORCHID* facility. Thus, a procedure must be found to design the stator geometries with these requirements.

3. *What is the optimal number of flow passages to achieve flow periodicity and minimise the effect of wall-reflected shock waves?*

   The *ORCHID* facility has limited thermal power. This means that for a given flow condition, there is a maximum mass flow rate. Since the flow is choked in the throat(s) of the cascade, for a given number of passages, this implies a maximum throat area. Thus, the blade height must decrease as the number of passages increases. So, to find the optimal number of passages, the flow periodicity and the effects of blade height on the flow must be investigated for a varying number of blades.

1.3. Report Outline

This report is structured as follows. After this introductory chapter, chapter 2 contains a comprehensive literature review containing the required theoretical background as well as the current state of the art of NICFD experiments. Then, chapter 3 describes the methodology used to design the linear cascade test section, as well as the numerical analysis approach. The results of this analysis are investigated in chapter 4, including a discussion of the findings. Finally, chapter 5 summarises the conclusions that are drawn from this investigation and formulates answers to the research questions. This final chapter ends with a list of recommendations for future research.

2

Literature Review

This chapter contains the theoretical knowledge required for the research within this report, collected from scientific literature. First, section 2.1 discusses the general design aspects of supersonic stator cascades, as well as the flow structure generated within and behind these cascades. Then section 2.2 contains the basic theory behind nonideal compressible fluid dynamics. This is followed by a discussion on numerical modelling approaches for NICFD flows in section 2.3.

In addition to theoretical background, this chapter also provides an overview of the current NICFD experiments and the facilities in which they are performed, this is presented in section 2.4. The measurement techniques used in the NICFD experiments are investigated in section 2.5. Finally, the existing work towards the goal of developing a linear stator cascade test section for the *ORCHID* facility is summarised in section 2.6.

2.1. Supersonic Turbine Stators

The main purpose of stator cascades in turbines is to deflect the flow to introduce circumferential velocity to rotate the rotor. In this way, the rotor can convert the energy in the flow to mechanical work. In addition to this, supersonic stators accelerate the flow to supersonic speeds, in order to extract more work in a single stage. This is done by shaping the stator vanes so the passage between them forms a converging-diverging nozzle. A schematic of a single supersonic turbine stage can be seen in Figure 2.1, including its velocity triangles. This research focusses only on the stator.

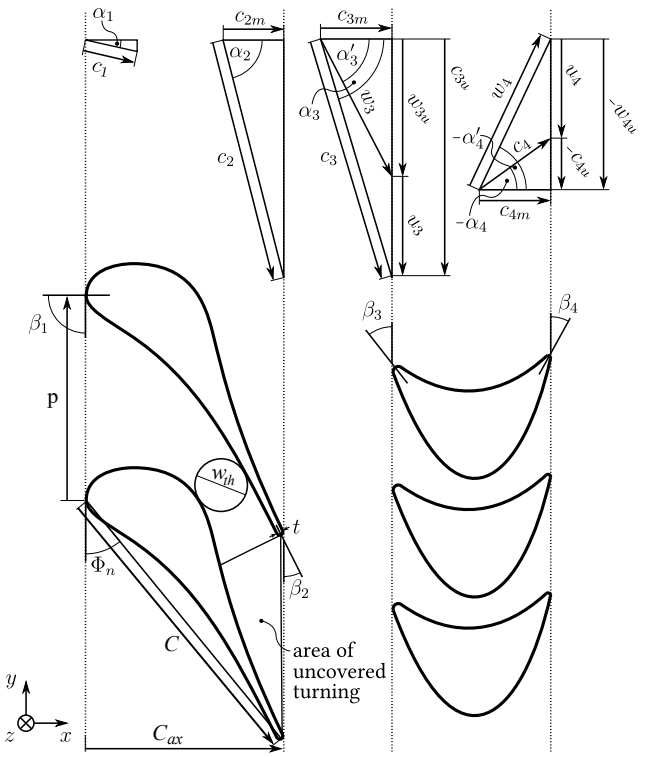

Figure 2.1: Schematic of a supersonic turbine stage, adapted from [9]

The following nomenclature is used:

- α_1 and α_2 are the stator in- and out-flow angles;
- c_1 and c_2 are the absolute in- and out-flow velocities;
- β_1 and β_2 are the stator entrance and exit blade metal angles;
- Φ_n is the stator stagger angle;
- w_{th} is the stator throat width;
- p is the stator pitch;
- t is the stator trailing edge thickness;
- C is the stator chord length;
- C_{ax} is the stator axial chord length.

The schematic shows a cross section of a stator and rotor row in a supersonic turbine. The flow entering the stator is (almost) aligned with the x-axis. Then, the stator deflects the flow and increases its velocity. The flow then enters the rotor, which converts the kinetic energy in the flow into mechanical energy. The schematic also shows that the stator blades are spaced by the pitch p. The space between the stator vanes forms the passage with the converging-diverging nozzle shape. Finally, the flow reaches the area of uncovered turning, where the flow is bound by only one blade.

While delivering high specific power, the drawback of supersonic turbines is the increase in losses as a result of the occurrence of shock waves. These shock waves cause an increase in the trailing edge losses, while the boundary layer losses reduce with increasing Mach numbers because of the reduction of the Reynolds number. This causes trailing edge losses to dominate total stator profile losses[10]. Furthermore, trailing edge losses increase roughly linearly with trailing edge blockage, resulting in trailing edge losses dominating total turbine loss for turbines with thick trailing edge stator blades (needed on cooled blades)[10].

The general flow pattern at the trailing edge of a supersonic stator vane can be seen in Figure 2.2. When the trailing edge curvature is reached, the flow on both the suction and pressure sides will separate, creating a low-pressure region behind the trailing edge. This region is called the base region and is bound by the separated shear layers. The change in flow direction due to separation causes expansion waves to form, originating at the separation points. The shear layers will meet somewhere behind the trailing edge, called the confluence region. The combined shear layers will form a wake behind the stator vane. When the shear layers meet, they deflect in one common direction. This change in direction causes compression shocks that originate in the confluence region. The shock on the pressure side of the blade propagates to the suction side of the adjacent blade, deflecting on the surface. This has a large effect on its pressure distribution[10]. The other shock wave will propagate into the flow, causing dynamic effects when it meets the rotor blades. The shock-expansion wave system resulting from these propagations can be seen in Figure 2.3. It can be seen that there will be a pattern of alternating expansion and compression waves in the wake of the supersonic stator cascade.

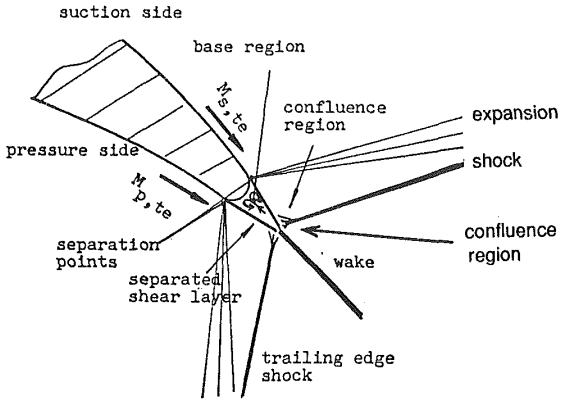

Figure 2.2: Structure of supersonic trailing edge flow[10]

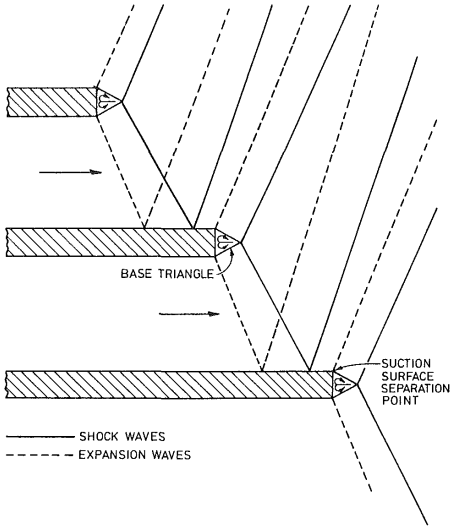

Figure 2.3: Shock-expansion wave system behind a supersonic cascade[10]

Downstream of the stator cascade, the created shock pattern will start to interact with the rotor. This will have multiple detrimental effects. First, these complex dynamic effects will add to the turbine losses. Furthermore, periodic interaction of the rotor blades with shock waves will cause cyclic loading, which will reduce the fatigue life of the rotor blades[9, 8]. Finally, there is the risk of shock-induced boundary layer separation in the rotor[11]. Improving the stator vane design and reducing the intensity of the trailing edge shock waves in the wake will help alleviate these effects.

To investigate these effects, Giovannini et al. [12] performed a three-dimensional unsteady RANS simulation of the stator-rotor flow interaction in a supersonic axial turbine stage. The time evolution of the flow field can be seen in Figure 2.4, where each frame contains a different moment in time indicated by the fraction of time passed over the time it takes for a rotor blade to pass a stator passage. Here, the trailing edge shocks of the stator vane are labelled A and B. Then, the pressure-side shock (B) reflects on the stator vane below it and forms a reflection shock, highlighted in the second instance. In the same instance, direct shock A reflects on the rotor, creating a reflection shock (D). This shock travels upstream and affects the suction side of the stator vane. The shock wave can travel upstream because, while the total flow velocity behind the stator cascade is supersonic, the axial flow velocity is subsonic. The reflection shock thus also influences the pressure distribution on the stator.

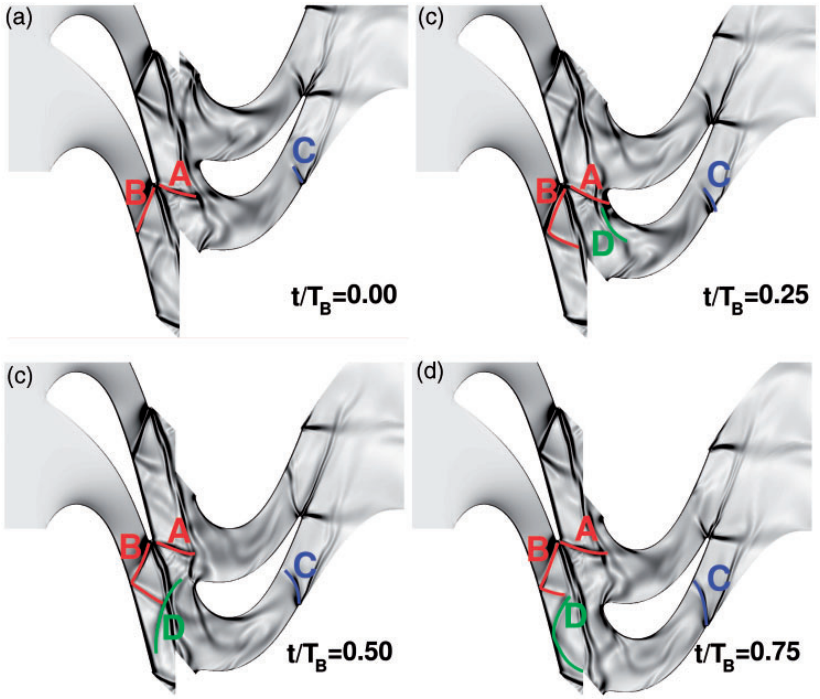

Figure 2.4: Unsteady RANS simulation time evolution of the flow field in a supersonic axial turbine stage[12]

2.2. Nonideal Compressible Fluid Dynamics

As the name suggests, Nonideal Compressible Fluid Dynamics (NICFD) investigates fluids that are both compressible and nonideal. A compressible flow is defined as a flow in which the density changes significantly. The assumption of a compressible ideal flow is often sufficient for many aerodynamic problems, as the fluid is air. These problems can be modelled numerically with the conservation equations (see section 2.3) by introducing an Equation of State (EoS) to close the system. This is needed since the density terms in the equations cannot be assumed constant for compressible flows. Thus, an equation is needed that relates the thermodynamic properties of the fluid. For ideal gases, this can be done with the ideal gas law $P = \rho \mathrm{R} T$, which relates the pressure P to the fluid density ρ and temperature T using the specific gas constant R. The ideal gas law assumes a constant specific heat[4].

The ideal gas law fails when intermolecular forces become significant. Van der Waals[13] was the first to derive a thermodynamic model that describes multiple phases: liquid, saturated, and vapour[4]. The van der Waals equation

$$P = \frac{\mathrm{R} T}{\nu - b} - \frac{a}{\nu^2} \tag{2.1}$$

is derived from the ideal gas law and depends on the co-volume parameter b and the molecular attraction parameter a, with $\nu = \rho^{-1}$ being the specific volume. Head [4] states that this equation of state is rather inaccurate (although theoretically sound), but that a large number of concurrent models were derived from it for simple substances.

To investigate nonideal fluid dynamics, it is critical to identify when a fluid is considered nonideal. As stated previously, nonideality occurs when intermolecular forces become significant. Thus, the conditions where these forces become significant must be determined.

A parameter that is often used to quantify nonideality, as discussed by Head [4], Guardone et al. [14] and Wiesche [15]) is the compressibility factor Z, which is defined from the ideal gas law as

$$Z = \frac{P \nu}{\mathrm{R} T}. \tag{2.2}$$

This definition asserts that an ideal gas has a compressibility factor of $Z = 1$.

Both Head [4] and Wiesche [15] state that $Z \neq 1$ is a requirement for nonideality, but not a sufficient one. The compressibility factor cannot provide information on the speed of sound change with respect to density, which defines the dynamic behaviour of the flow (called the ”fluid mechanical phenomena” by Wiesche [15]). Guardone et al. [14] differentiate between thermodynamic nonideal effects, for which compressibility factor (Z) is a measure, and gas dynamic nonideal effects.

Landau [16] derived a nondimensional parameter as

$$\frac{\nu^3}{c^2}\left(\frac{\partial^2 P}{\partial \nu^2}\right)_{\mathrm{s}}, \tag{2.3}$$

describing the curvature of isentropes in a $P\nu$-diagram, shown in Equation 2.3. Here c is the speed of sound and the subscript s indicates an isentropic process. Hayes [17] later introduced a factor of one-over-two and the symbol Γ, after which work by Thompson [18] named the parameter ”the fundamental derivative of gas dynamics”:

$$\Gamma = \frac{1}{2}\frac{\nu^3}{c^2}\left(\frac{\partial^2 P}{\partial \nu^2}\right)_{\mathrm{s}} = 1 + \frac{\rho}{c}\left(\frac{\partial c}{\partial \rho}\right)_{\mathrm{s}}. \tag{2.4}$$

For a perfect gas, $\Gamma \geq 1$. Using further thermodynamic manipulations, Thompson [18] derives more identities, including one for ideal gases as

$$\Gamma = \frac{1}{2}(\gamma + 1), \tag{2.5}$$

with $\gamma = \frac{c_{\mathrm{p}}}{c_{\mathrm{v}}}$ depicting the specific heat ratio.

Thompson [18] further showed that the Mach number will no longer increase monotonically with velocity when $\Gamma < 1$. This means that the Mach number can also decrease with increasing velocity when $M^2 > 1/(1-\Gamma)$. It can be said that in this regime, qualitative flow features remain the same as for ideal flow, but the quantitative features differ. Lastly, Thompson showed that when $\Gamma < 0$, classical qualitative phenomena in a flow reverse, meaning that Prandtl-Meyer expansion fans become compression fans and compression shocks become rarefaction (or expansion) shocks. The substances in which this is possible are called BZT fluids, after Bethe, Zel’dovich and Thompson. However, no experiment has yet shown these phenomena in reality according to Head [4].

With the two indicators for (non)ideality, fluid and domain classifications can be made. Head [4], Guardone et al. [14] and Wiesche [15] all distinguish three main regimes as listed in Table 2.1. The classical regime includes both perfect gases (sometimes called dilute gases) and dense vapours (or nonideal gases). The term dense vapour stems from the fact that intermolecular effects become more significant with higher density because of the closer proximity of the molecules. Here, Guardone et al. [14] differ slightly in terms of terminology compared to the others. This is because Head and Wiesche define a dense vapour as a fluid with $0 < \Gamma < 1$. However, they also define a dense vapour region in the PT- and Ts-diagrams. An example of these diagrams for carbon dioxide can be seen in Figure 2.5, where the axes are normalised based on the critical point (cp).

Table 2.1: Classification of gas dynamic regimes in gaseous (vapour) phase, from Head [4, p. 17] based on Thompson [18]

Γ	Possible phenomena	Classification	Soundspeed variation	Substance state
$\Gamma > 1$	Compression shocks expansion fans	Classical Compressible Fluid Dynamics	$\left(\frac{\partial c}{\partial P}\right)_s > 0$	Perfect gas
$\Gamma = 1$	Flow with $c = \text{const.}^*$	Classical nonideal Compressible Fluid Dynamics	$\left(\frac{\partial c}{\partial P}\right)_s = 0$	Gas made of molecules in states featuring $c = \text{const.}$
$0 < \Gamma < 1$	Compression shocks, Expansion fans		$\left(\frac{\partial c}{\partial P}\right)_s < 0$	Dense vapour
$\Gamma = 0$	Stationary acoustic wave*	Non-classical nonideal Compressible Fluid Dynamics	$\left(\frac{\partial c}{\partial P}\right)_s < 0$	Dense vapour of sufficiently complex molecules
$\Gamma < 0$	Rarefaction shocks, Compression fans		$\left(\frac{\partial c}{\partial P}\right)_s < 0$	

* Arguably, this type of flow is a limiting case and cannot occur in practice.

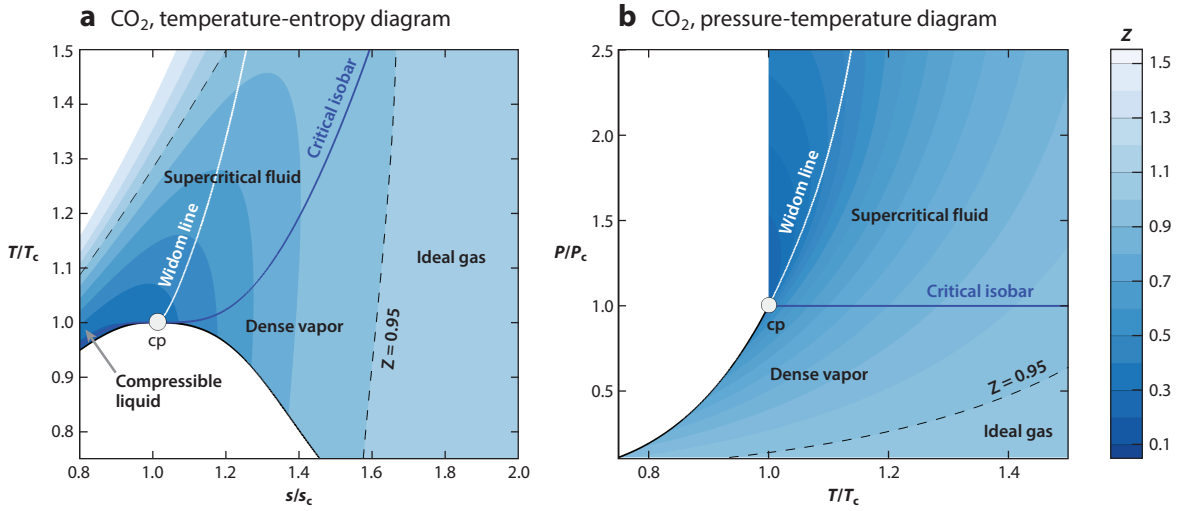

Figure 2.5: Normalised Ts and PT thermodynamic diagrams for carbon dioxide indicating critical point (cp) and the different fluid classification zones[14]

In this case, a dense vapour must have $Z < 1$, must be in the vapour state, and must be below the critical pressure. Above the critical pressure, the fluid is defined as a supercritical fluid. This means that a dense vapour has two different meanings. For this reason, Guardone et al. introduce new fluid designations based on their molecular complexity. That is, the number of degrees of freedom of a fluid molecule. This is because, in addition to density, a higher molecular complexity also increases intermolecular forces, and thus increases nonideality. In addition to the BZT fluids discussed previously, Guardone et al. presented two different designations.

First, low-molecular-complexity (LMC) fluids are distinguished. LMC fluids are fluids with a minimum fundamental derivative of gas dynamics greater than one ($\Gamma_{\min} > 1$) in the nonideal single-phase region. For these fluids, the speed of sound will always decrease on isentropic rarefaction (expansion), increase on isentropic compression and will always monotonically increase with increasing velocity, just like a perfect gas (no gas dynamic nonideal effects). However, NICFD is still applicable for these gases, as they can still differ from the ideal gas equation (so showing nonideal thermodynamic effects) in the dense-vapour region of the thermodynamic plane.

Secondly, fluids of higher molecular complexity (HMC) are fluids with $0 < \Gamma < 1$ in the nonideal single-phase region. These fluids can have variations in the speed of sound opposite of that of an ideal gas and their speed of sound can thus vary nonmonotonically with velocity. This can result in peaks in the Mach number in an isentropically expanding flow. All other thermodynamic property evolutions in a flow are only quantitatively different from those of an ideal gas, just like for LMCs. Thus, these fluids are classified as classical[14].

In Figure 2.6, the normalised $P\nu$-diagrams of three different substances are compared, including the compressibility factor and the fundamental derivative isolines. Here, the diagram on the left shows an LMC fluid, the middle a BZT, and the right a mixture representing an HMC fluid. It can be seen that the fundamental derivative of gas dynamics of the LMC fluid is always above one, and the isolines are straight, meaning the speed of sound variation is like that of an ideal gas. The diagram also confirms that LMC fluids still show nonideal behaviour, since the compressibility factor can be lower than one. The other fluids show curving isolines, indicating a reversal of the speed of sound variation compared to that of an ideal gas. The BZT has a molecular complexity higher than that of the HMC fluid, resulting in a higher curvature of the isolines.

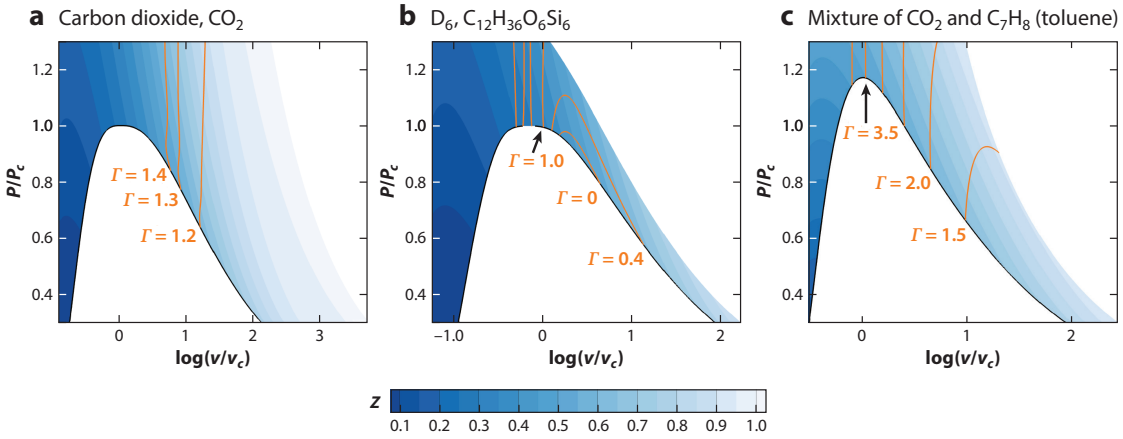

Figure 2.6: Example $P\nu$-diagrams with the compressibility factor and fundamental derivative of gas dynamics isolines with: (a) Low molecular complex fluid, (b) BZT fluid and (c) High molecular complex fluid[14]

2.3. NICFD Numerical Analysis

When designing the linear cascade test section, accurate numerical flow simulations are critical. Significant inaccuracies in the numerical simulations will result in incorrect flow conditions in the physical experiment. This section will discuss the methods that have been implemented to extend the capabilities of computational fluid dynamics (CFD) tools to accurately model nonideal compressible flows.

As discussed in section 2.2, the continuity equations are not sufficient to determine all unknowns when considering compressible fluids. Thus, the continuity equations are closed with an Equation of State, which relates the thermodynamic properties of the fluid. This is also called the first closure condition. Many EoSs for real fluids have been developed. According to Post [19], there are three types of EoSs: virial, analytical, and purely empirical.

Virial EoSs are based on polynomial series expansions of the compressibility factor (Equation 2.2), which for pure fluids are only a function of temperature and can be deduced from molecular theory[19]. According to Post, they can only accurately model modest deviations from ideal gas conditions.

The most common analytical EoSs are cubic equations of state (CEoS). These are based on the assumption that there should be an EoS that is valid for all fluids. The van der Waals equation (Equation 2.1) is one of the simplest CEoS. CEoSs are widely adopted because they need limited input information and can be extended to fluid mixtures, but are inherently inaccurate near the critical point[20]. The most common modern CEoSs are Peng-Robinson[1], improved Stryiek-Vera Peng-Robinson (iPRSV)[21] and Sovae-Redlich-Kwong[22]. CEoSs are usually expressed in terms of pres-

sure as a function of temperature and density, $P = P(T, \rho)$, according to Guardone et al. [14]. For these models, an additional expression for the ideal gas c_{p} or c_{v} is also needed[14].

Lastly, empirical EoSs are derived from measurements and are valid only for one substance within the measurement space. These models are referred to as multi-parameter equations of state (MEoS). Unlike CEoS, they are usually expressed in the reduced Helmholz energy $\alpha = \alpha(T, \rho)$[14, 19]. The Helmholz energy A is defined as the useful work that can be extracted from a closed system isothermally,

$$A \equiv U - Ts, \tag{2.6}$$

where U is the internal energy, T the temperature, and s the entropy. Then, the equation of state can be written as

$$\frac{a(T, \rho)}{\mathrm{R}T} = \frac{a^{\mathrm{o}}(T, \rho) + a^{\mathrm{r}}(T, \rho)}{\mathrm{R}T} = \alpha^{\mathrm{o}}(\tau, \delta) + \alpha^{\mathrm{r}}(\tau, \delta), \tag{2.7}$$

where a is the specific (or molar) Helmholtz energy, R is the gas constant, $\tau = \frac{T_{\mathrm{c}}}{T}$ is the inverse reduced temperature and $\delta = \frac{\rho}{\rho_{\mathrm{c}}}$ is the reduced density (with respect to their critical values)[23]. It can be seen that the reduced Helmholtz energy is divided into two components. The first component (α^{o}) represents the behaviour of an ideal gas, while the second component (α^{r}) represents the behaviour of the residual real gas. The Helmholtz free energy representation does not require an additional relationship, as opposed to the pressure representation, since all other thermodynamic properties can be derived from combinations of its partial derivatives according to both Post, Span and Wagner. An overview of these relations can be found in Table II of Span and Wagner [23, p. 11].

Colonna and Silva [20] state that MEoSs are very accurate in both the liquid and vapour phases, even close to the critical point. Their accuracy increases with increasing number of parameters. Post and Guardone et al. divide MEoSs into reference models and technical models. Reference models have an uncertainty of the same order as the high accuracy measurement data used to fit the model, while technical models have higher uncertainties than reference models but lower than simpler models(in the order of 0.1%) [24]. The most common MEoS is the Span-Wagner representation[23]. In this representation, the ideal gas part of the reduced Helmholtz energy is derived from an equation of heat capacity for the ideal gas, $c_{\mathrm{p}}^{\mathrm{o}}$. More distinctively, a formulation for the residual is found based on the interpolation of the measurement data.

A collection of MEoS can be found in the *REFPROP* library of the National Institute of Standards and Technology (*NIST*)[2]. Another library containing thermodynamic and transport property models is *FluidProp*[25]. FluidProp contains seven libraries, including *REFPROP*. It was originally developed by researchers at the Power and Propulsion group at Delft University of Technology. Furthermore, a common open source database is *CoolProp*[3].

The main drawback of MEoSs is that they are computationally demanding since they require expensive iterations. This is because the thermodynamic potentials depend on two variables instead of one, which must be determined by iteration to achieve thermal equilibrium[14]. This makes direct use of MEoSs unfeasible for technical use, since it can increase simulation times by two orders of magnitude[14]. A solution to this is the look-up table (LUT) method. Here, the MEoS is evaluated for a certain thermodynamic space and resolution. The results are then stored in a table that is interpolated to get the required values. This significantly reduces the computation time while retaining high accuracy if the proper interpolation method and resolution is used[19].

In addition to the thermodynamic properties, transport properties must also be modelled. This is done with a second class of closure conditions. The properties affecting NICFD flows are viscosity and thermal conductivity[14]. According to Guardone et al. the effect of pressure on viscosity and thermal conductivity becomes significant when $1 < T_{\mathrm{r}} < 1.5$ and $P_{\mathrm{r}} > 1$. Here, $T_{\mathrm{r}} = \frac{T}{T_{\mathrm{c}}}$ and $P_{\mathrm{r}} = \frac{P}{P_{\mathrm{c}}}$ are the reduced temperature and pressure. T_{c} and P_{c} are the critical temperature and pressure, respectively. That is, the critical point of a fluid is at $T_{\mathrm{r}} = P_{\mathrm{r}} = 1$. When the effect of pressure becomes significant, the ideal gas assumption fails, and again real gas relations are required. For MEoSs, corresponding

relations for the transport properties are used according to Post [19]. These can also be found in the *REFPROP* and FluidProp libraries.

There are many commercial and academic numerical solvers that have implemented methods for evaluating nonideal compressible flows. Since 2006, *ANSYS Fluent* and later *ANSYS CFX* have the possibility of simulating NICFD effects, offering the possibility of determining thermodynamic properties with cubic equations of state or external look-up tables for even more accurate models[4]. Open-source platforms like *OpenFoam* and *SU2* have been developed in academia and can also model NICFD effects.

2.4. NICFD Experiments

Head [4], Guardone et al. [14] and Wiesche [15] all credit Duff [26] for the first documented NICFD experiment. He conducted a CO_2 expansion experiment using a de Laval nozzle in a blow-down wind tunnel. Next, Dettleff et al. [27] used a shock tube to generate liquefaction shocks in organic fluids. These are compression shocks that cause condensation. The first experiments to show the existence of rarefaction shocks were performed by Kutateladze, Nakoryakov, and Borisov [28], but these results were disproven. Later, Bier et al. performed experiments using planar and axially symmetric Laval nozzles to investigate spontaneous condensation first in CO_2[29] and then in organic refrigerants. The first NICFD experiment in a continuous wind tunnel was performed by Anders, Anderson, and Murthy [30], who modified an existing wind tunnel to use SF_6 as a working fluid. Instead of investigating NICFD, the goal of this work was to increase the Reynolds number for transonic wind tunnel experiments. The next attempt to investigate rarefaction shock waves was made by Fergason and Argrow [31]. These experiments were also unsuccessful as a result of the thermal decomposition of the organic fluid. Years later, Colonna et al. [32] at Delft University of Technology designed and constructed a new shock tube facility called Flexible Asymmetric Shock Tube (*FAST*). It took another seven years until the first results of this facility were published by Mathijssen et al. [33]. The cause of this delay was due to the challenges in operating the facility's unique fast-opening valve at high temperatures[4]. According to Head [4], the *FAST* facility was moved to a new location. After a period of downtime, it is said that experiments with the *FAST* facility have resumed. However, the list of research facilities at Delft University of Technology no longer list the *FAST* facility[34]. It turns out that the *FAST* facility has been replaced by a new facility, the Asymmetric Shock Tube for Experiments on Rarefaction waves (*ASTER*). This shock tube facility was designed to be "smaller, simpler, and easier to operate"[35] than its predecessor. The most recent developments were published by Chandrasekaran [35]. For more details on the experimental history, Head [4, p. 19-41] provides an in-depth historical overview of NICFD experiments.

From the historical overview of NICFD experiments it can be concluded that blow-down facilities, including shock tubes, were almost always used. The reason for this is that these facilities are one of the simplest and cheapest that can produce supersonic flow[15]. Shock tubes work by separating high-pressure and low-pressure gases by a diaphragm. This diaphragm can then be burst mechanically or be designed to burst at a certain condition. When it bursts, a shock wave propagates through the low-pressure section of the tube.

Closely related to shock tubes are Ludwieg tubes. These also use a diaphragm. However, instead of a low-pressure gas section, the high-pressure gas is separated from a vacuum tank or 'dump tank'. The high-pressure tube section includes a convergent-divergent nozzle. When the diaphragm breaks, a shock wave propagates into the vacuum tank, while an expansion wave propagates into the high-pressure section. The unsteady expansion sets up a steady subsonic flow towards the nozzle. The nozzle then accelerates this flow to supersonic conditions[15].

A major drawback of shock and Ludwieg tubes is the very short measurement time, which is of the order of milliseconds (see Table 2.2). Blow-down wind tunnels can offer an improvement in this area. The term "wind tunnel" in this case is not quite accurate, since these tunnels operate with organic vapours instead of air as the working fluid. As suggested by Wiesche [15], the term "vapour tunnel" would be more fitting. However, he also states that wind tunnel is the accepted terminology in aerodynamics. A (thermally driven) blow-down wind tunnel also uses a high-pressure and low-pressure tank, however, they are now separated by a valve. The high pressure fluid is heated to high temperature, vaporising it. Then, the valve is opened and the flow expands through the test section, after which it is collected

in the low-pressure tank. This method can reach measurement durations of the order of one hundred seconds.

To achieve even longer testing times, continuous working facilities are used. These techniques have drawbacks compared to the blow-down facilities. First, these systems require substantial power to achieve high-speed flow conditions as a result of the high density of organic fluids. Furthermore, the whole system must be able to handle high-pressure and high-temperature conditions. Lastly, all joints must be carefully sealed to avoid leaks, as organic fluids can be toxic or have high greenhouse gas or ozone depletion potential[15].

There are two types of continuous working facilities that are used for NICFD experiments. First, there are compressor-driven wind tunnels. As the name suggests, they use a compressor to drive the organic fluid. This is the simplest continuous working wind tunnel type, but requires a large amount of energy to operate. The second type are organic Rankine cycle wind tunnels. Here, the flow passes through an evaporator, the test section (expansion component), a condenser, and finally a pump. The drawback of this system is the higher complexity compared to the compressor-driven wind tunnel. However, the advantages of lower power requirements are two-fold. Firstly, the Rankine cycle allows for higher Mach number values. Secondly, by replacing the test section with a turbine, the facility can be converted to a power system test rig. A heat exchanger can be implemented in both continuous working concepts, reducing the thermal power required. However, this power requirement remains substantial[15]. An overview of NICFD test facility classifications can be found in Figure 2.7.

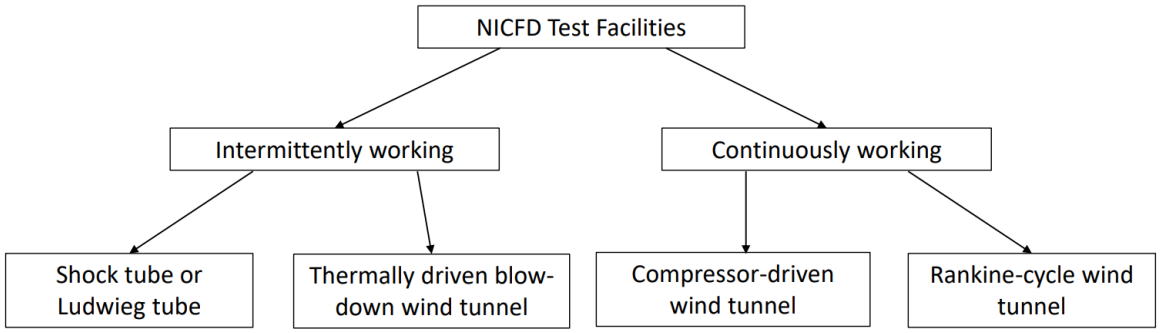

Figure 2.7: Classification overview of NICFD test facilities[15]

Currently, there are a limited number of NICFD test facilities in operation. A detailed overview of current facilities, their type of operation, and specifications, published by Wiesche [15], can be seen in Table 2.2. In addition to this, an overview of the different experiments performed in each facility can be found in Table 2.3. Head [4] also describes all except the Cambridge facility, while Guardone et al. [14] only includes the *TROVA*, *CLOWT* and *ORCHID*. As discussed previously, the facility missing from all these sources is the *ASTER* facility at Delft University of Technology. This is a Ludwieg tunnel that can operate at 25 bar, 400 °C and uses a glass diaphragm to facilitate sudden expansion[34]. Its charge tube has an outer diameter of 17.5 mm and a thickness of 2.35 mm [35]. The first experiments used siloxane D_6, with compressibility factors of $0.44 < Z < 0.95$ [35].

The other Ludwieg tube facility that is known to be in operation is the Cambridge Real Gas Wind Tunnel. The first experiments in the facility were performed by Durá Galiana et al. [36, 37] and used a flat plate to investigate trailing edge losses. In these experiments, a flat plate embedded in an axisymmetrical nozzle was used. The experiments were carried out with air, CO_2 and SF_6 as working fluids. The experiments were carried out at ambient temperature and different nozzles were used for each working fluid to ensure that the tests were carried out at the same Mach number ($M \approx 2$). Pressure transducers were used to measure the wall static pressure, inlet total pressure, and base pressure. A thermocouple was used to determine temperature, but because of short measurement times, the temperature could only be measured with pre-run measurements. Measurement data was then compared to extensive CFD analyses using Reynolds-averaged Navier-Stokes (RANS), detached-Eddy simulation (DES) and large-Eddy simulation (LES) methods.

The next experimental campaign was performed by Baumgärtner, Otter, and Wheeler [38]. Here, the flat plate and nozzle were replaced by an annular supersonic turbine vane cascade with eight passages. The vanes consisted of circular leading and trailing edges and a converging-diverging nozzle section. The vane span was 5 mm for a total diameter of 40 mm. The outer casing contained pressure transducers along the mid-pitch streamline to measure wall static pressure. The casing was able to rotate to move the pressure taps relative to the vanes. Experiments were carried out with argon, CO_2, air, and R134a. The experimental results were compared with a RANS simulation.

Table 2.2: Currently available NICFD test facilities[15, p. 13], obtained from White [39]

Test Facility	Institution	Type and Operation mode	Measurement Times	Working Fluids	Pressure	Temperature	Mach Number	Minimum Z/Γ	Test Section
TROVA	Milano, IT	Blow-down wind tunnel	10 up to 100 s	Siloxanes, refrigerants, hydrocarbons	Up to 50 bar	Up to 400 °C	Up to $M = 3$	$Z = 0.3/$ $\Gamma < 1$	50 mm x 100mm
ORCHID	Tu Delft, NL	Rankine wind tunnel (continuous)	Long time	Siloxanes, refrigerants, hydrocarbons	Up to 25 bar	Up to 380 °C	Up to $M = 3$	$Z = 0.3/$ $\Gamma < 1$	Limited by thermal power (400 kW)
CLOWT	FH Munster, DE	Closed wind tunnel (continuous)	Long time	Novec 649, air	Up to 10 bar	Up to 150 °C	Up to $M = 1.3$	$Z = 0.7/$ $\Gamma = 0.8$	50 mm x 100 mm or 42 diameter (jet)
Cambridge Real-Gas Wind Tunnel	Whittle, UK	Ludwieg tube	10-100 ms	R134a, SF6, CO2, Air, N2, Argon	Up to 45 bar	15-150 °C	Up to $M = 2.5$	$Z = 0.6/$ $\Gamma < 0.9$	50 mm tube diameter
ICL-TRANSIENT	Imperial, UK	Blow-down wind tunnel	Short time	Refrigerants	Up to 30 bar	70 °C (nominal)	Up to $M = 2.2$	$Z = 0.5/$ $\Gamma = 1.05$	2 mm throat height

The Imperial College London (*ICL*) *TRANSIENT* facility is a blow-down wind tunnel. Robertson et al. [40] performed experiments with this facility to validate CFD simulations of highly nonideal flows. A planar nozzle test section with a height of just 2 mm was used, designed for an exit Mach number of 2. The working fluid for this experiment was R1233zd(E). Eight pressure taps across the centre line of the nozzle were used to measure wall static pressure. Since the pressure transducers were rated for a maximum temperature of 75 °C, and the operating design temperature was 200 °C, direct measurement from the test section was not possible. This was solved by using connecting tubes that were long enough to ensure that the temperature at the pressure transducers was sufficiently reduced by convection. This raised concerns about the dynamic response that the sensors would be able to achieve. Thus, the first and last transducers were replaced with sensors that could operate at high temperatures and thus be attached directly. RANS simulations were also performed comparing different EoS models: Helmholtz free energy, Peng-Robinson and ideal gas.

The other blow-down wind tunnel is the Test Rig for Organic Vapours (*TROVA*) of the Politecnico di Milano. It can achieve the highest operating pressure and temperature of the known NICFD test facilities and can operate with a variety of working fluids. The first experiments were performed on a planar converging-diverging nozzle with static pressure taps along the nozzle axis and one-sided optical access for schlieren imaging. The working fluid used was siloxane MDM. Initial experiments[41, 42] focused on qualitative investigation of the flow structure as well as quantitative analysis of the pressure measurements. Later, the development of the Mach number in the flow was investigated on the basis of the shock wave angles, using automated image processing on the Schlieren images[43, 44, 45]. Later, Zocca et al. [46] investigated a diamond-shaped aerofoil placed in a planar nozzle exit and compared the results to inviscid shock theory complemented with an EoS to account for nonideal effects. After this, a linear stator cascade consisting of three blades was tested. Measurements were performed with static pressure taps and a traversable total pressure probe in the wake. The blades were placed at a high stagger angle, which was found to generate representative wake flows for both axial and radial stator geometries while allowing a straight test section. The side walls were designed using the streamlines from numerical modelling to improve the flow periodicity.

The Closed Loop Organic vapour Wind Tunnel (*CLOWT*) is one of the two continuous working facilities. It is a compressor-driven wind tunnel. Experiments were performed using a calibration section

to also investigate measurement techniques such as the experiments at the *TROVA* facility, although the experiments at *CLOWT* were performed at high subsonic speeds compared to supersonic speeds at *TROVA*. Also similar to the *TROVA* experiments, a three-blade linear cascade was tested (again at high subsonic exit flow conditions). A traversing mechanism for both total pressure and hot-wire anemometry sensors was used in front and behind the cascade to measure flow fields. With the data, boundary layer and trailing edge losses were evaluated. Furthermore, the effect of surface roughness was investigated, since the cascade was made via selective laser melting.

Table 2.3: Experiments performed in currently available NICFD facilities

Test Facility	Experiment	Working Fluid	Publications
TROVA	Planar nozzle	Air, Siloxane MDM	[41], [42], [43], [44], [45], [47]
	Planar nozzle with Pitot tube	Siloxane MM	[48]
	Linear cascade	Nitrogen, Siloxane MDM, Siloxane MM	[49], [50], [51]
	Diamond shaped airfoil	Siloxane MDM	[46]
	Laser Doppler Velocimetry of planar nozzle	Siloxane MM	[52]
ORCHID	Planar nozzle	Siloxane MM	[53], [4], [54]
	Particle Image Velocimetry of planar nozzle	Siloxane MM	[55]
CLOWT	Rotatable cylinder Pitot probe	Air, Novec 649	[56], [57], [58]
	Hot-Wire Anemometry with turbulence sphere	Novec 649	[59]
	Additively manufactured linear cascade	Air, Novec 649	[60], [61]
Cambridge Real-Gas Wind Tunnel	Flat plate trailing edge loss	Air, CO_2, SF_6	[36], [37]
	Annular cascade	Argon, air, CO_2 R134a	[62], [38]
ICL-TRANSIENT	Planar nozzle	R1233zd(E)	[40]

Finally, there is the Organic Rankine Cycle Hybrid Integrated Device (*ORCHID*), which is a Rankine cycle vapour tunnel at Delft University of Technology. Head [4] provides a detailed overview of the preliminary design, design and commissioning, and design of the first test section of the facility. The facility consists of an evaporator (primary heat exchanger), a regenerator, a condenser, and a pump. The fluid can be sent to one of two test sections. One is a planar nozzle test section with optical access to perform fundamental NICFD experiments. The second can house a mini-ORC expander test section. This setup is what makes this a hybrid device. The *ORCHID* facility, as well as a simplified process flow diagram, can be seen in Figure 2.8. The flow is vaporised by the primary heat exchanger and sent through one of the test sections. A regenerator transfers some of the residual heat from the flow to the flow after the pump, reducing the energy needed by the primary heat exchanger. The flow is then condensed by the condenser. The pump then increases the pressure of the flow again to complete the loop. The system is designed for a maximum pressure of 25 bar and a temperature of 400 °C (which is the maximum temperature of the thermal oil). The thermal energy source of the primary heat exchanger is an electric heater with a rated thermal power of 400 $\mathrm{kW_{th}}$. The mass flow rate is limited to 1.4 kg/s due to vibration problems of the main pump at higher mass flow rates[4].

Head [4] describes the design and commissioning of the nozzle test section and Beltrame et al. [53] discuss the first experimental results. Similarly to the experiments at the *TROVA* facility, the evolution of the Mach number throughout the flow was determined using automated image processing with schlieren images. Unlike those experiments, static pressure taps are placed on the top and bottom nozzle profile walls instead of the back wall. This allowed for two-sided optical access. The data collected was compared with a numerical simulation to verify the open-source CFD programme *SU2*. Later, Michelis et al. [55] were the first to publish the use of particle image velocimetry in supersonic vapour flows to quantitatively assess the velocity field. This measurement technique will also be discussed in more detail in section 2.5.

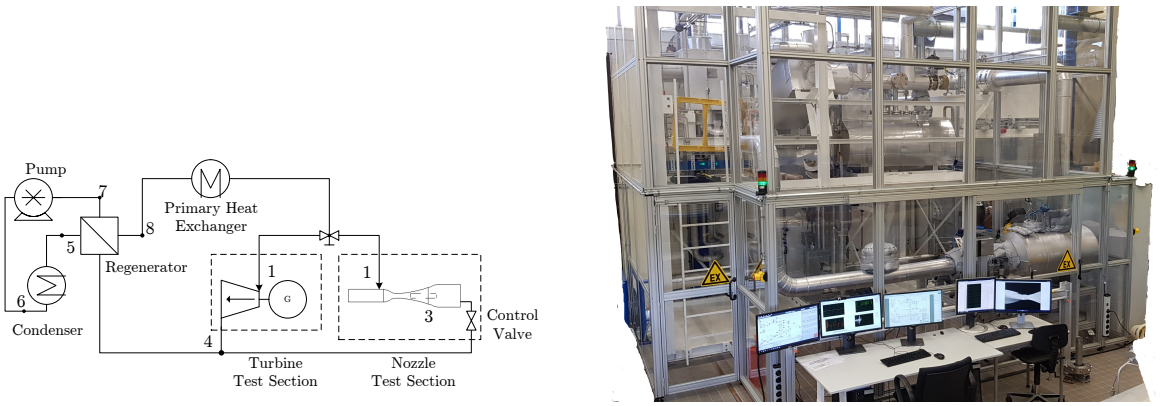

(a) Simplified process flow diagram of the *ORCHID*

(b) Picture of the *ORCHID*

Figure 2.8: *ORCHID* facility[4]

2.5. NICFD Measurement Techniques

There is a large array of techniques that can be used to measure flow properties. However, the high temperature and density of NICFD flows introduce challenges, especially in supersonic flows. Guardone et al. [14] discuss many of these issues. Furthermore, an extensive review of NICFD measurement techniques is provided by Wiesche [15]. This section will discuss these issues, their solutions, and the adoption of these techniques in recent experiments.

2.5.1. Static Pressure Measurements

First, for static pressure measurements, pressure taps are used. These are small holes drilled along a wall, normal to the flow velocity. These holes are connected to pressure transducers. There are several complications when working with high-temperature organic vapours. First, the materials used for the sensors must be chemically compatible with the working fluid. Furthermore, they must be rated for the high temperatures expected in the flow. Even if this is the case, pressure sensors are sensitive to temperature, so they must be calibrated at the expected operating temperature. Another option is to connect the pressure transducers with tubing, instead of directly to the test section. In this way, the sensors can be thermally decoupled from the test section, because convection reduces the temperature of the tube before the pressure transducer. An example of this is shown in Figure 2.9. However, this introduces new problems. Due to the increased volume between the pressure transducer and the flow, the dynamic response of the transducers is reduced. Fast dynamic response is important when high-frequency pressure transducers are used, for example, to determine turbulence intensity. Carmine et al. [41] used a method by Antonini, Persico, and Rowe [63] to estimate the resonance frequency and thus determine a maximum observable frequency. On the other hand, Robertson et al. [40] instead replaced two pressure transducers with directly attached high-temperature transducers to check the dynamic response of the thermally decoupled probes.

Another issue that occurs is condensation of the organic vapour in the tubing or pressure transducers. This condensation can cause incompressible plugs that separate the transducer from the test section[15], rendering it essentially useless. This issue is most relevant for continuously working vapour tunnels and blow-down tunnels. Shock tube experiments can use directly attached pressure transducers, because of the very short measurement times[15]. Wiesche [15] lists three possible solutions to the condensation issue, of which only two are practical and used in organic vapour flows.

Firstly, liquid traps and purging devices can be added to the lines connecting the pressure transducers to the test location. These ensure that the lines are clear of condensation. Purging systems are employed by the *TROVA*, *CLOWT* and *ORCHID* facilities. Conti et al. [48] describe the method used at the *TROVA* blow-down wind tunnel facility. The lines of the measurement system are connected to a nitrogen tank. Using a pressure regulator, the nitrogen pressure is set to be just higher than the maximum expected pressure of the test section. Using a timer, the nitrogen tank is opened as the test starts and closed just

after the peak pressure. In this way, only nitrogen is ever present in the lines, avoiding condensation.

The second solution discussed by Wiesche is to place the pneumatic lines within the hot environment of the test facility so no condensation occurs within the lines. Closed-loop facilities like *CLOWT* must employ this method, since nitrogen contamination caused by the purge method cannot be removed from the working fluid. To overcome this, Reinker et al. [57] use a passive pressure transducer thermal decoupling system, incorporating a U-tube. This tube causes condensate to pool in the bottom of the U-tube. This will introduce a systematic error in the pressure measurement, depending on the height of the fluid buildup. The maximum error is thus dictated by the height of the U-tube. The thermally isolated pressure transducer can be connected to one of twenty pressure taps with a set of valves operated by a rotating shifter. This assembly is placed inside the heated area of the wind tunnel to ensure that no condensation occurs. An overview of the valve assembly and a thermal image of the U-tube can be seen in Figure 2.9.

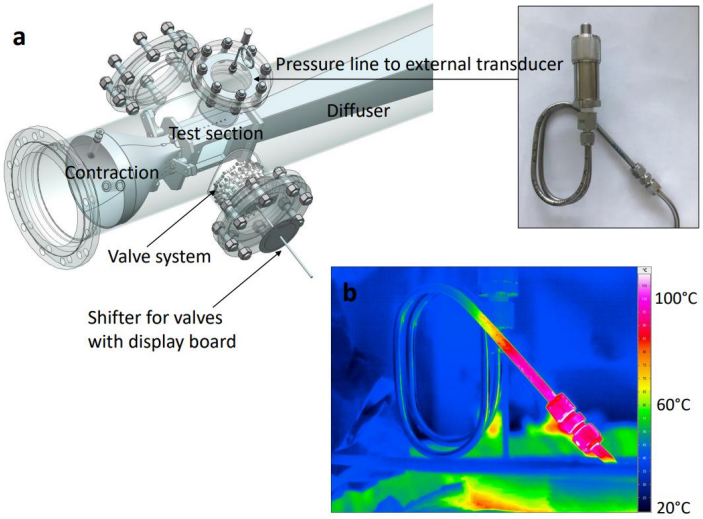

Figure 2.9: Pressure measurement system of the *CLOWT* facility: (a) valves and lines in hot area of the wind tunnel and (b) thermal image of the thermally decoupled pressure transducer by U-tube[15]

Because the *ORCHID* system uses an evaporator and condenser, nitrogen can be separated from the condensate since nitrogen is not condensible[15]. For this reason, a nitrogen purging system is used. Head [4] describes the system in detail. The static pressure taps are connected to a pressure scanner (Scanivalve) via liquid traps. The assembly of the liquid traps can be seen in Figure 2.10. Each trap has optical access, so the operator can see if condensation occurs. If this is the case, the lines can be purged with a burst of nitrogen. Furthermore, each trap has two valves. One to isolate the trap from the pressure scanner and one to drain any condensate that formed in the liquid trap.

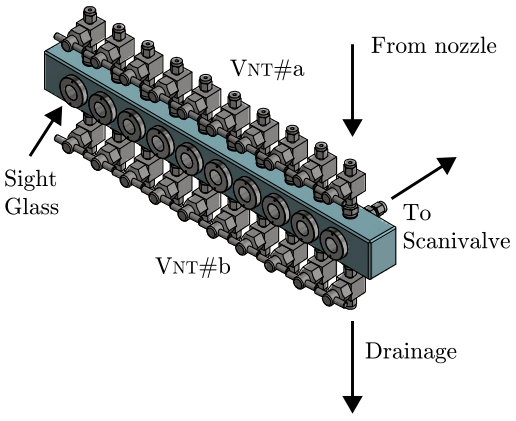

Figure 2.10: Assembly of the liquid traps used at the *ORCHID* facility[4]

2.5.2. Stagnation pressure measurements

To determine the stagnation pressure, stagnation pressure probes are used. These are tubes with a hole in the tip that is placed directly in the flow path. This causes the flow to stagnate in the tube, converting its kinetic energy into pressure, thus the total pressure can be measured by a pressure transducer. Furthermore, total-static Pitot tubes include static pressure taps orthogonal to the flow direction. With these instruments, both total and static pressures are measured, thus flow velocity can be directly determined.

For these devices, the same difficulties with operating temperature and condensation apply as for static pressure taps. Further challenges arise in trans- and supersonic flows because of compressibility effects ahead of the probe. For subsonic flows, the stagnation pressure can be measured directly, but in nonideal compressible flows a data reduction is required. Using a proper equation of state together with conservation equations, the flow quantities can be derived from total flow conditions and measured stagnation pressure[15]. In supersonic flows, a bow shock occurs ahead of the probe, causing a loss of total pressure. To quantify the total pressure before the shock, an additional static pressure measurement is needed ahead of the shock, since the pressure loss is affected by Γ and Z[14].

Another problem to overcome is that because of the increased fluid density, the probe is subject to high loads and vibrations, complicating the probe design. The material and shape of the probe must be chosen properly to avoid vibrations that can distort the measurement data. Furthermore, flow blockage effects and probe interaction are highly relevant for turbomachinery experiments due to the large relative size of the probes compared to the cascade geometries[62]. An example of probe interaction can be seen in Figure 2.11. Supersonic flows especially suffer from these effects due to the generation of shock waves.

The first use of stagnation probes in NICFD experiments was reported by Dura Galiana et al. [37, 36] to determine wake losses of a flat plate for supersonic flows of organic vapour. They used sintering 3D-printing techniques to produce the probes. This allowed them to easily change the design to find the design with minimal blockage effects. The final design used a wedge probe with an angle of 10 degrees. The sensors were placed directly inside the probes to minimise dynamic response times. Baumgärtner et al. [38, 64] also investigated the blockage effect of different probe designs. They also found a wedge probe design to significantly reduce blockage effects compared to a circular design. This can be seen in the CFD models in Figure 2.11. The comparison shows a significant reduction in probe interaction for the wedge probe. An additional advantage of the wedge shape was a higher structural integrity compared to a circular shape[64] .Baumgärtner et al. make use of the rotatable outer housing of the test section to take static pressure measurements throughout the passage.

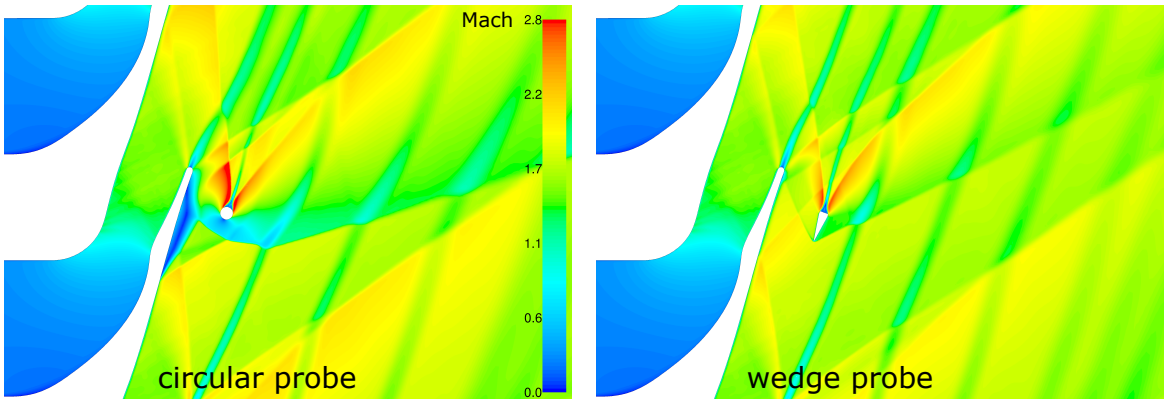

Figure 2.11: CFD simulation of a circular and wedge static pressure probe behind a stator vane cascade[64]

Conti et al. [48, 65] use a total-static Pitot tube in a planar nozzle with subsonic flows of siloxane MM. They determined that the level of flow ideality had limited effects on the stagnation pressure measurements, so no data correction was performed. Later, using the same facility, Manfredi et al. [50] replaced

the subsonic planar nozzle section with a supersonic linear stator cascade. The stagnation pressure probe is placed on a traversing system. This allows the probe to be placed at the blade mid-span exactly above one of 21 static pressure taps in the rear wall. This is necessary since the static pressure is required to correct for the pressure loss caused by the induced bow shock ahead of the total pressure probe. In addition to static pressure, the total pressure and temperature of the inlet flow are used together with the total pressure after the shock (measured by the probe) to determine the total pressure ahead of the shock. This is possible since the flow is assumed to be adiabatic due to the addition of a heating system and insulation of the test section.

Reinker et al. [57] tested a rotatable cylindrical pitot tube in high subsonic organic vapour flow. They used a data reduction process to determine Mach number and velocity of the nonideal flow. They found significant deviation from perfect gas flows at high subsonic flows. Later Hake et al. [61, 60] also used traversing stagnation pressure probes in experiments on a linear cascade in subsonic organic vapour flows. They used two traversing Pitot tubes to measure the stagnation pressure profiles along the blade passage. Data reduction was performed based on data in the *REFPROP* fluid database to account for nonideality.

The flow direction can also be determined with multihole pressure probes. However, there is no literature documenting the successful implementation of this technique for organic vapour flows[14].

2.5.3. Hot-Wire Anemometry

Another intrusive measurement technique is Hot-Wire Anemometry (HWA). This technique uses a thin wire through which an electric current passes. The flow velocity can be measured from this current by equating the heat introduced to the wire from the electrical resistivity of the wire to the heat lost through forced convection to the flow. Because of the small size of the wire, high frequency velocity fluctuations can be detected. For this reason, HWA is often used in turbulence research[15].

Like for static pressure probes, the high density flows of organic vapour cause high mechanical loads on the HWA probe. This can also lead to vibration problems, as discussed for the stagnation pressure probes. Furthermore, these high loads limit the miniaturisation of the wires, as they can break if they get too thin. This limits the turbulence resolution of the measurements[14].

Reinker and Aus Der Wiesche [59] first used HWA in low-speed to high-subsonic (up to Mach 0.7) organic vapour flows to assess its performance. First, the probe was placed in a planar converging diverging nozzle test section for calibration. Then, a sphere was introduced into the flow to create turbulence. Turbulence intensities, length scales, and velocity spectra were successfully determined. However, high Reynolds number and high dynamic loads were encountered. Later, more experiments with the same setup were performed by Hake et al. [61].

Then, Hake, Sundermeier, and Wiesche [60] used HWA to investigate the flow fields up- and downstream of a linear cascade. The traversing Pitot tubes discussed previously were replaced by HWA probes, allowing them to use the same traversing mechanism. Significant vibration issues were encountered at Mach numbers greater than 0.6, which were detected with a high-speed camera. Furthermore, calibration required substantial effort.

Finally, Hake et al. [66] conducted a measurement campaign to investigate grid-generated turbulence. Again, flow conditions were low to high subsonic. A turbulence generating grid was placed in front of the calibration test section used in the previous experiments. The results of the measurements were used to validate the numerical methods.

Currently, no attempts have been made to apply HWA to supersonic organic vapour flows because of the issues discussed.

2.5.4. Schlieren Imaging

With schlieren imaging, density gradients, and thus refraction index variations are visualised[15]. Schlieren imaging is the oldest noninvasive optical flow measurement technique used in wind tunnel experiments. It has long been a comparatively easy way to provide qualitative measurements of shock waves to add to qualitative measurements. However, recent developments allow for the derivation of qualitative measurements from Schlieren images. The use of modern computer vision techniques allows for automatic

measurement of the location and angle of shock structures, with which local Mach number values can be determined[4, 67]. Furthermore, advances in background-orientated schlieren (BOS) imaging allow measurements of the density field[58, 67]. Schlieren imaging can be used for NICFD experiments because organic vapours are transparent. Moreover, Head showed that higher-contrast images can be obtained with the same equipment for organic vapours than for air, because of a higher refractive index for the same comparative density increase. He states that: ”the variation of light intensity through a dense organic vapour is much larger than that through air for comparable density changes; thus much less optical sensitivity is needed in order to obtain Schlieren images of dense organic vapour flows compared to that needed for air flows. Conversely, for a given quality of the optical equipment, a much higher contrast of the schlieren image can be obtained if the fluid of the observed flow is a dense organic vapor.”[4, p. 163]

The refraction index n is defined as the ratio of the speed of light in a vacuum to the speed of light in a medium: $n \equiv \frac{c_0}{c}$[4]. The relation between the refraction index gradient ∇n and the density gradient $\nabla \rho$ can be derived from the Gladstone-Dale equation as $\nabla n = \mathrm{K} \nabla \rho$, where K is the Gladstone-Dale constant[67]. From this equation, it becomes clear that a density gradient in one direction results in a refraction index gradient in the same direction. So, light rays are bent towards higher-density regions. Schlieren images are generated by using a knife edge to convert these light deflections into changes in light intensity.

A schematic showing the working principle of Schlieren imaging can be seen in Figure 2.12. In this case, a density gradient in the x-direction causes light to deflect with angle ϵ. The size of this angle is proportional to the refraction index gradient and thus to the density gradient. It can be seen that, because of the deflection angle, the light ray gets blocked by the knife, thus causing a reduced light intensity. In this way, the location of a density gradient (and thus a shock wave) is visualised as a dark region. By rotating the knife edge 90 degrees, density gradients in the y-direction can be visualised instead of the x-direction. In the case displayed in Figure 2.12, assuming that the flow direction is in the x direction, the location of the knife causes compression shocks to appear dark because of their positive density gradient in the x direction. Expansion fans will have a negative gradient and thus appear brighter in the Schlieren image compared to the background. By placing the knife on the other side of the light, this visualisation can be inverted.

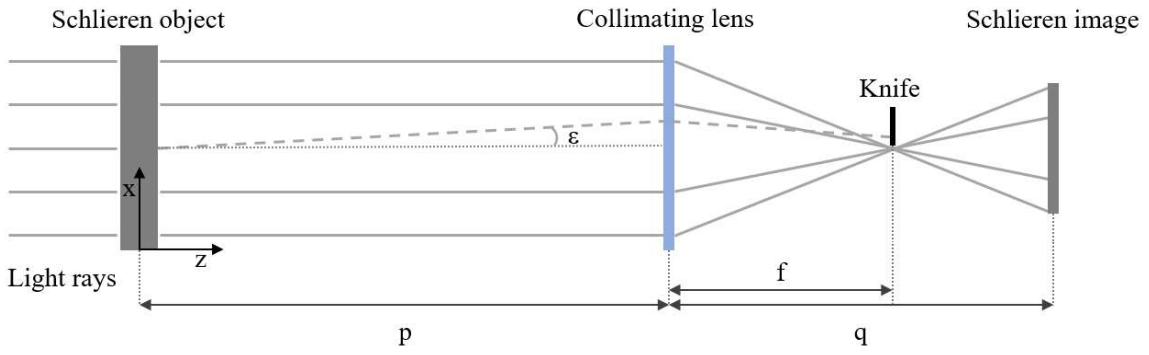

Figure 2.12: Illustrative sketch of the schlieren technique[67]

There are four types of Schlieren imaging setups. A schematic overview of these is provided by Wiesche [15] in Figure 2.13.

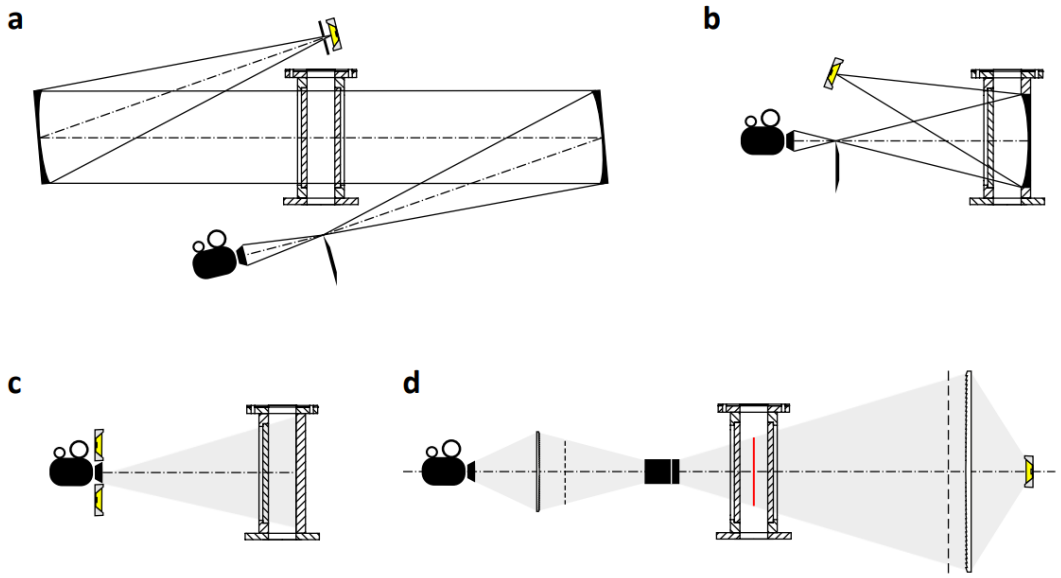

Figure 2.13: Four types of schlieren system: (a) conventional z-type, (b) double-passage, (c) background oriented and (d) focusing[15]

Head et al. [4, 53, 54] have used a conventional z-type setup at the *ORCHID* facility in multiple experiments of a planar nozzle. Light is passed through the test section, which is made possible by using two windows. A z-type setup was chosen because it was found to be less complex and costly compared to the other methods, while providing a high enough resolution[4]. An automated image processing tool was used to measure the angles of the shock waves in the supersonic part of the nozzle, which originate from imperfections in the nozzle walls. From these angles, the local Mach number could be determined across the nozzle centre line and at the exit plane.

Before these experiments, Spinelli et al. [42] were the first to use schlieren imaging on nonideal compressible flow through a planar nozzle at the *TROVA* facility. They employed a double-pass system. Instead of the concave mirror+ back wall seen in Figure 2.13, a mirror-polished back wall is used together with a prism to separate the emitting and receiving light beams. This has multiple advantages. First, this allows instrumentation like static pressure taps to be attached to the back wall. Furthermore, aligning the test section and the optical bench is much simpler.

However, there are some drawbacks as well. First, because the back wall was not heated, condensation occurred on its surface[42]. This condensation obscured the Schlieren images. However, as the back wall heated up from the fluid during the test, the condensation would disappear. Another expected issue is the fact that a polished steel surface will become dirty more easily[15]. However, this can be mitigated by cleaning the surface after a few experiments.

Later experiments[68, 43, 69, 67] using the same planar nozzle and schlieren setup improved the quality of the schlieren images. They discovered that the refraction gradients of the expansion fans in the flow were so large that the deflected light moved outside the measurement range. This caused the expansion fans to appear dark, while they should have appeared light. It was determined that this issue decreased with increasing nonideality. Spinelli et al. [44, 45] also report a Mach number estimation process based on schlieren images using computer-automated image processing, like the method used by Head [4]. Later, Zocca et al. [46] used the same setup to visualise the shock waves introduced by a diamond-shaped aerofoil placed in the nozzle test section. Finally, Manfredi et al. [50] mention the use of the Schlieren setup in their tests on a linear stator vane cascade. However, no results of these measurements were provided as the experiments were still ongoing.

The last known schlieren setup used for NICFD experiments is employed at the *CLOWT* facility and is a background-orientated Schlieren system. The system was developed by Sundermeier et al. [58]. It also relies on light reflecting off the back wall. However, this technique uses an anodised black aluminium

back wall with a laser engraved pattern of random dots. The distortions of the reflected light due to density gradients are then analysed using an image correlation algorithm. This allows for the quantitive measurement of the density field. However, the drawback is the reduced sensitivity compared to other techniques. This means that only high density gradients can be detected, limiting the technique to high Mach number flows.

2.5.5. LDV and PIV

Laser Doppler Velocimetry (LDV) and Particle Image Velocimetry (PIV) are more complicated optical techniques that are used to directly quantify velocity in the flow. Both methods rely on seeding particles. These are small particles added to the working fluid to reflect light. These particles must have about the same density as the working fluid, to minimise buoyancy, which is very difficult for organic vapour flows[15]. Furthermore, one would like to have small particles to minimise the effect on the flow. The maximum size of the particles is driven by their dynamic response time in the flow, which should not be higher than the characteristic time scale of the flow in case of unsteady flows[15] On the other hand, sufficiently sized particles are required to ensure a sufficient signal-to-noise ratio[15]. The latter can also be improved by choosing particles with a higher refractive index. Finally, the particles should be stable at high temperatures for organic vapours.

As the name suggests, LDV uses laser light. This light is scattered by the seeding particles. The velocity of the particles at a specific point of the flow can be determined from the Doppler shift of the scattered light. The first use of LDV for NICFD experiments is reported by Gallarini et al. [52]. They employed LDV to achieve the first complete characterisation of a point in a nonideal compressible flow of MM siloxane. To achieve this, they had to design a novel seeding system to evenly distribute the seeding particles in the flow.

PIV works on the basis of very different principles. Instead of relying on the Doppler shift effect, it determines particle velocity based on the location of the particles in a sequence of pictures. The velocity is then determined by a correlation technique[15]. The advantage of PIV is that it can be used to determine the two- or even three-dimensional velocity field, compared to a small measurement point. This comes with the drawback of having strict requirements on exposure time and illumination for high-speed flows[15].

The first application of PIV in an organic vapour was reported by Head [4]. A specially built non-intrusive vapour analyser was used to test the application of PIV on organic vapour flows. Three flow cases were analysed: natural convection, rotating disc, and combined natural convection and rotating disc flow fields. D_4 was used as the working fluid, with TiO_2 seeding particles. The experiments were performed to investigate the particle seeding density and the signal-to-noise ratio of the measurements. The results showed average flow field uncertainties below 1%, which was deemed acceptable for an accurate flow field assessment.

Next, Michelis et al. [55] reported the first use of PIV in supersonic organic vapour flows. These experiments were performed at the *ORCHID* facility using a planar nozzle test section. In the experiments, a sheet of laser light was introduced into the exit of the nozzle via an optical access window in the expansion vessel behind the nozzle test section. The refracted light from the particles could then be detected by a camera through the transparent side wall. A schematic of the setup can be seen in Figure 2.14. The camera was calibrated to detect the particles in the mid-plane of the test section. The measured velocities in the x and y directions were compared to RANS simulations, which were previously assessed by comparison with Mach number estimates from schlieren images (discussed in subsection 2.5.4). The results show an expanded uncertainty of 1.1% in the measured velocity field and a deviation from the RANS simulation from 0.1% in the throat to 10% in the outlet. This was determined to be a result of hardware limitations. These limitations will be addressed in further research, along with an investigation of flow fields with more pronounced nonideal effects.

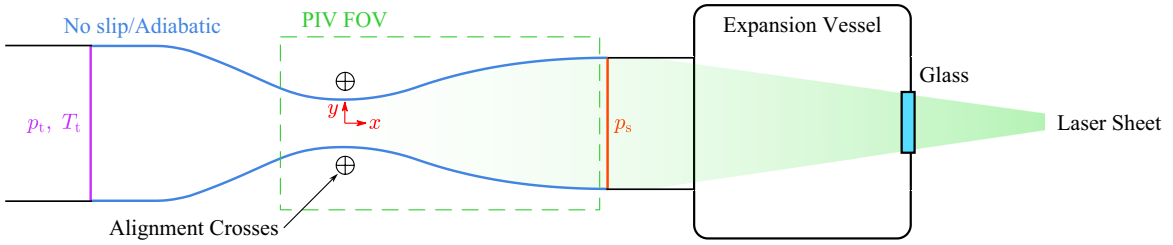

Figure 2.14: Schematic of the nozzle PIV setup at the *ORCHID* test facility[55]

2.5.6. Temperature and Heat Flux Measurements

To date, NICFD experiments mainly include temperature probes in the inflow and outflow of the test section to verify the test section operating conditions. Using these probes inside the test section will significantly disturb the flow in a way similar to the Pitot probes (and other intrusive measurement probes). However, different measurement techniques exist, which are widely adopted in high-temperature turbine experiments.

As stated in chapter 1, one of the experimental goals is to investigate flow characteristics such as the evolution of the boundary layer and the transition from laminar to turbulent boundary layer. Although not yet employed in NICFD experiments, conventional turbine experiments often use techniques based on heat transfer measurements to investigate boundary layers. One of these methods is heated thin-film measurement. This technique uses thin heated films placed on the blade surface to locally measure the mean and fluctuating heat transfer rate, from which the boundary layer condition can be determined[70]. Note that this technique is quite complicated to build into a blade. In addition, the films will inevitably disturb the flow. The possible erosion of the films as a result of the working fluid must also be investigated.

To overcome these issues, another commonly used method in conventional turbine experiments is infrared thermal imaging. This technique captures infrared radiation emitted by a surface. Then, the temperature of the surface is determined on the basis of the wavelength. The location of the laminar to turbulent transition can be detected on the basis of the surface temperature since the thermal conductivity of a turbulent boundary layer is higher than that of a laminar one, however, due to conduction the temperature will homogenise over time[71]. For this reason, metallic blades must be coated with an insulating material to increase measurement time. An additional challenge for infrared thermal imaging is that it requires a calibration procedure. Measurements can be disturbed by different factors: adsorption in the optical path (due to the working fluid and the transparent window), emission from the optical path, emission of the surroundings reflecting off the measured surface, and the emissivity of the target surface based on the viewing angle[72]. Reflection of the surrounding radiation can be minimised by ensuring that the target surface has a high emissivity. This can be done by applying a black surface coating. The other disturbances can be addressed with a series of calibrations, discussed in [72]. The required coating would mean that, if the backplate surface temperature is to be measured, a different backplate must be installed compared to the one required for background-orientated or regular Schlieren imaging.

Finally, another experimental goal discussed in chapter 1 is to validate modelling assumptions. One of these is the assumption of adiabatic flows, meaning no heat flux through the boundary walls. Head [4] suggest using thermocouples to measure temperature at a small distance from the wall surface. However, infrared thermal imaging provides a non-intrusive method for detecting the wall surface temperature. This means that infrared thermography can address both research goals.

2.5.7. Instrumentation Selection and Compatibility

To conclude this overview of measurement techniques, the most promising measurement techniques are selected for the research goals of the linear cascade test section. The research goals discussed in chapter 1 include obtaining validation data for numerical analysis tools, as well as evaluating the performance of different stator geometries to validate and develop design tools and guidelines. For this second goal, Hariharan [6] has investigated the relevant system response quantities to characterise

stator performance. He identified, among others, the pressure loss coefficient and exit flow uniformity coefficient, which can be experimentally determined using a combination of static pressure measurements, Schlieren flow visualisations and PIV.

All of these measurement techniques have been used in the planar nozzle test section of the *ORCHID* facility, reducing the complexity of implementation in the linear cascade test section. For static pressure measurements, the existing Scanivalve system can be used. For Schlieren imaging, the currently employed z-type setup must be replaced by a double-passage setup. The reason for this is that a z-type setup requires optical access on both sides of the cascade, which would require the cascade blades to be mounted on the windows. Instead, for a double-passage system, the blades can be mounded on a steel backplate. This backplate should have a mirror-like surface finish to allow the light to reflect back to the camera of the Schlieren setup. Finally, like Schlieren imaging, PIV has also been implemented in the planar nozzle test section. Initial results show that PIV can successfully be used in supersonic NICFD flows; however, some hardware limitations are currently being addressed in further research.

In addition to determining response quantities, the velocity field data that can be measured using PIV can be used to perform validation studies of numerical models. This would be a valuable addition to the current state of the art, as the overview of current NICFD experiments in section 2.4 shows that this type of validation has not been done for linear cascade flows. The same holds for the density field, which can be determined using background-orientated Schlieren. For this technique, the backplate of the cascade would have to be swapped out for one with a laser-engraved pattern of dots instead of the mirror polished backplate used for the regular Schlieren imaging.

The review of intrusive measurement techniques like Pitot probes and HWA shows that the high-density supersonic flow in the test section significantly complicates their implementation. Complicated traversing and sealing mechanisms are required to provide access to the test section. Furthermore, the high flow density exerts a significant force on the instruments. Most critically, these intrusive techniques significantly distort the flow around them, which is especially limiting in the small spacings inside the cascade passages.

Finally, although it requires a complicated calibration and some test section modifications, infrared thermal imaging has the potential to provide valuable data which can validate both the adiabatic flow modelling assumption and the ability of numerical solvers to predict boundary layer behaviour. For this reason, a detailed study on the implementation of thermal imaging for the linear cascade test section should be considered.

2.6. Previous Work Towards a Linear Cascade Test Section

The work within this report is in fact not the first step toward a linear cascade test section for the *ORCHID* facility. Groen [73], Haur [74], and Zuna [75] have created a detailed preliminary design of the cascade test section, including the housing, settling chamber, and receiver. They focused on the mechanical design of the test section, including integration into the *ORCHID* facility, numerical structural analysis and an investigation of the housing seals. In addition to this, a CFD analysis was performed to find a housing design ahead of the cascade that could transition to flow from a circular inlet to a rectangular domain more effectively and provide the most uniform flow at the cascade entrance. The final design of the complete assembly is shown in Figure 2.15. Here, Figure 2.15a shows a detailed drawing of the complete setup of the test section with the indicated components. Furthermore, Figure 2.15b shows a cross section of the assembly to show the flow path through the assembly.

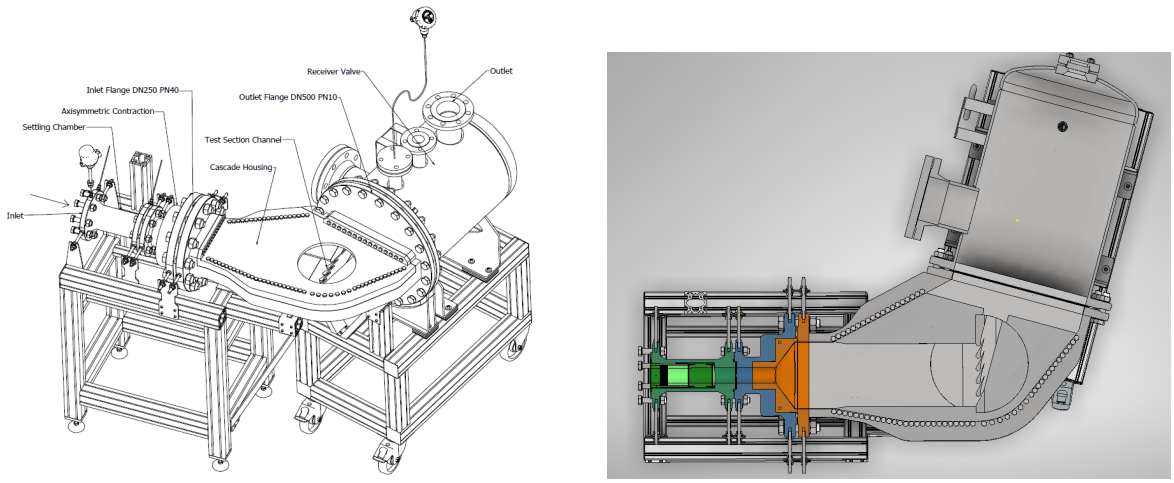

(a) Detailed drawing of the complete test section setup

(b) Internal flow path through the test section

Figure 2.15: Preliminary design of the *ORCHID* linear cascade test section[73]

Using this preliminary design, Hariharan [6] investigated relevant response quantities to characterise stator performance. In addition, an uncertainty quantification study was performed, showing that the influence of critical point uncertainty is dominant over the inlet pressure and viscosity for NICFD flows. Furthermore, Vello [7] used the preliminary design of the cascade test section to adapt the validation infrastructure used for the planar nozzle test section for linear cascade application. This infrastructure was then used to compare *SU2* simulations to three-dimensional simulations using a commercial solver. The results show a positive comparison, where the error was lower than the error of most response quantities.

3

Methodology

Building on the theoretical basis and state of the art of NICFD experiments established in the literature review of the previous chapter, this chapter describes the methodology used for the design and numerical analysis of a linear stator cascade test section for the *ORCHID* facility. First, section 3.1 discusses the selection of expansion conditions, based on the objectives of the experiments and the constraints of the facility. Then, section 3.2 shows the design process of the stator vane geometries as well as the design of the complete cascade. Finally, section 3.3 explains the approach for the numerical analysis of the test section. This includes domain discretisation, numerical solver setup, and some solution verification steps.

3.1. Selection of Experimental Conditions

The first step to design the linear stator cascade test section is to select the experimental conditions, as well as to determine the geometrical constraints of the linear stator cascade. To select the test conditions, requirements and constraints must be determined. Finally, the scale and geometry of the stator vanes can be designed based on the experimental conditions.

3.1.1. Constraints and Requirements

In order to select the experimental conditions, the requirements for the experiments must be formulated and the constraints identified. The first step is to set a range for the nondimensional flow properties: the exit Mach number and the Reynolds number. Since the goal is to investigate the flow through a supersonic stator cascade, the exit Mach number will be required to be between 1.3 and 2.0. The Reynolds number should be between 1 and 8 million. These are common ranges for supersonic stator vanes.

Next, the required flow nonideality must be investigated. For this, three experiments will be considered. For the first experiment, the flow must be as close as possible to an ideal flow. This means that the fundamental derivative of gas dynamics should be close to or above unity: $\Gamma \gtrsim 1$ (see section 2.2). This condition (referred to as the ”ideal” condition) will serve as a baseline. Next, a ”nonideal” condition that has $\Gamma, Z < 1$ will be investigated. This condition will require that there is a monotonic evolution of Γ across the expansion. The final condition will be nonideal and nonmonotonic (hereafter referred to as the ”nonmonotonic” condition) will be required to have a nonmonotonic evolution of Γ while keeping $\Gamma < 1$.

There are two sources of constraints for the thermodynamic design space, the working fluid and the *ORCHID* capabilities. The organic working fluid used in the *ORCHID* is Hexamethyldisiloxane (MM). MM starts to dissociate at 300 $^\circ$C[4], which will be the upper temperature limit. Furthermore, to avoid condensation, the entire expansion must avoid the saturation curve. For this reason, a 5% entropy margin will be used between the saturation curve (s_{sat}) and the entropy of the isentropic expansion lines. This means that the minimum entropy is equal to 1.05 times the maximum saturation entropy within the temperature range of the isentropic expansion. In this way, no condensation will occur during

expansion. A visualisation of the resulting constraint in the Ts-diagram is shown in Figure 3.1. To avoid any part of the expansion to get within the 5% entropy margin of the saturation curve, the expansion lines must be placed to the right of the minimum entropy line (the solid red line). The *ORCHID* was designed with a maximum operating pressure of 25 bar and a maximum operating temperature of 320 °C[4]. In this case, it is clear that the thermal dissociation is the limiting factor for the maximum operating temperature. A subatmospheric exit pressure can be supported by the *ORCHID*, however an exact lower limit is unknown. For this reason a value of 0.5 bar will be assumed as the lower limit to be safe. An overview of the design requirements and constraints can be seen in Table 3.1. Since the constraints must be applied to the Ts-diagram, which uses reduced temperature and entropy, the constraints will also be converted to reduced coefficients by dividing by the critical temperature and entropy respectively.

Table 3.1: Design requirements and constraints for the flow conditions

Requirements	
Exit Mach number	$1.3 < M < 2.0$
Reynolds number	$1\,\text{million} < Re < 8\,\text{million}$
Constraints	
Maximum temperature	$T_{\max} = 300\,^{\circ}\text{C}$
Maximum pressure	$P_{\max} = 25\,\text{bar}$
Minimum pressure	$P_{\min} = 0.5\,\text{bar}$
Minimum entropy	$s_{\min} = 1.05 \cdot \max(s_{\text{sat}}(T_{\text{inlet}} \rightarrow T_{\text{outlet}}))$

3.1.2. Selection of Flow Conditions

Next, isentropic expansion calculations are performed to quickly evaluate the expansion properties. The expansions can be represented within the thermodynamic design space as expansion lines in a Ts-diagram. Three design variables must be selected to set the isentropic expansion lines, namely the total inlet pressure $P_{\text{t,inlet}}$, total inlet temperature $T_{\text{t,inlet}}$, and the static outlet pressure P_{outlet}. It is assumed that the inlet velocity is low, thus the total and static inlet conditions are equal. From these variables, initial estimates can be made for the exit Mach number and throat conditions based on the assumption of isentropic expansion. This neglects any viscous losses and boundary layer formation, which will result in an overestimation of the exit Mach number and mass flow rate. For the mass flow rate, it is critical to stay below the maximum mass flow rate that can be provided by the *ORCHID* facility, so a conservative estimate is desirable.

To calculate the isentropic expansion of an organic vapour in nonideal conditions, the *NiceProp*[76] tool is used. This tool uses *REFPROP* (see section 2.3) to determine the properties of the working fluid under the varying thermodynamic conditions for a given isentropic expansion. Additionally, *NiceProp* can be used to plot the expansion lines in a Ts-diagram, as well as to plot the evolution of different properties across the expansion. This information can be used to select the design conditions.

The Ts-diagram for MM can be seen in Figure 3.1. The diagram shows the selected expansion lines in dark grey, the compressibility factor Z, the isolines of the fundamental derivative Γ, the isobaric lines at the inlet and outlet conditions of each expansion in light grey, the two-phase region bound by the vaporisation curve, and the critical isobar in red separating the sub- and supercritical regions. The axis of the plot are in terms of reduced temperature T_{r} and entropy s_{r}, which are the ratio of temperature and entropy over the critical temperature and entropy of the fluid receptively.

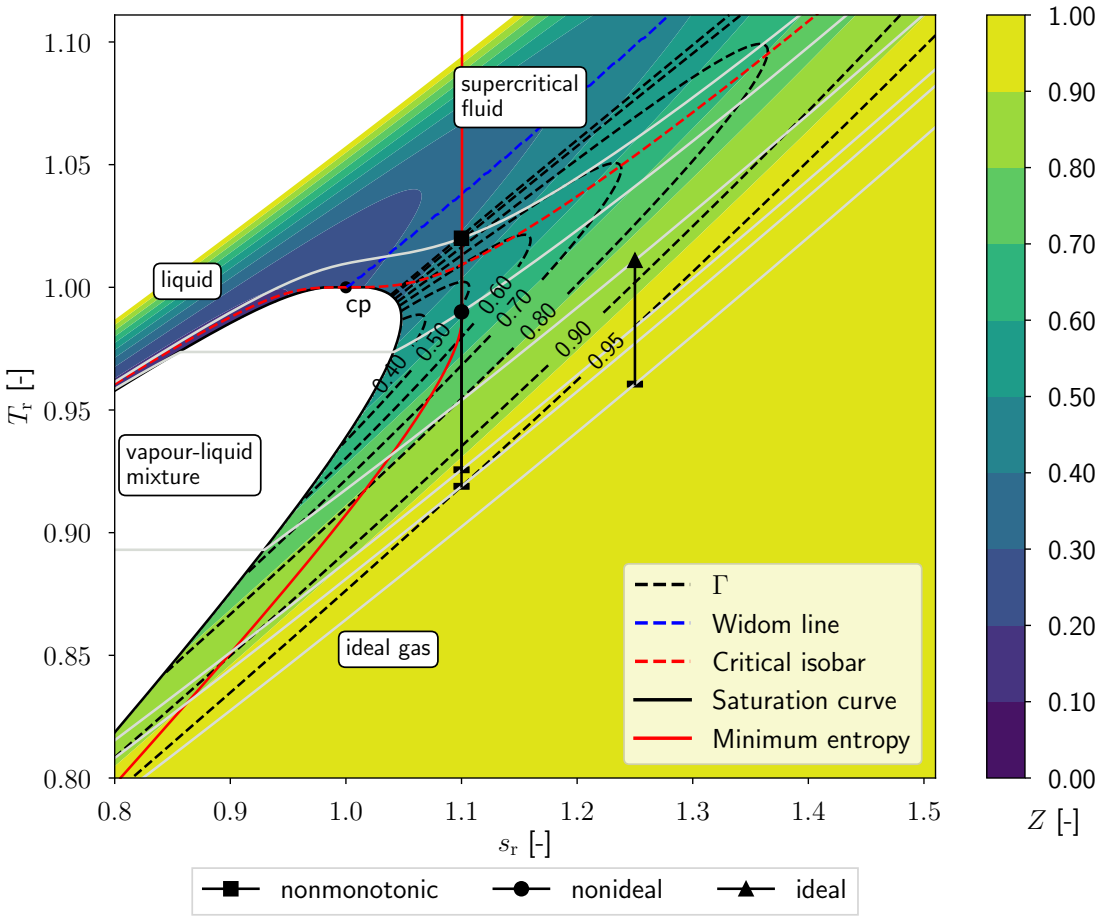

Figure 3.1: Ts-diagram containing the three isentropic expansion lines of the design conditions

From the Ts-diagram, it becomes clear that the fundamental derivative of gas dynamics is lower closer to the critical point. So, in order to achieve the most nonideal fluid effects, the entropy of the nonmonotonic and nonideal expansions will be set to the minimal margin to the saturation curve as discussed in the design constraints. For the ideal condition, the value will be set higher to keep the fundamental derivative high. The length of the expansion lines is dictated by the total-to-static pressure ratio β_{ts}, which is the ratio between the total inlet pressure and the static outlet pressure. The exit Mach number can be controlled with this ratio. A pressure ratio is determined for every condition so the exit Mach numbers for all conditions are equal and within the required range. If the inlet conditions of one of the design conditions change, the pressure ratio is changed again to match the required Mach number.

Next, the total inlet temperature of the expansion lines can be set to fit the requirements for the evolution of the fundamental derivative. Figure 3.2a shows the evolution of the fundamental derivative and the compressibility factor against Mach number for expansions with increasing total inlet temperature (and thus increasing lenght of the expansion line in the Ts-diagram). For the nonmonotonic expansion, the goal is to get the peak of the fundamental derivative as close to the throat (Mach 1) as possible, without increasing the fundamental derivative above one. This results in the selection of the middle (blue) expansion for the nonmonotonic case. The monotonic, nonideal expansion is found by lowering the nonmonotonic expansion line in the Ts-diagram (by lowering the total inlet temperature) until only a monotonic evolution of the fundamental derivative is present. Finally, the ideal expansion is found by setting the total inlet temperature so the outlet pressure stays above 0.5 bar, as required. This results in the most ideal expansion possible.

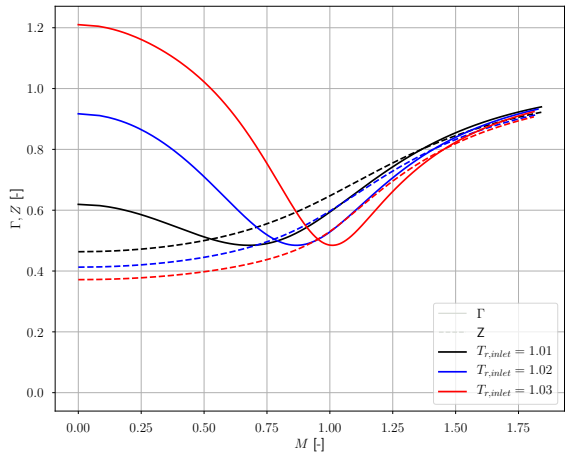

(a) Evolution of compressibility factor Z and fundamental derivative Γ against Mach number for nonmonotonic expansions with increasing total inlet temperature

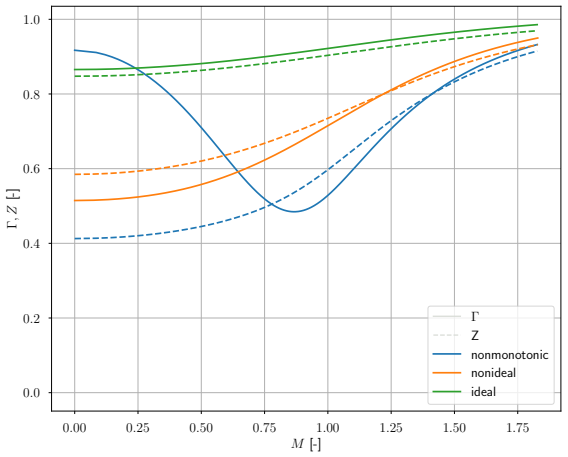

(b) Evolution of compressibility factor Z and fundamental derivative Γ against Mach number for the three selected design conditions

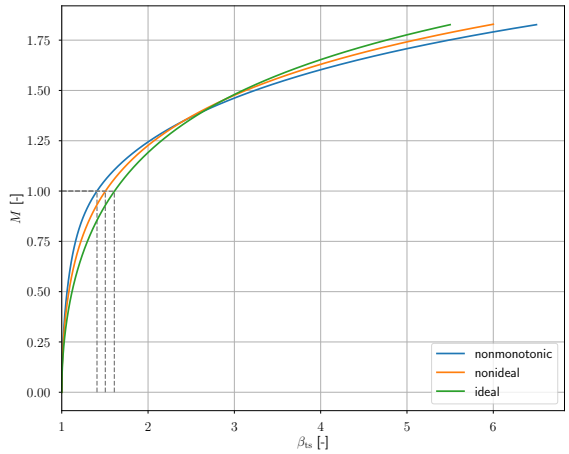

(c) Evolution of Mach number against total-to-static pressure ratio β_{ts} for the three selected design conditions

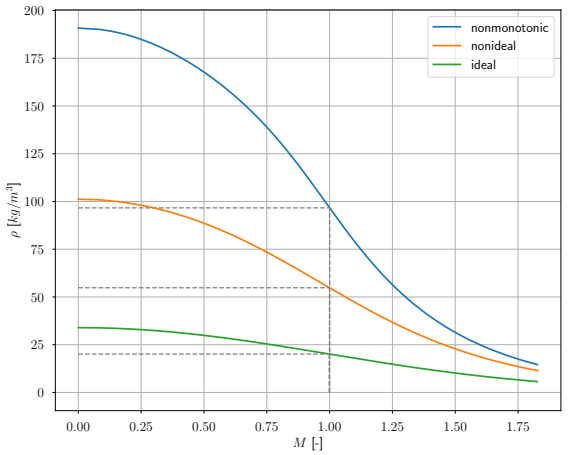

(d) Evolution of density number against Mach number for the three selected design conditions

Figure 3.2: Evolution of flow properties through the isentropic expansions

Figure 3.2b shows the evolution of the fundamental derivative and compressibility factor for the final design conditions and Figure 3.1 shows the isentropic expansion lines of the final design conditions plotted in the Ts-diagram. The final properties of the expansions are listed in Table 3.2. Furthermore, Figure 3.2c shows the effect of nonideality on the Mach number distribution, while Figure 3.2d shows that the more nonideal expansions have a significantly higher density in the throat (indicated by the dashed line). This means that the available throat area will be significantly reduced considering a maximum mass flow rate, which will be further analysed in the next section.

Table 3.2: Isentropic expansion properties for the three selected conditions

		Nonmonotonic	Nonideal	Ideal
Reduced inlet entropy	s_r [−]	1.10	1.10	1.25
Reduced total inlet temperature	T_r [−]	1.02	0.99	1.011
Total-to-static pressure ratio	β_ts [−]	6.5	6.0	5.5
Total inlet temperature	$T_\mathrm{t,inlet}$ [K]	529.1	513.5	524.4
Total inlet pressure	$P_\mathrm{t,inlet}$ [bar]	21.33	15.56	7.73
Static outlet pressure	P_outlet [bar]	3.28	2.39	1.83
Exit Mach number	M_outlet [−]	1.83	1.83	1.83
Average compressibility factor	Z_avg [−]	0.67	0.77	0.91
Average fundamental derivative	Γ_avg [−]	0.69	0.75	0.93

3.1.3. Geometrical Cascade Constraints

The thermal power that can be delivered by the *ORCHID* facility is a critical design constraint to consider. Together with the expansion conditions, the thermal power determines the maximum mass flow rate that can be delivered by the system. This maximum mass flow rate will determine the maximum total throat area of the stator cascade, since the throat of a passage between supersonic stator vanes is choked. This means that for a given number of blades (and thus flow passages), the maximum throat area will be dictated by this thermal power.

During the first commissioning experiments performed by Head [4], it became clear that the thermal power available was lower than expected based on the design of the facility. The throat area of the planar nozzle used during these tests was reduced from 200 mm^2 to 150 mm^2 to reach the design conditions of the experiment. Since no exact thermal power limit is known, it will be derived from the commissioning experiment conditions of the 150 mm^2 nozzle test section.

The thermal input power $\dot{Q}_{in}$ can be determined using

$$\dot{Q}_\mathrm{in} = \dot{m}(h_\mathrm{inlet} - h_8) \propto \dot{m} h_\mathrm{inlet} = A_\mathrm{th}\rho_\mathrm{th}v_\mathrm{th}h_\mathrm{inlet}, \tag{3.1}$$

where $\dot{m}$ is the working fluid mass flow rate, A_th is the throat area, ρ_th is the density in the throat, v_th is the velocity in the throat and h_inlet and h_8 are the enthalpies in the test section inlet station and regenerator outlet station respectively (see Figure 2.8a, where the inlet staion is station 1 in the diagram)[4]. This follows from the fact that the heater thermal power is equal to the power required at the cascade inlet minus the power recovered by the regenerator. The second half of the equation implies that the change in thermal recovery by the regenerator is minimal in different flow conditions. Assuming that the efficiency of the regenerator is constant, the amount of energy that the regenerator can recover depends on the energy available in the flow leaving the cascade test section. To verify that this is the case, the outflow enthalpy of the test section $h_\mathrm{outlet} = h(P_\mathrm{outlet}, T_\mathrm{outlet})_s$ is multiplied by the calculated maximum mass flow rate $\dot{m}$ for the three design conditions and the flow condition through the commissioning planar nozzle test section assuming isentropic expansion in all cases.

To determine the maximum mass flow rate, first the thermal power of the planar nozzle commissioning experiment is determined using Equation 3.1 with total inlet conditions and throat area of 150 mm^2. This is assumed to be the maximum thermal power of the flow at the inlet of the test section. Then, this power is used with the conditions of the three design cases to find the maximum mass flow rate for each condition by dividing the thermal power by the inlet enthalpy $h_\mathrm{inlet} = h(P_\mathrm{t,inlet}, T_\mathrm{t,inlet})$.

To verify the previously mentioned heat exchanger assumption, the energy in the outlet flow for each design condition at the maximum mass flow rate can be seen in Table 3.3. The results show that all design conditions exceed the available energy of the planar nozzle conditions, indicating that the regenerator can recover more energy from the flow. This would support the assumption that the regenerator exit enthalpy h_8 can be neglected from Equation 3.1, assuming that the regenerator efficiency stays constant. Critically, this analysis is performed assuming an isentropic expansion, thus neglecting any losses during the expansion. For this analysis to be valid, the losses for each experiment must be comparable. It is unlikely that a cascade experiment has similar losses compared to the planar nozzle since

a complex pattern of wakes, shocks, and expansion fans is formed in the former, but the magnitude of the differences is difficult to predict. However, the effect of the increase in losses is expected to be small.

Table 3.3: Outlet flow thermal power for all experiment conditions at maximum mass flow rate, compared to the planar nozzle

	Planar nozzle	**Nonmonotonic**	**Nonideal**	**Ideal**
$h_{\text{outlet}} \cdot \dot{m}$ [kW_{th}]	446	458	456	456
Δ [%]	–	+2.52	+2.24	+2.24

Before finalising this analysis, an issue with the thermal power was raised by researchers operating the *ORCHID*. A decreasing trend for the thermal power is observed over time. This is caused by wear and degradation of the heat exchangers in the *ORCHID* facility. For this reason, it was recommended to reduce the maximum throat area by 15 to 20 percent (since this is directly proportional to the maximum thermal power). Since there is also the unknown of the expansion losses, the conservative value of 20% will be used. With this, the final relation between the flow conditions and the maximum cascade dimensions can be derived as follows:

$$\begin{aligned} \dot{Q}_{\text{inlet,max}} &= \dot{Q}_{\text{inlet,noz}} \cdot \text{SF} \\ h_{\text{inlet,casc}} \cdot \dot{m}_{\text{max,casc}} &= h_{\text{inlet,noz}} \cdot \dot{m}_{\text{noz}} \cdot \text{SF} \\ h_{\text{inlet,casc}} \cdot w_{\text{th}} \cdot h_{\text{bl}} \cdot n_{\text{pass}} \cdot \rho_{\text{th}} \cdot v_{\text{th}} &= 431940 \cdot 1.1592 \cdot 0.8 \approx 400\,\text{kW}_{\text{th}}, \end{aligned} \tag{3.2}$$

where the cascade inlet enthalpy $h_{\text{inlet,casc}}$, the flow density in the throat ρ_{th} and throat velocity v_{th} are set by the chosen expansion conditions. This means that the product of throat width w_{th}, blade height h_{bl} and number of passages n_{pass} is constrained by a constant for each thermodynamic condition considered. This constant is the maximum total throat area of the cascade A_{th}. The resulting dimensional limits of the isentropic expansions can be found in Table 3.4.

Table 3.4: Dimensional cascade properties based on the maximum thermal power of the *ORCHID* and the thermodynamic conditions of the expansions

		Nonmonotonic	**Nonideal**	**Ideal**
Maximum mass flow rate	$\dot{m}_{\text{max}}$ [kg/s]	0.951	0.961	0.857
Maximum total throat area	A_{th} [mm^2]	102.4	147.4	285.8

3.2. Stator Cascade Design

With the expansion conditions and the respective maximum mass flow rates determined in the previous section, the stator cascade can be designed. First, the stator vane geometries are generated. Then, the geometries are scaled to meet the mass flow rate and Reynolds number constraints determined in the previous section, resulting in two final cascade geometries which will be used for the numerical analysis.

3.2.1. Stator Design

Now that the inlet and outlet flow conditions are selected and the geometrical constraints are defined, the stator vane geometry can be designed. For this, the *OpenMOC*[77] tool is used. This tool uses the Method of Characteristics (MoC) to calculate the shape of the diverging portion of the nozzle, to generate a parallel uniform flow for specific expansion conditions. This shape forms part of the passage between two blades (see section 2.1). After the nozzle shape is generated, the geometry is scaled to achieve the desired mass flow rate per unit blade height. Then, this nozzle geometry is used to determine the supersonic stator vane geometry. Like the *NiceProp* tool, *OpenMOC* uses the *REFPROP* fluid model database to determine the fluid properties of MM. The diverging nozzle shape is calculated

based on the total inlet conditions and the required nozzle outlet Mach number. A detailed explanation of the MoC procedure is described by Anand [77].

The procedure for designing the stator vane based on the diverging nozzle shape from the MoC is shown schematically in Figure 3.3. The pitch of the cascade is first determined using the nozzle exit width (distance between the points ss_a and ps_a^*), the width of the trailing edge specified by the user t and the design flow angle ϕ_a. Note that Figure 3.3 indicates a right angle in ss_a. This approach has been revised such that the line originating from the point ss_a is tangent to the nozzle outlet (the curve between ss_o and ss_a at the exit of the nozzle (point ss_a), which is not necessarily perpendicular to the exit plane of the nozzle.

To define the stator geometry, the diverging nozzle geometry is first rotated by the design flow angle ϕ_a around the centre of the throat. Then, the bottom curve of the diverging nozzle is shifted up by the pitch p. After this, a half-circle is added to form the trailing edge. A straight line is drawn between the points ss_a and ss_{te} to connect the nozzle shapes behind the diverging section of the blade. Then, the points ss_o and ps_o are connected using a nonuniform rational basis spline, forming the leading edge of the blade. The control points of this spline could be used for blade shape optimisation, which is outside the scope of this research. Note that the control points in Figure 3.3, while still indicative of the general approach, have been altered and therefore are no longer representative. As the procedure described is similar to the procedure for radial stator geometries, additional information on the procedure can also be found in the work of Cappiello et al. [78].

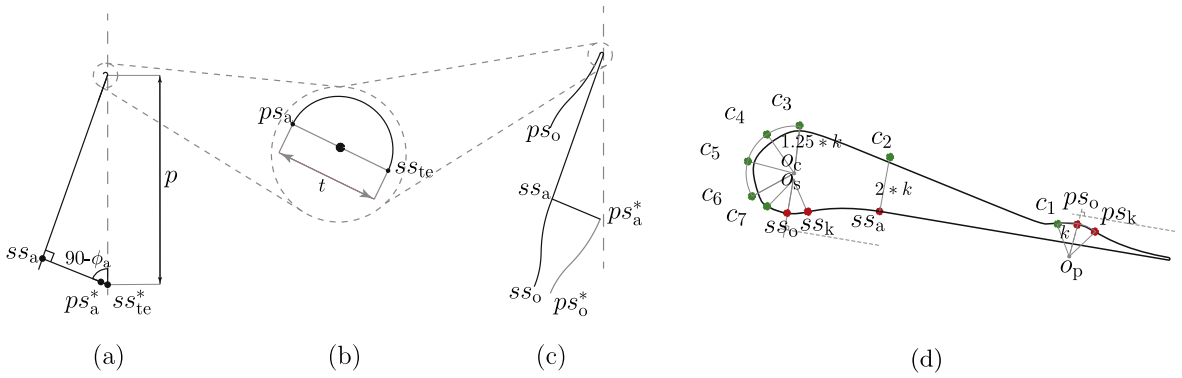

Figure 3.3: Schematic of the procedure to obtain the stator geometry from the diverging nozzle shape, (a) semi-bladed region, (b) trailing edge, (c) semi-blade region and diverging section, (d) blade geometry with spline control points[79]

Furthermore, since one of the goals of this work is to compare blades with a constant trailing edge thickness to pitch ratio, the *OpenMOC* tool was expanded to include this ratio as a design parameter. To determine the correct trailing edge thickness, an initial guess is used to determine a blade pitch value. Then, the trailing edge thickness is iteratively adapted and the pitch is recalculated until the design converges to the required ratio.

Another important design parameter for supersonic stators that is not covered by *OpenMOC* is the post-expansion ratio. The post-expansion ratio dictates the amount of expansion in the area of uncovered turning. This is the area behind the diverging nozzle shape that is covered only by a stator vane, as seen in Figure 2.1. The post-expansion ratio is defined as $\beta_\mathrm{PE} = \frac{P_\mathrm{a}}{P_\mathrm{outlet}}$, where P_a is the pressure at the exit of the nozzle computed by the MoC and P_outlet is the pressure at the outlet of the stator. Anand, Colonna, and Pini [79] investigated the optimal post-expansion ratio for fluids of complex molecules, including MM. They found that the optimal post-expansion ratio for MM at a total-to-static pressure ratio of 6.0 and a flow angle of 70° was 1.06. The effect of solidity, flow angle, and pressure ratio on the optimal post-expansion ratio were also investigated in the same work. From the results, it can be concluded that the solidity has a limited effect on the optimal post-expansion ratio. Furthermore, the flow angle and total-to-static expansion are close enough to the design conditions (75° and 6.5 to 5.5 respectively) to make the post-expansion ratio valid for this application.

Next, the nozzle expansion ratio can be found using the total-to-static expansion ratio and the optimal

post-expansion ratio based on their definitions:

$$\beta_{\text{noz}} = \frac{P_{\text{inlet}}}{p_{\text{a}}} = \frac{\beta_{\text{ts}}}{\beta_{\text{PE,opt}}} = \frac{6.5}{1.185} = 5.485. \tag{3.3}$$

This pressure ratio can then be used with the inlet conditions to determine the nozzle exit Mach number using *NiceProp*. This can then be used in *OpenMOC* to calculate the shape of the divergent nozzle. This shape is then used to create the stator vane geometry.

3.2.2. Constant Reynolds Number Cascade Design

As discussed in chapter 1, one of the design goals for the cascade test section is to design a stator vane for each expansion condition considered, while keeping the Reynolds number, Mach number, and trailing edge-to-pitch ratio constant. The exit Mach number has already been considered in the expansion selection. The trailing edge-to-pitch ratio will be set to 2%, which is a common but non-demanding value considering the manufacturability of the blades. The Reynolds number (Re) for stator vanes is defined based on the outlet conditions as described by

$$Re = \frac{C \cdot \rho_{\text{outlet}} \cdot v_{\text{outlet}}}{\mu_{\text{outlet}}} \tag{3.4}$$

, where C is the length of the stator vane chord, ρ_{outlet} is the outlet flow density, v_{outlet} is the outlet flow velocity and μ_{outlet} the outlet dynamic viscosity. It becomes clear that, for a given expansion, all flow variables are set, and the Reynolds number is directly proportional to the chord length. For this reason, to match the Reynolds number of the different cascade designs, the blades must be scaled based on the required Reynolds number. The resulting stator geometries can be seen in Figure 3.4b for the three design conditions. To inspect the effect of the flow condition on the stator geometry, all geometries have been plotted at the same (arbitrary) throat width in Figure 3.4a. In addition, the most important specifications of the geometries are listed in Table 3.5. The maximum allowable blade height is determined using the maximum total throat area in Table 3.4 and dividing by the throat width and the number of passages.

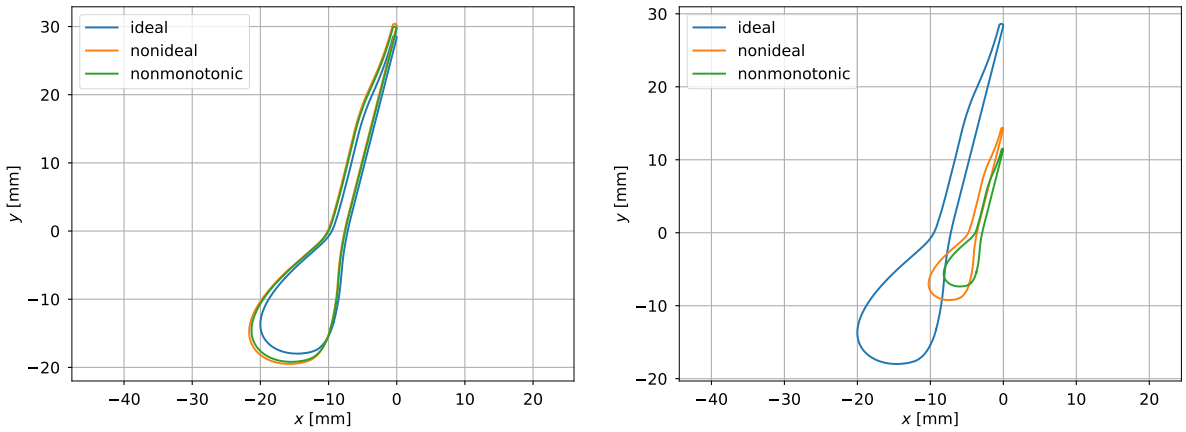

(a) Constant throat width

(b) Constant Reynolds number of 7 million

Figure 3.4: Stator vane geometries for the three design conditions

Table 3.5: Specifications of the constant Reynolds number blade designs

		General		
Outflow Mach number	M_{outlet} [−]	1.83		
Post-expansion ratio	$\beta_{\text{PE,opt}}$ [−]	1.06		
Trailing edge-to-pitch ratio	t/p [−]	0.02		
Design flow angle	ϕ_{a} [°]	75		
		Nonmonotonic	**Nonideal**	**Ideal**
Total-to-static pressure ratio	β_{ts} [−]	6.5	6.0	5.5
Trailing edge thickness	t [mm]	0.228	0.285	0.567
Throat width	w_{th} [mm]	1.42	1.75	3.70
Chord length	C [mm]	18.9	23.6	46.6
Pitch	p [mm]	11.4	14.2	28.3
Solidity	$\sigma(=\frac{C}{p})$ [−]	1.66	1.66	1.65
Reynolds number	Re [million]	7.00	7.00	7.00
Maximum blade height, 5 passage cascade	$h_{\text{bl,5pass}}$ [mm]	14.4	16.9	15.5
Maximum blade height, 7 passage cascade	$h_{\text{bl,7pass}}$ [mm]	10.3	12.1	11.1

From these results, several conclusions can be drawn. First of all, from Figure 3.4a, it becomes clear that the stator geometries are very comparable. Only the ideal condition produces a blade with a slightly shorter diverging nozzle shape, resulting in a shorter blade overall. However, the nonmonotonic and nonideal blade designs are almost identical. Furthermore, Table 3.5 shows that the nonmonotonic condition will restrict the height of the blade, as it is not desirable to design a test section for different blade heights.

The effects of the Reynolds number scaling are significant. The nonideal and nonmonotonic blades become very small, while the ideal blade has about twice the chord length. This is problematic for two reasons. First of all, manufacturing and instrumenting such small blades is expected to be very challenging and costly. One could increase the design Reynolds number, but this would also increase the size of the ideal blade geometry. The ratio between the blades is fixed by the selected conditions. The difference in pitch will make it more difficult to integrate all blades in the same test section, increasing the cost of the experimental campaign.

Additionally, in turbulent boundary layer regimes common in high Reynolds number turbomachinery blading like this, the dissipation coefficient is often considered constant since there is a weak variation of dissipation coefficient with momentum thickness based Reynolds number[80]. Because of this, the effect of the difference in Reynolds number on the boundary layer losses will be minimal.

Because of these reasons, it is decided to remove the Reynolds number consistency constraint. Instead, a single blade design will be used to perform experiments for all three expansions. In this way, no cascades need to be swapped out, reducing the duration and cost of the experimental campaign. An additional benefit is that the blades used for each test will be identical, aiding to the comparability between the different experiments.

3.2.3. Single Blade Geometry Cascade Design

With the Reynolds number as a free variable, a new blade scaling method is required. This method will be based on the mass flow rate constraint derived in Equation 3.2, with which the maximum total throat area of the cascade was calculated for each expansion condition. From Table 3.4, it can be concluded that the nonmonotonic expansion has the lowest allowable total throat area. This is expected since the expansion has a much higher density in the throat, which can be seen in Figure 3.2d. This means that the cascade geometry will be constrained by the nonmonotonic expansion condition.

From the maximum total throat area of the nonmonotonic expansion, the throat area of a single passage can be found by dividing the total area by the number of passages. To minimise the effects of wall-reflected shock waves and to maximise the flow periodicity, the number of passages should be as high as possible. To find the largest feasible number of passages, Figure 3.5 is used. In this graph, the

throat width is plotted against the blade height for a given number of passages. In this case, we want to consider only an odd number of passages, since this will result in one passage in the centre of the cascade with equal distance to both outer walls. Additionally, axes showing the chord length of the stator vane and the Reynolds number for ideal thermodynamic conditions are added because they are directly proportional to the throat width. To select the final design points, a line is drawn that represents a blade height to throat width ratio of two. In this way, the relative distance between the midplane and the walls of the passage remains constant when comparing different numbers of passages. A ratio of two-to-one is chosen to ensure that the midplane is free from any boundary layer effects generated by the top and bottom walls.

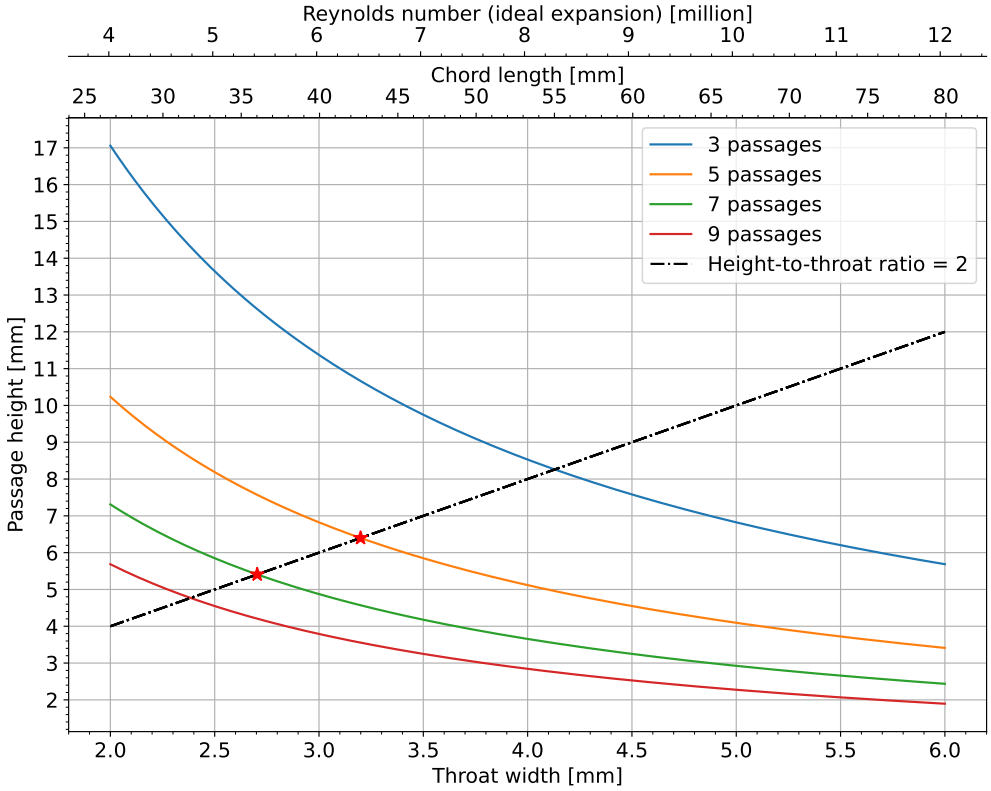

Figure 3.5: Throat dimensions for different number of passages based on the maximum allowable total throat area for the nonmonotonic expansion

The intersection points of the dashed line with the passage curves are the design points that will be considered. To investigate the effect of increasing the number of passages, two designs are selected for detailed CFD analysis. It is expected that three passages will not be enough to produce a periodic flow in the centre passage. Thus, five- and seven-passage designs will be considered, which are marked in Figure 3.5. By choosing to analyse two different blade scales, both cascades have the largest blade scales possible under the mass flow rate constraint. This is important since larger blade scales allow for a higher measurement resolution when using optical measurement techniques.

The final consideration before moving on to the detailed flow analysis is which blade geometry will be used. That is, which expansion condition should be used for the blade design. Based on Figure 3.4a, it was determined that the geometries designed for the nonmonotonic and nonideal expansions were very similar, while the ideal expansion geometry deviated slightly. The blade geometry generated with the nonmonotonic expansion conditions is chosen for the cascade, since it is the condition of most interest. Scaling this geometry to the throat widths of the design points results in the blade geometries in Figure 3.6. The specifications for both geometries are listed in Table 3.6.

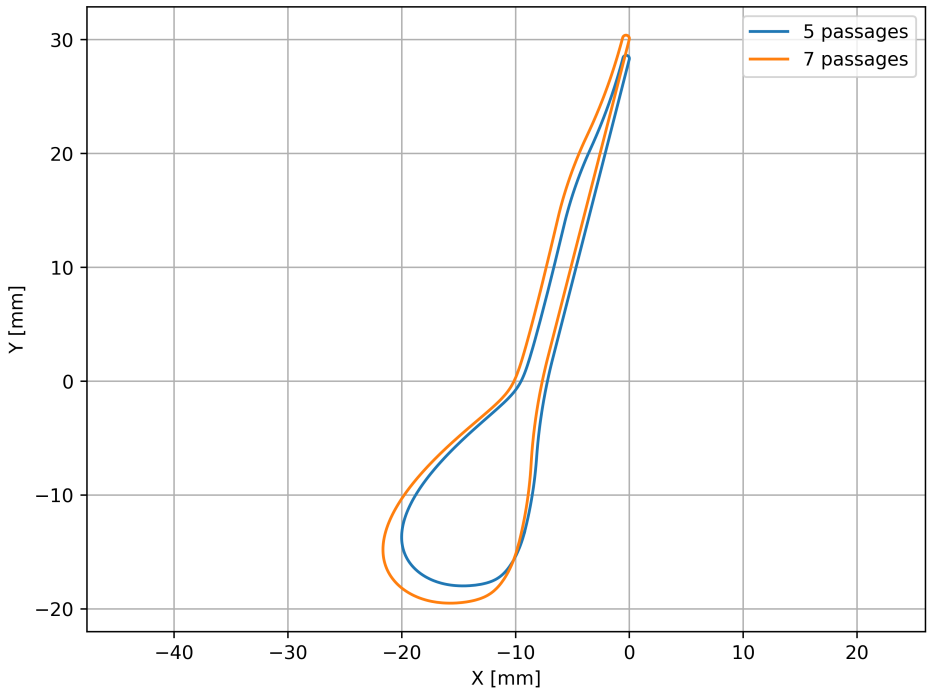

Figure 3.6: Blade geometries scaled for maximum throat area for five and seven passage cascades

Table 3.6: Specifications of the blade designs for the five and seven passage cascades

		General	
Outflow Mach number	M_{outlet} [−]	1.83	
Post-expansion ratio	$\beta_{\text{PE,opt}}$ [−]	1.06	
Trailing edge-to-pitch ratio	t/p [%]	2	
Design flow angle	ϕ_{a} [°]	75	
Solidity	$\sigma(=\frac{C}{p})$ [−]	1.66	
		5 passages	**7 passages**
Trailing edge thickness	t [mm]	0.513	0.434
Blade height	h_{bl} [mm]	6.40	5.41
Throat width	w_{th} [mm]	3.20	2.71
Chord length	C [mm]	42.7	36.1
Pitch	p [mm]	25.7	21.7
Reynolds number ideal expansion	Re_{ideal} [million]	6.42	5.42
Reynolds number nonideal expansion	Re_{nonid} [million]	12.7	10.7
Reynolds number nonmonotonic expansion	Re_{nonm} [million]	15.8	13.4

3.3. CFD Approach

In order to determine the optimal design of the test section, a CFD analysis is performed comparing multiple layouts. First, the flow fields through an infinite cascade for the three expansion conditions are computed. Recalling that an infinite cascade represents the real domain of a blade in an annular cascade, these flow fields will serve as the reference for the midplane flow through the centre passage in the finite cascade test section. Furthermore, comparing the infinite cascade flow fields of the three expansions can provide insight into the effects of flow nonideality. Next, the flow fields through both the five- and seven-passage cascades are analysed and compared to the infinite cascade results.

In this section, first, the discretisation of both the infinite cascade and the cascade test sections is presented. Then, the numerical solver and its settings are discussed. Next, some post-processing

steps that are used to interpret the solver results are highlighted. After this, the accuracy of a Cubic Equation of State (discussed in section 2.3) is verified for the most non-ideal fluid condition. Lastly, a comparison is made between the results of a three-dimensional and a two-dimensional numerical domain. The aim of this comparison is to verify that the measurement plane of the three-dimensional cascade (the midplane) is free from boundary layer effects originating from the endwalls enclosing the cascade and can thus be analysed using a two-dimensional domain.

3.3.1. Domain discretisation

There are four main domains to discretise (mesh): *(1)* the passage for the infinite cascade, *(2)* a two-dimensional five-passage cascade test section, *(3)* a seven-passage test section, and *(4)* a three-dimensional test section. In addition, meshes with altered tailboard angles are made.

The periodic single-passage domain for the infinite cascade is the simplest to discretise. This domain utilises periodic boundary conditions to simulate an infinite cascade, as shown in Figure 3.7a. This boundary condition is explained in more detail in the next section. This type of domain is commonly used to evaluate turbomachinery blade designs, since it allows for the evaluation of the mean-line flow of a blade in a full cascade, using a small domain. This allows for relatively few elements and thus quick computation.

Due to the commonality of this domain, specialised meshing tools exist to quickly generate an unstructured mesh for a given blade geometry. In this case, *UMG2*[81] is used, since *OpenMOC* was designed to automatically generate the required geometry input files for *UMG2*. This makes it very easy to quickly change the mesh if the blade design changes.

UMG2 can generate an unstructured, periodic, two-dimensional mesh around a given geometry. For this, the user must provide the blade geometry coordinates, specifications like blade pitch, the boundary conditions, and the cell size constraints at each boundary. A spline is then created through the given coordinates to define the blade geometry. Inflow, outflow, and periodic boundaries are also defined. Then, an unstructured mesh is generated, automatically ensuring that the nodes on both periodic boundaries align. Additionally, *UMG2* can generate wall refinement zones around specified surfaces, using a structured mesh, to accurately resolve surface viscous effects. The user can specify the first cell height and the height of the full refinement layer. In this case, a wall refinement zone is applied to the blade surface.

The first cell height and the height of the refinement zone are determined using an approximation

$$y^+ = \frac{y \cdot Re}{C \cdot Re^{1/14} \cdot \sqrt{80}}, \tag{3.5}$$

where y is the height, Re is the Reynolds number based on the cascade exit conditions, and C is the chord length. To determine the first cell height, $y^+ = 1$ is used to ensure that the surface viscous effects are accurately resolved. For the height of the refinement zone, $y^+ = 1000$ is commonly used. During post-processing of the results, y^+ is evaluated across all walls for each analysis to ensure that $y^+ \lesssim 1$.

The meshed domain can be seen in Figure 3.7 including the boundaries. In subsection 3.2.3, two blades were designed, based on one geometry but scaled based on the mass flow rate through the cascade. To obtain a mesh for the five- and seven-passage cascade blades, this mesh can simply be scaled down with the size ratio between the two blades since the geometry is the same. In this way, the mesh retains the exact same cell count, meaning that only one mesh convergence study is required for the infinite cascade meshes.

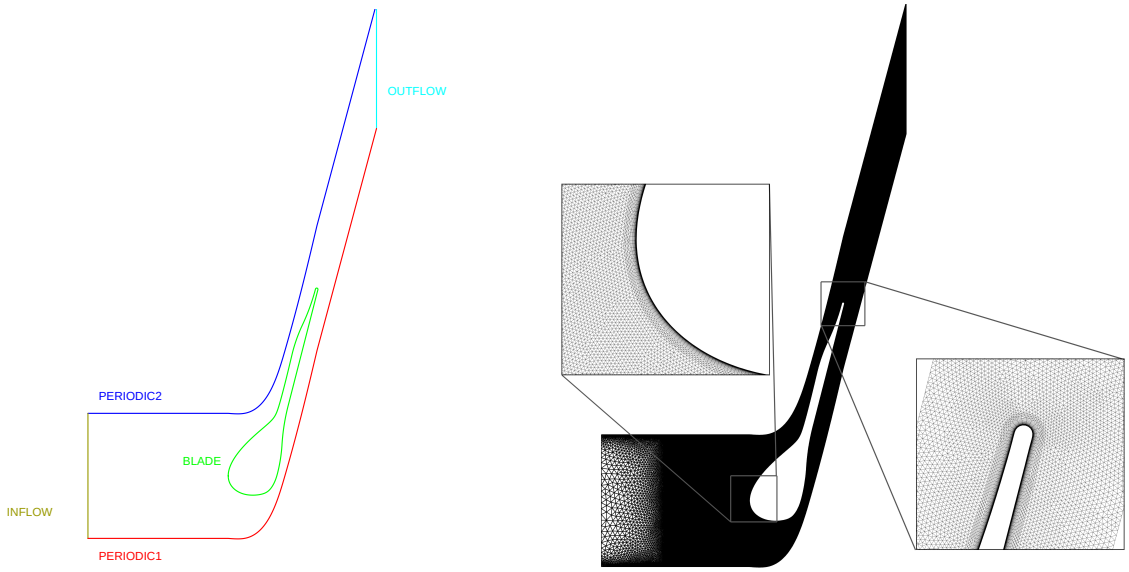

(a) Domain boundaries

(b) Meshed domain

Figure 3.7: Infinite cascade numerical domain

Next, both the five- and seven-passage cascade test section domains must be discretised. This domain introduces cascade side walls, instead of periodic boundaries. The side walls of the test section will be made up of straight walls at the inflow connected to the leading edge of one half of a blade, which is in line with the other blades to form the cascade passages. The half blades are followed by straight walls connected at the trailing edge, rotated by the tailboard angle ϕ_{tb} to direct the outflow. Initially, the tailboard angle is set to the design flow angle: $\phi_{\mathrm{tb}} = \phi_{\mathrm{a}} = 75°$. Then, these outflow walls (henceforth called tailboards) are rotated to redirect wall-reflected shock waves away from the measurement area. Figure 3.8 shows how one of the side walls is constructed. Note that the side wall for the opposite side of the cascade is constructed in a similar fassion using the other half of the blade geometry.

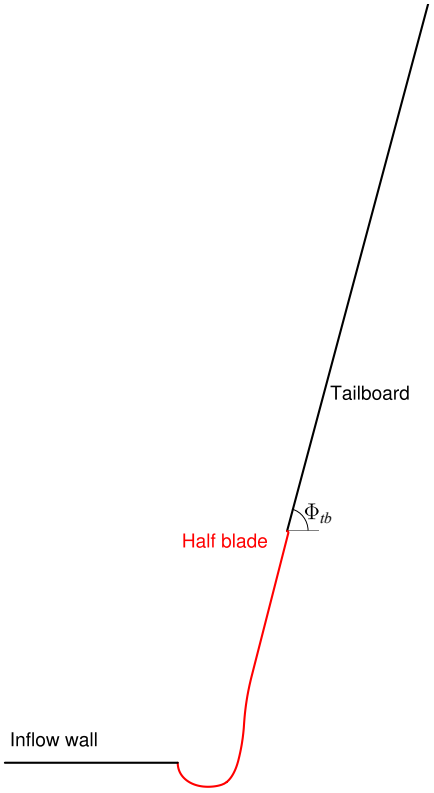

Figure 3.8: Diagram showing the construction of the cascade side wall

Since these domains contain more complicated geometries at the test section walls, *UMG2* can no longer be used if one wants to use wall mesh refinement. The suspected cause are the locations on the cascade walls where the straight in- and outflow walls connect to the half-blade geometries. As an example. Figure 3.9b shows the location at the trailing edge. Here, the walls form an angle of almost 90 degrees, possibly causing the wall refinement zones to overlap. For this reason, cascade test section meshes are generated using the commercial *Ansys ICEM* software. Using *ICEM*, the wall refinement layer can be generated manually using blocking, resulting in the mesh in Figure 3.9b. For these meshes, the same first cell height and refinement layer height are used as for the infinite cascade. Again, during post-processing, the y^+ values are analysed to ensure that $y^+ \lesssim 1$ along all walls.

To ensure that the flow periodicity between passages is unaffected by the mesh, the mesh inside each passage should be identical. This is achieved by meshing a single passage, as opposed to splitting two passages and meshing around one blade like the infinite cascade mesh. One passage is bound by the pressure-side blade half on the bottom and the suction-side blade half on top. Then, straight lines connect the inflow and outflow to these blade halves. The width of one passage is equal to the pitch. The mesh for the cascade is made by repeating the passage mesh offset by the pitch and merging the overlapping nodes at the coinciding boundaries. This requires the nodes on the coinciding boundaries to be perfectly aligned, resulting in the same cell spacing on these boundaries.

An issue with this approach arises because the pressure-side and suction-side walls indicated in Figure 3.10a both have wall refinement zones. If both of these are present in the passage mesh, repeating this mesh will cause a refinement zone behind the trailing edges of all blades in the cascade. This is undesirable for two reasons. First of all, this unnecessarily increases the number of cells and thus computational cost. More critically, this results in highly elongated cells that are not necessarily oriented in the direction of the flow, which could lead to convergence issues.

Finally, to mitigate reflected shocks, the bottom and/or top tailboards can simply be rotated while ensuring a constant location for the outflow boundary. This rotation will cause the tailboard(s) to increase or decrease in length. Rotation of the tailboard can also increase the length of the outflow boundary. To

ensure a constant cell size on the tailboards and the outflow boundary, the number of cells is increased or decreased on these boundaries with the ratio of this change in length.

To solve this issue, three separate passage meshes are made. One in which only the blade surfaces (suction-side and pressure-side) have a wall refinement zone, as shown in Figure 3.9a. This mesh can then be repeated to ensure mesh periodicity in these passages. Then, the first and last passages of the cascade (directly next to the test section walls) require separate meshes. One mesh will contain a wall refinement zone of the entire wall that includes the inflow wall, the half-blade, and the tailboard, as seen in Figure 3.9b. The other will have the same refinement zone, except it will be on the wall with the pressure side half of the blade geometry, called the pressure-side wall in Figure 3.10a. A five-passage cascade mesh is then made up of first the passage with the refined pressure-side wall, then three repeating meshes with only the blade surface refinement and finally a passage with the suction-side wall refinement. For the seven-passage cascade, the five-passage meshes can simply be scaled like the infinite cascade mesh and two additional repeating passage meshes can be added. The resulting mesh of the five-passage cascade test section can be seen in Figure 3.10b. The domain boundaries are shown in Figure 3.10a.

As a final step, a mesh convergence study is performed for both the infinite cascade and finite cascade meshes to determine the number of cell required for accurate results. Since both meshes can be scaled down to create the seven-passage cascade meshes, the mesh convergence study will be performed only on the five-passage cascade (blade scale) meshes. The mesh convergence study and its results are described in Appendix A. The selected mesh for the infinite cascade domain consists of 197,834 elements and the selected mesh for the five passage cascade domain consists of 558,857 elements.

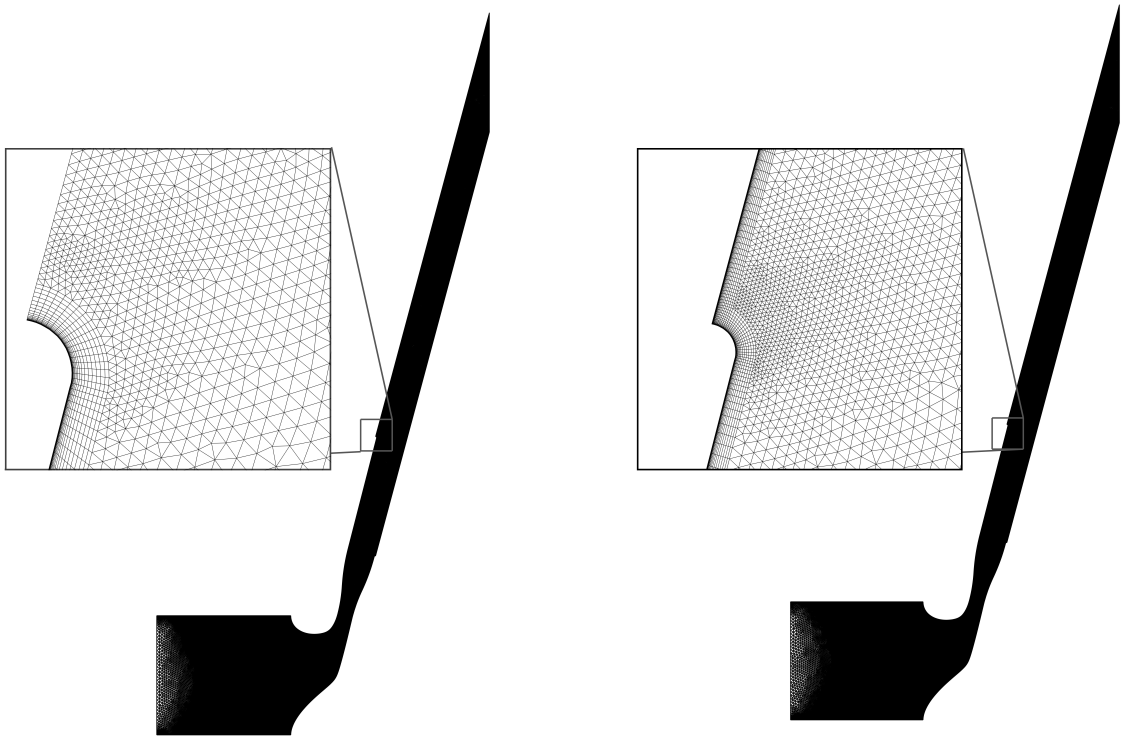

(a) Repeated mesh **(b)** Suction-side wall refinement mesh

Figure 3.9: Mesh zones which are merged to form the five passage cascade mesh

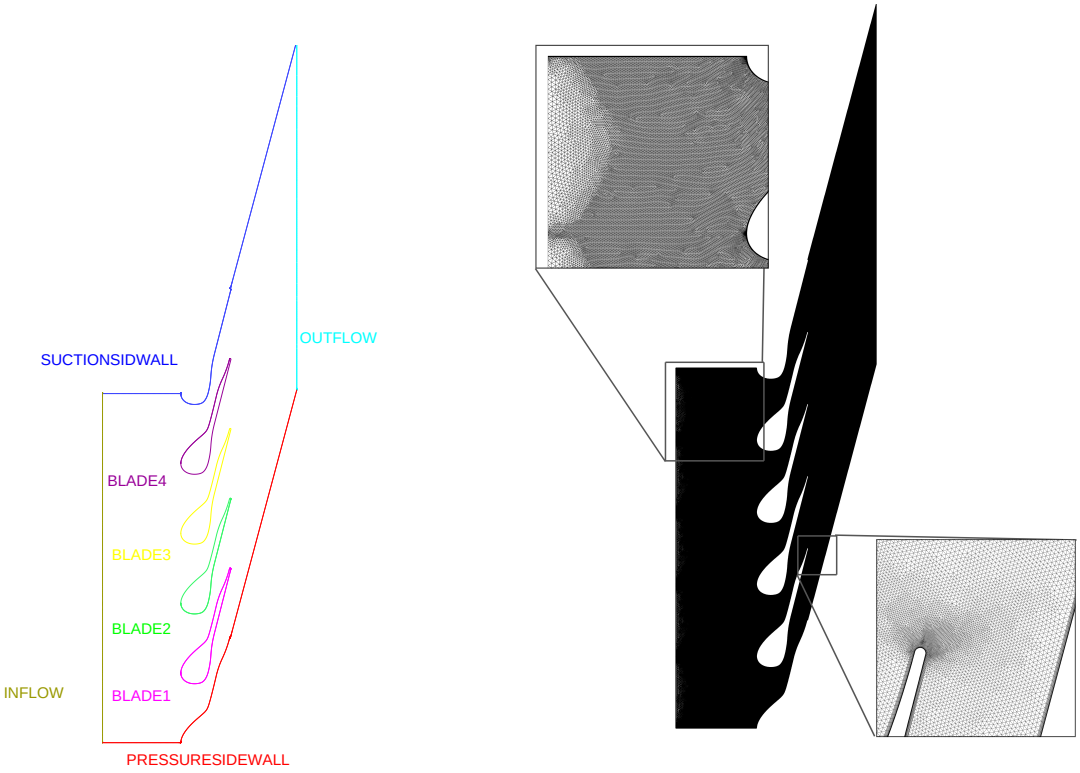

(a) Domain boundaries **(b)** Meshed domain

Figure 3.10: Five passage cascade numerical domain

3.3.2. Numerical Solver

Numerical analysis is performed using the open-source *SU2* software[82] to solve the Reynolds-averaged Navier-Stokes equations. *SU2* has integrated capabilities to handle NICFD computations, including the Peng-Robinson (PR) Cubic Equation of State (CEoS), as well as support for the external *CoolProp* library. The capabilities of *SU2* to accurately compute NICFD flows have been verified against both analytical solutions and a commercial software suite[83]. Furthermore, experimental results for NICFD flow through a planar nozzle test section show good agreement between numerical results and experimental data for both Mach number and pressure[54].

Thermodynamic state properties of the working fluid are computed using the built-in PR CEoS. However, a CEoS could prove insufficiently accurate for the nonmonotonic expansion, as the expansion line is close to the critical point of the working fluid, as discussed in section 2.3. For this reason, subsection 3.3.4 discusses a verification study of the PR EoS for the nonmonotonic expansion using the Helmholtz free energy MEoS (also called HEoS) implemented in *CoolProp*[84].

For the viscosity and turbulence models, constant molecular viscosity and Prandtl number are used, respectively. For both, the averages of the isentropic expansion lines for each experimental condition are used. For the turbulence model, the Spalart-Allmaras model is used. Each simulation is initialised using a first-order upwind Roe convective scheme with an outlet pressure ramp that gradually reduces the pressure until the design pressure ratio is reached. Then, the computation is restarted with a second-order central JST scheme starting with the first-order result file. For compressible flows, the only available turbulence convergence scheme is first-order scalar-upwind. The time-discretisation schemes for both the flow and turbulence models are Eurler-implicit.

Finally, the boundary conditions must be considered. For the walls (blades, suction- and pressure-side walls), non-slip adiabatic wall boundary conditions are used. For the in- and outflow boundaries, non-reflective boundary conditions (NRBCs) must be used to avoid non-physical shock reflections on the outlet boundary. The NRBC implemented in *SU2* is the Giles boundary condition[85]. At the inflow boundary, the total pressure and temperature are imposed. At the outlet, static pressure is imposed.

For the conditions imposed on the in- and outlet, the values of the isentropic expansion lines selected in subsection 3.1.2 are used. Finally, for the infinite cascade domain, a periodic boundary condition is imposed on both periodic boundaries indicated in Figure 3.7a, cancelling out all fluxes between the two.

SU2 requires additional settings, in addition to those discussed in this section. All settings can be found in the example configuration files for both the first-order initialisation and the second-order computation in Appendix B.

3.3.3. Post-Processing

Some post-processing steps are already integrated in *SU2*, like calculating average flow properties in the in- and outflow boundaries or determining the total-to-static pressure ratio. For more detailed analysis, additional post-processing steps are developed.

The post-processing steps are performed using a Python script and the commercial *Tecplot360* integrated post-processing environment. Contour plots of flow Mach number, pressure and density are made using *Tecplot360*. Furthermore, the density gradient can be quickly calculated across the domain, with which numerical Schlieren images are generated. A Python script is used to generate graphs containing blade surface data or line data along the cascade at a specified distance behind the cascade trailing edges, parallel to the in- and outflow boundaries. To extract the line data, a *Tecplot360* interface for Python is used called *Pytecplot*. Finally, a script is used to command *Tecplot360* to extract line data along a series of evenly spaced lines across the cascade, again parallel to the in- and outflow boundaries. A macro is then executed to calculate the mass-flow averaged entropy of every line. This can then be used to plot the evolution of the entropy along the flow path of the test section.

3.3.4. Verification of Equation of State

To verify the accuracy of the Peng-Robinson CEoS for the nonmonotonic expansion, two CFD calculations are performed using the infinite cascade numerical domain (5 passage blade scale) together with the nonmonotonic expansion conditions. One will use the Peng-Robinison EoS, while the other uses the Helmholtz-energy Equation of State (HEoS) implemented in *CoolProp*. All other solver settings are identical between the two cases.

The average flow properties at the in- and outflow boundaries are summarised in Table 3.7, including the results of the nonmonotonic isentropic expansion line. In addition, information about the computational cost of each case is included. Note that computations for both cases were performed on 40 cores using the same CPUs. From the results it becomes clear that the different Equations of State have minimal impact on the average flow properties. However, as expected, the average time per iteration for the HEoS is one order of magnitude greater than that of the CEoS. Additionally, the solution requires many more iterations to converge to the same residual criterion. Because of these effects, the computational time for the HEoS is very high compared to the CEoS, which means that it is unfeasible to use the HEoS for the larger meshes of the complete cascade test sections. A solution to this problem could be the use of a look-up table, as discussed in section 2.3. However, this functionality has not yet been implemented in the version of *SU2* used during this research.

Furthermore, Figure 3.11 shows graphs comparing blade loading and line distributions at one chord length behind the cascade. The blade loading and blade temperature are plotted against the distance in the x-direction (the direction of the inlet flow), normalised such that zero is the leading edge and one is the trailing edge location. Line distributions are plotted against the y-distance, normalised with respect to pitch. From the results, it becomes clear that the EoS has no significant effect on both the blade loading and the flow angle. Also, the effect on the flow Mach number is minimal, though more significant. Finally, the most significant difference is found for the flow temperature, especially behind the throats of the cascade passages.

For this research, the accuracy of both the blade loading and shock wave locations is critical. The results show that both flow features are accurately predicted by the PR EoS. For this reason, and to avoid excessive computational costs, the Peng-Robinson EoS is used for all subsequent analyses.

Table 3.7: Average in- and outflow properties and computational cost for the Peng-Robinson CEoS and HEoS (nonmonotonic expansion conditions)

		Expansion line	PR CEoS	CoolProp HEoS
Outflow Mach number	M_{outlet} [−]	1.827	1.790	1.787
Cascade mass flow rate	$\dot{m}$ [kg/s]	0.951	0.946[1]	0.948[1]
Inlet pressure	P_{inlet} [bar]	21.33	21.30	21.30
Outlet pressure	P_{outlet} [bar]	3.282	3.282	3.281
Total-to-static pressure ratio	β_{ts} [−]	6.500	6.501	6.501
Computational cost (excl. first-order initialisation)				
Average time per iteration [s]		-	0.195	1.90
Total computational time [h]		-	0.25	6.0
Number of iterations		-	4 576	11 172

[1] Calculation: $\dot{m} = \dot{m}_{2D} \cdot h_{bl} \cdot n_{pass}$

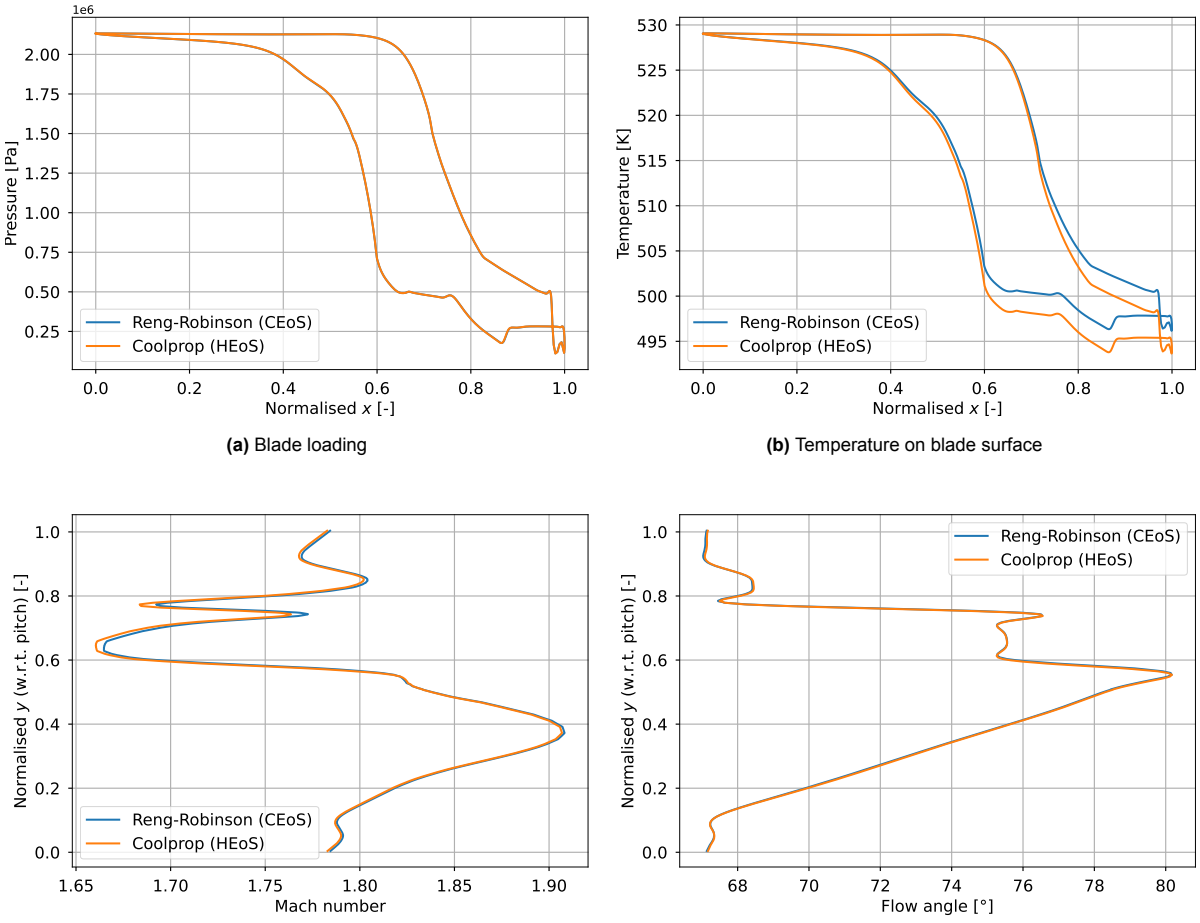

(a) Blade loading

(b) Temperature on blade surface

(c) Mach number distribution one chord length behind the cascade (in flow direction)

(d) Flow angle distribution one chord length behind the cascade (in flow direction)

Figure 3.11: Comparison between CEoS and HEoS results for nonmonotonic expansion condition using the infinite cascade numerical domain

3.3.5. Verification of 2D Midplane Flow

The linear cascade test section must have 2D flow in the midplane, which is free from boundary layer effects originating from the endwalls enclosing the top and bottom of the cascade. This section will analyse a three-dimensional simulation of the five-passage cascade to verify that this is the case for the cascade height determined in subsection 3.2.3, using the nonideal expansion conditions. Additionally, the flow field in the midplane of the three-dimensional simulation is compared to the flow in a two-dimensional simulation. From this comparison, to determine if 2D simulations can accurately predict the midplane flow field of the cascade.

To create the 3D mesh, the five-passage cascade mesh generated in subsection 3.3.1 is extruded to half the blade height, creating one-half of the cascade. A symmetry boundary condition is then imposed on the midplane surface, allowing analysis of a full cascade using only half of the cells. Cell layers are added in the extrusion direction, where the first cell height is determined using Equation 3.5 with a y^+ of one to resolve the viscous effects on the bottom wall. For the following cell layers, the cell height increases by roughly a factor of 1.3. Again, y^+ on the bottom test section wall is investigated during post-processing to ensure $y^+ \lesssim 1$.

Again, a non-slip adiabatic wall boundary condition is imposed on the bottom wall of the cascade. Due to the current implementation approach of the Giles boundary condition in *SU2*, it can only be applied in a three-dimensional domain when periodic boundary conditions are used on the walls connecting the inflow and outflow boundaries. Because of this, it is not possible to use an NRBC for the three-dimensional analysis. To ensure a fair comparison, the Giles boundary condition is also replaced in the two-dimensional simulation.

The flow fields are analysed in a similar way as was done for the CEoS verification, where Table 3.8 shows the average flow properties and Figure 3.12 shows the blade surface and line distribution data. In Table 3.8, the ”3D” averages are taken across the full in- and outflow boundary surfaces, while the ”3D midplane” averages are taken across the lines where the cascade midplane surface (with the symmetry boundary condition) intersects with the in- and outflow boundaries. As expected, the results in Table 3.8 show a reduction in mass flow rate, and thus exit Mach number in the 3D simulation compared to the 2D results, caused by the viscous effects on the top and bottom walls. However, the average exit Mach number is much closer when only looking at the midplane of the 3D simulation, only deviating 0.5%.

In Figure 3.12, data is plotted at different heights above the bottom wall in the 3D cascade simulation, where 50% span is in the midplane. In addition, the data from the 2D is plotted. The line distributions are again located one chord length behind the cascade in flow direction and the normalisation of x- and y-distance are the same as in Figure 3.11. The results indicate that there is no significant difference between the flow in the 45% and 50% spans, suggesting that the flow in the midplane is indeed two-dimensional. This confirms that the blade height is large enough.

When comparing the midplane 3D and 2D distributions, the differences in the flow fields are much more significant. The blade loading and blade temperature graphs indicate that the shock impingement location on the suctions side blade surface is shifted further downstream in the 2D simulation. To investigate this effect in more detail, Figure 3.13 depicts the numerical Schlieren images of the 2D and 3D midplane flow fields. From these images, it becomes clear that the shocks reflecting from the bottom tailboard are angled slightly further in the flow direction for the 2D cascade. This is what causes the change in the location of the pressure drop on the suction side of the blade. To investigate whether only the reflected shocks are altered or if the source of the deviation originates from the shocks at the trailing edge, Figure 3.13a plots the pressure distribution along the bottom tailboard. The locations of the pressure minima indicate the shock locations. The graph shows that the pressure distribution already deviates at the start of the tailboard. The first shock reflection is already slightly different, with the difference in distance increasing when shocks are reflected off a blade and travel a further distance before reaching the bottom tailboard.

A possible explanation for the difference in the shock structure could be the difference in the average Mach number at the outlet, since this drives the angle of the trailing edge shocks. A larger exit Mach number causes the shocks to turn further downstream. However, the 3D midplane outlet Mach number is slightly higher than in the 2D case. This would suggest that the 3D midplane shock reflections should be further downstream for the 3D case. However, the data suggest the opposite. Additionally, from the

blade loading, it seems that the impingement location of the trailing edge shock from the blade below is exactly the same for both cases. This suggests that the deviation is not caused by a change in trailing edge shock angle.

Figure 3.13 shows that the shock waves in the 3D midplane have a darker colour in the Schlieren visualisation. Since the same colour scale is used in both images, this indicates that these shock waves have a higher intensity. This could also affect the shock reflection and thus the reflected shock locations. A possible cause for the intensity change could be the slightly different pressure ratio and slightly higher outflow Mach number in the middle plane of the 3D simulation, as listed in Table 3.8.

Currently, the exact cause for these results remains uncertain. Mainly the shocks reflected from the bottom tailboard seem affected, which must in any case be mitigated for the cascade to operate under infinite cascade conditions. Another important consideration is the fact that three-dimensional simulation is much more computationally expensive. For these reasons, the final analysis is performed using two-dimensional domains.

Table 3.8: Average in- and outflow properties for the 2D and 3D five passage cascade analysis (nonideal expansion conditions)

		Expansion line	**2D**	**3D midplane**	**3D**
Outflow Mach number	M_{outlet} [$-$]	1.829	1.774	1.783	1.678
Cascade mass flow rate	$\dot{m}$ [$\mathrm{kg/s}$]	0.667	0.666[1]	0.709[1]	0.627[2]
Inlet pressure	P_{inlet} [bar]	15.55	15.53	15.53	15.53
Outlet pressure	P_{outlet} [bar]	2.593	2.569	2.587	2.576
Total-to-static pressure ratio	β_{ts} [$-$]	6.000	6.056	6.014	6.040

[1] Calculation: $\dot{m} = \dot{m}_{\mathrm{2D}} \cdot h_{\mathrm{bl}}$
[2] Calculation: $\dot{m} = 2 \cdot \dot{m}_{\mathrm{3D}}$

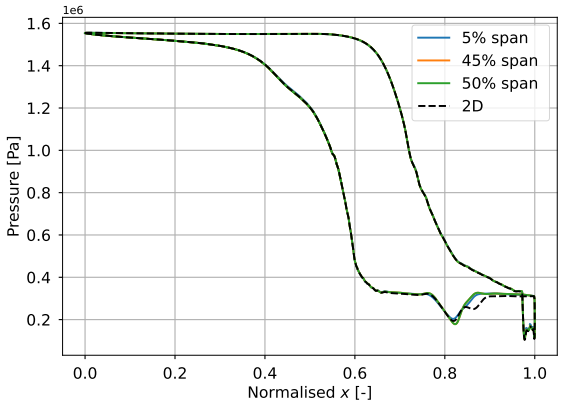

(a) Blade loading

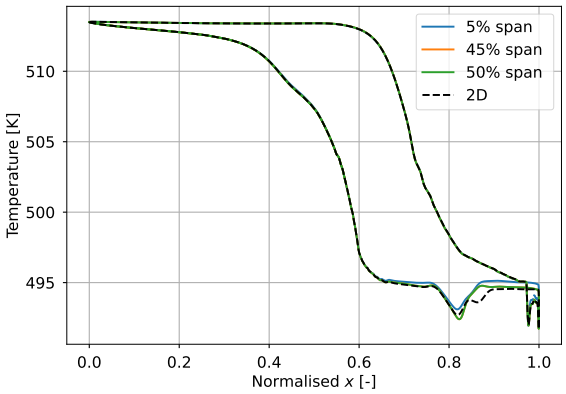

(b) Temperature on blade surface

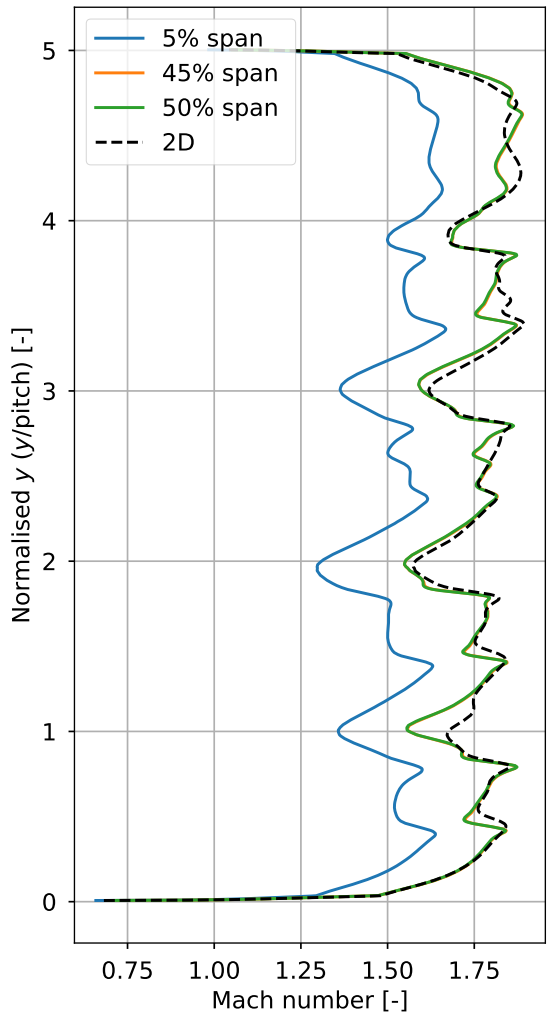

(c) Mach number distribution one chord length behind the cascade (in flow direction)

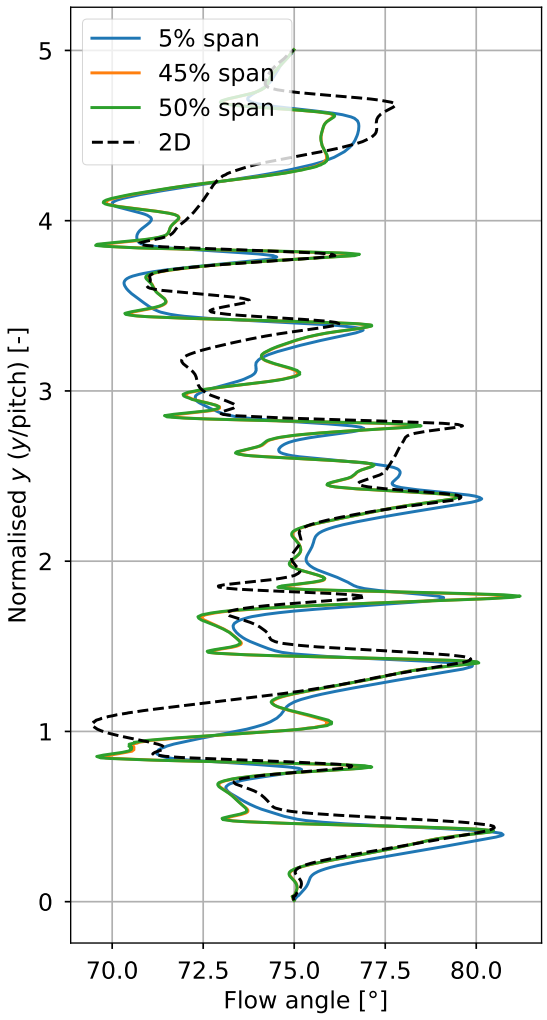

(d) Flow angle distribution one chord length behind the cascade (in flow direction)

Figure 3.12: Comparison between 2D and 3D results for nonideal expansion condition for the five passage cascade test section, with both simulations using Riemann boundary conditions

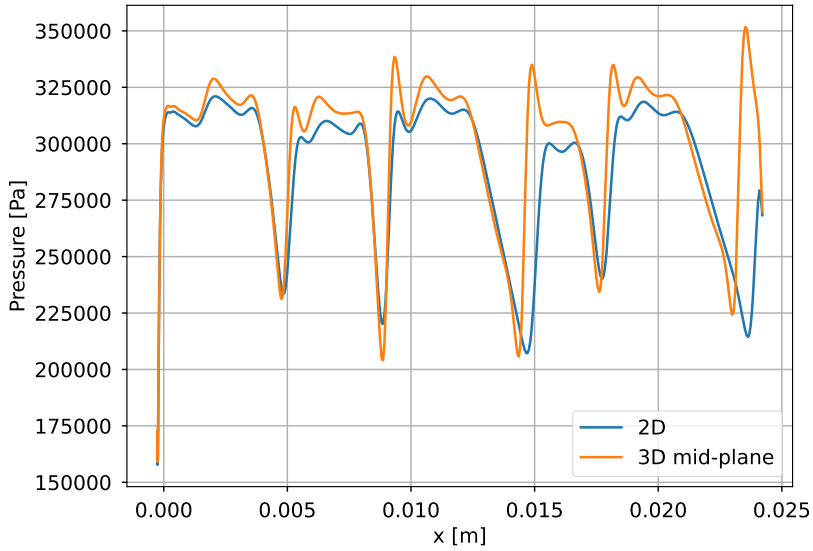

(a) Pressure distribution along bottom tailboard

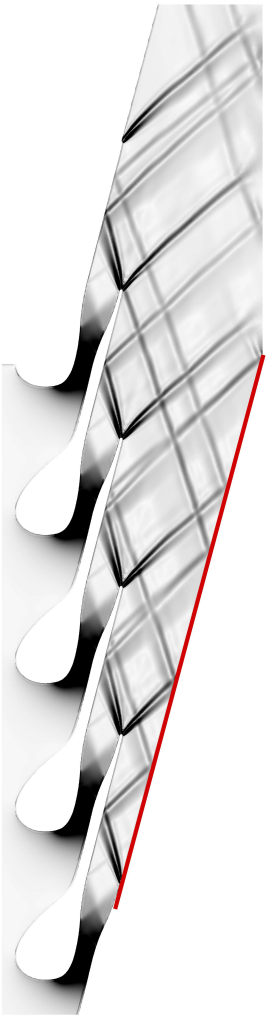

(b) Numerical Schlieren visualisation of the 2D analysis

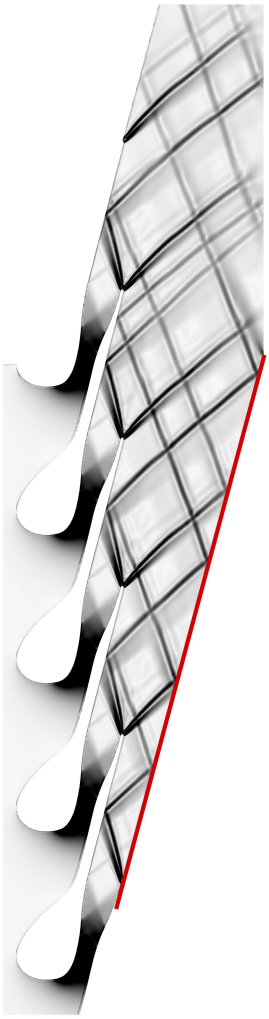

(c) Numerical Schlieren visualisation of midplane flow of the 3D analysis

Figure 3.13: Comparison between 2D and 3D midplane flow shock structures, using the same colour scale

4

Results

Based on the methodology discussed in the previous chapter, a range of numerical analyses are performed for different test section geometries and expansion conditions. In this chapter, the resulting flow fields are analysed and compared to find the optimal test section geometry. To investigate the effects of the nonideality of the working fluid, section 4.1 compares the flow fields resulting from the infinite cascade numerical domain analyses for the three expansion conditions. Next, section 4.2 compares the five- and seven-passage cascades to investigate whether increasing the number of passages improves the flow through the centre passage of the cascade compared to infinite cascade results. Based on the results, the number of passages to use for the test section cascade is decided. Then, section 4.3 investigates the effect of the tailboard angle on the flow field of the test section, ultimately aiming to determine the best tailboard orientation for the test section. Finally, section 4.4 provides an overview of the proposed design of the linear cascade test section.

4.1. Effects of Thermodynamic Conditions on Infinite Cascade Flows

Before evaluating the flow inside the linear cascade test section, the results of the two-dimensional infinite cascade numerical analysis are compared for the three expansion conditions. This comparison can provide first insights into the effects of flow ideality on stator performance.

A summary of the average flow properties at the inflow and outflow boundaries of the domain is shown in Table 4.1. Here, for each expansion condition, the results of the CFD analysis are also compared with the results of the isentropic expansion line calculations of section 3.1. The results show that both the total input pressure and the static outlet pressure match closely the desired values based on the expansion line calculations. Thus, it can be concluded that the CFD calculations have properly converged to the desired expansion conditions. Additionally, the results show a reduction in both the mass flow rate and the outflow Mach number compared to the isentropic expansion line calculations, as a result of viscous losses.

In addition to the average in- and outflow properties, Table 4.1 also shows the efficiency of the stator profile in each expansion condition using the definition

$$\eta_{\mathrm{N}} = \frac{h_{\mathrm{t,inlet}} - h_{\mathrm{exit}}}{h_{\mathrm{t,inlet}} - h_{\mathrm{s,exit}}}, \tag{4.1}$$

where $h_{\mathrm{t,inlet}}$ is the total enthalpy based on the total inlet conditions, h_{exit} is the enthalpy directly behind the stator vane and $h_{\mathrm{s,exit}}$ is the isentropic enthalpy behind the stator[78]. The enthalpy behind the stator vane is determined by taking a mass flow average of the pressure and temperature along a line distribution in y-direction behind the stator vane and determining the corresponding enthalpy using the Coolprop fluid model. Similarly, the total inlet enthalpy is determined using the total pressure and temperature at the inlet. To determine the isentropic enthalpy, first the total inlet entropy is determined with the Coolprop fluid model using the total inelt conditions. This entropy is then used together with the average pressure behind the stator to calculate the isentropic enthalpy behind the stator.

The results indicate a significant drop in profile efficiency when comparing the nonideal condition to the ideal condition. The effiency drop between the nonmonotonic condition and the nonideal condition is smaller. This is expected since these conditions are closer together in the Ts-diagram. Clealy, nonideal thermodynamic effects have a significant negative impact on profile efficiency. Considering that the stator profile design is optimised for the nonmonotonic condition, one would expect that this effect is even greater when comparing stator geometries that are optimised for each individual condition. Further research should investigate whether there is a significant improvement in profile efficiency for the ideal and nonideal conditions when using stator geometries optimised for these conditions.

Table 4.1: Average inflow and outflow properties of the 2D infinite cascade numerical analysis for the three expansion conditions compared to the isentropic expansion line results, including profile efficiencies

		ideal		**nonideal**		**nonmonotonic**	
		expansion line	**CFD**	**expanion line**	**CFD**	**expansion line**	**CFD**
Outflow Mach number	M_{outlet} [–]	1.827	1.774	1.829	1.783	1.827	1.790
Outflow angle	α_{outlet} [°]	–	76.15	–	73.88	–	70.87
Mass flow rate	$\dot{m}$ [kg/s]	0.307	0.306	0.667	0.664	0.951	0.946
Inlet total pressure	$P_{\mathrm{t,inlet}}$ [bar]	7.725	7.725	15.56	15.56	21.33	21.33
Inlet static pressure	P_{inlet} [bar]	7.725	7.705	15.56	15.53	21.33	21.30
Outlet static pressure	P_{outlet} [bar]	1.405	1.405	2.593	2.593	3.282	3.282
Total-to-static pressure ratio	β_{ts} [–]	5.500	5.498	6.000	5.999	6.500	6.501
Profile efficiency	η_{N} [%]	–	92.2	–	84.1	–	81.4

Table 4.1 also indicates a significant reduction in the average flow angle with increasing nonideality. To investigate this flow angle effect in more detail, Figure 4.1 shows a Mach number contour and a numerical Schlieren visualisation of the two-dimensional infinite cascade domain for the three expansion conditions. The results of each expansion condition are stacked to form a three-bladed cascade, where the domain around each blade contains the results of one of the expansions. To better distinguish the three expansions, each uses a different colour scale in the Schlieren visualisation. Using this layout, changes in the flow field can most easily be identified in the boundaries running through the centre of the passages. Finally, streamlines have been added to the Schlieren image to visualise the flow direction along the trailing edge wake.

In addition, Figure 4.2b plots the flow angle against the normalised pitch along the line distribution drawn in Figure 4.1 (the dashed line). This graph confirms a significant change in the flow angle between the different expansions, especially in the flow centred between the blades.

In the figures, a clear change in the flow angle can be seen between the different conditions. The flow immediately behind the trailing edge of the ideal expansion blade aligns well with the metal angle. However, for the nonideal expansion, the flow is bent downward. Finally, the flow is bent even more in the nonmonotonic condition. When closely examining the trailing edge shock structures behind the blades in the Schlieren visualisation, it becomes clear that these are also affected. Due to nonideal thermodynamic effects, the bottom expansion fan is compressed, while the top expansion fan becomes wider. This reduces the flow angle behind the cascade with increasing nonideality, which can be seen in Figure 4.1. The expansion fan angles change since the Prandtl-Meyer function predicts that the flow turing through an expansion fan is based on the heat capacity ratio of the fluid for a given Mach number, which is a thermodynamic condition affected by the flow properties. This means that because of the change in thermodynamic conditions between the three different expansions, the expansion fan angles change. This then affects the flow angle behind the cascade.

This change in flow angle has a significant effect on the blade loading, plotted in Figure 4.2a. The shock reflection location on the suction-side of the blade is clearly moving towards the trailing edge with decreasing flow ideality. A possible cause for the flow angle reduction could be that the stator vanes can no longer fully deflect the flow because of the increased density associated with the increase in nonideality.

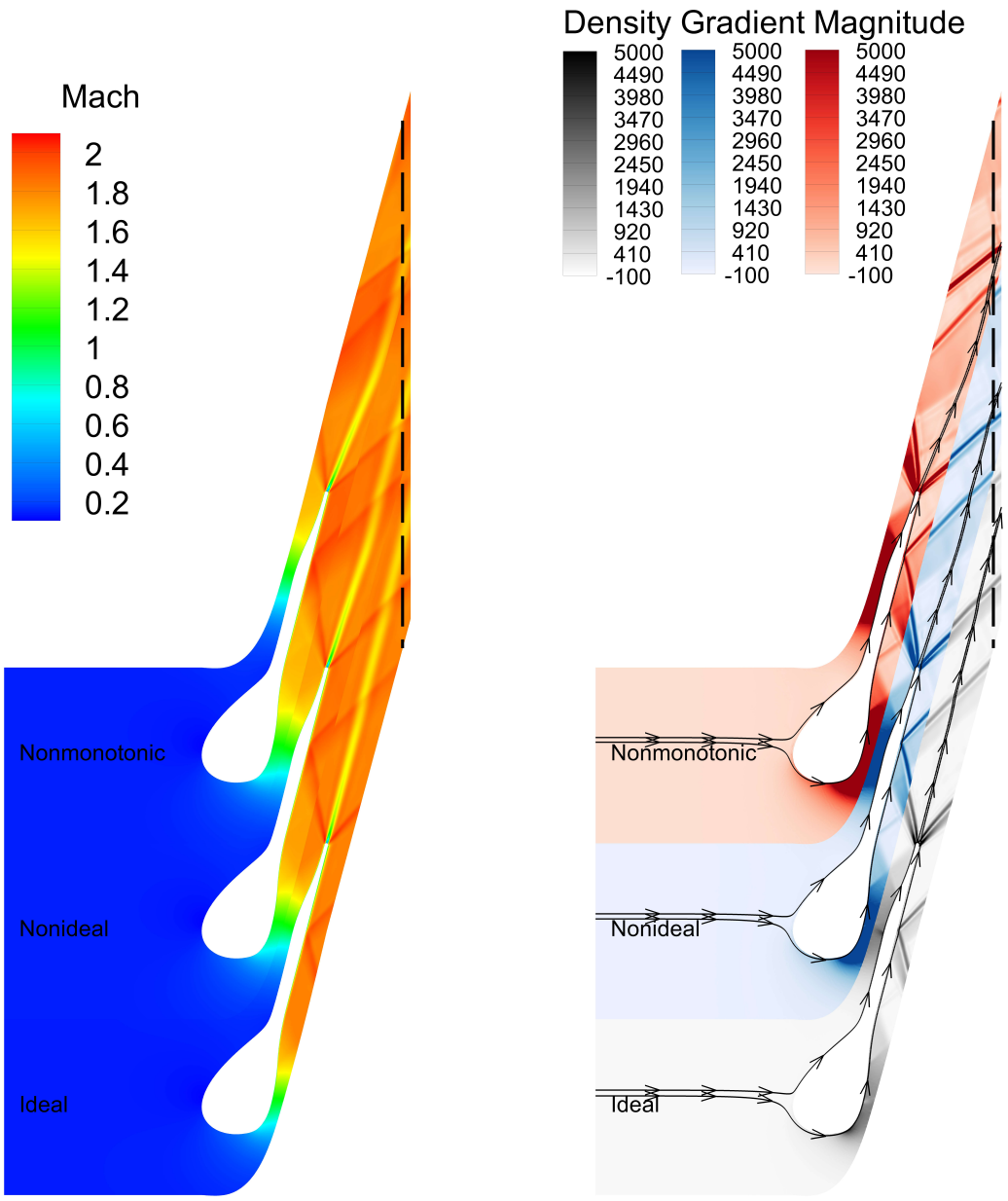

(a) Flow Mach number

(b) Numerical Schlieren visualisation including streamlines

Figure 4.1: Comparison between the contour plots of the flow around a single blade in an infinite cascade for the three expansion conditions, with the dashed line indicating the location of the line distribution

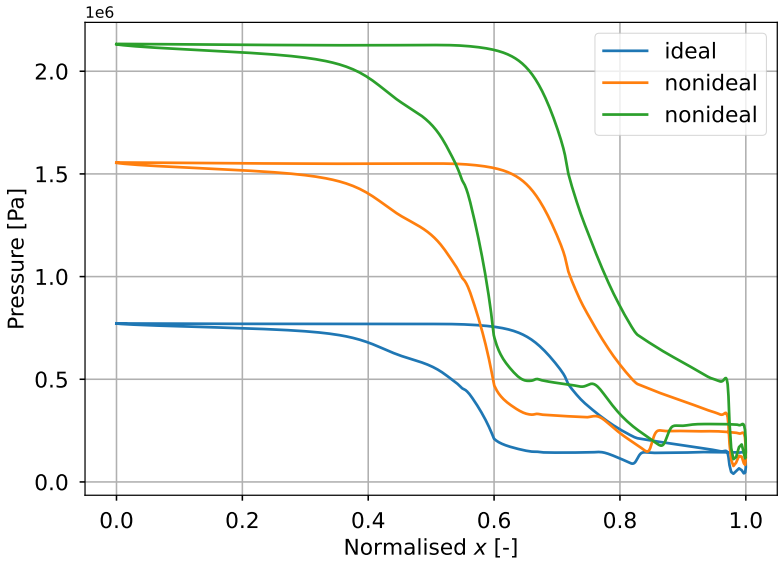

(a) Blade loading

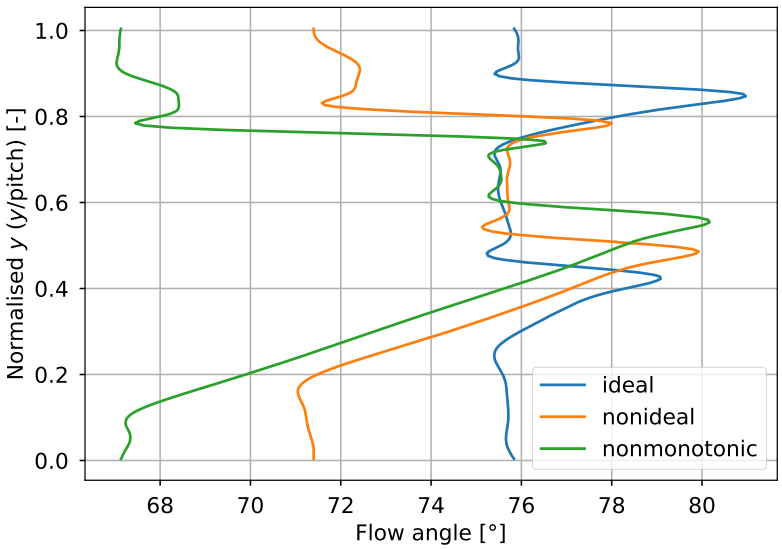

(b) Flow angle distribution one chord length behind the cascade (in flow direction)

Figure 4.2: Comparison of the 2D infinite cascade numerical analyses for the three expansion conditions

4.2. Effect of Additional Cascade Passages

This section shows a comparison between the five- and seven-passage cascade test sections to determine whether adding additional passages improves the flow through the centre passage with respect to the infinite cascade results. For this purpose, the blade loading in the centre cascade passage is compared to the infinite cascade blade loading. To obtain the centre passage blade loading, the pressure distributions of the pressure-side of blade two and the suction-side of blade three for the five-passage cascade and blade three and four respectively for the seven-passage cascade are extracted (where the blades are numbered from bottom to top as indicated in Figure 3.10a). The resulting graphs comparing the blade pressure distributions of the centre passages of the five- and seven-passage cascades with the infinite cascade are shown in Figure 4.3. Here, the pressure is plotted against the x-distance, normalised with the axial chord length starting from the blade leading edge.

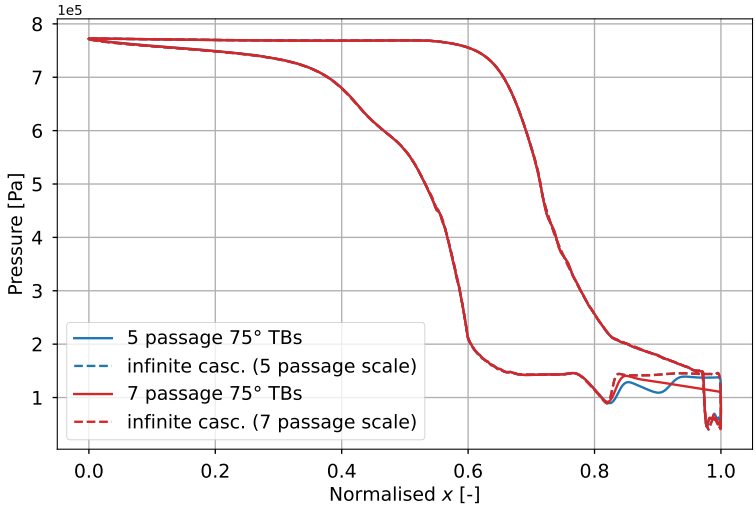

(a) Ideal expansion

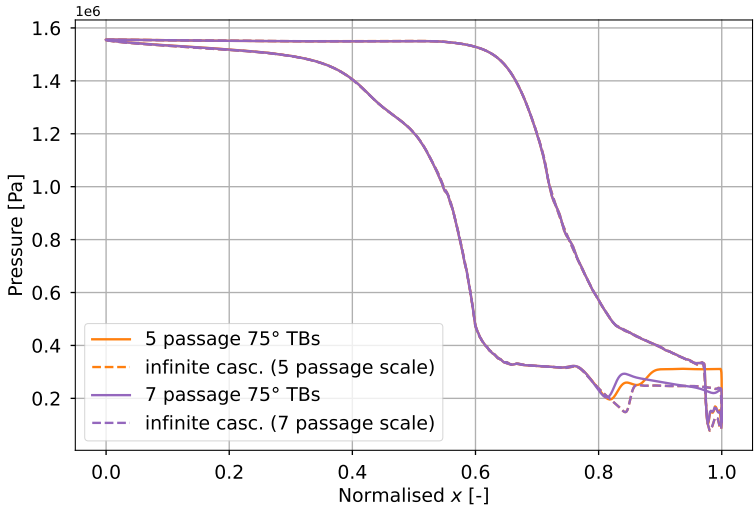

(b) Nonideal expansion

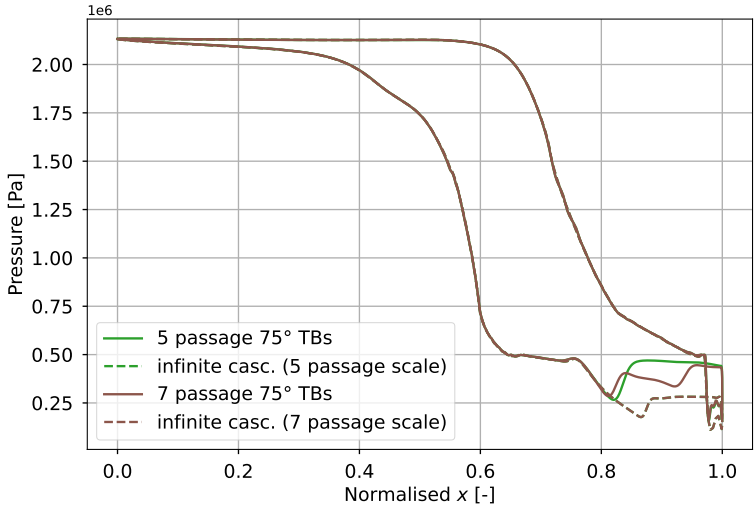

(c) Nonmonotonic expansion

Figure 4.3: Blade loading comparison between a five passage cascade, seven passage cascade and infinite cascades (five and seven passage cascade blade scales) for the three expansion conditions

First, note that the blade loading curves of the five- and seven-passage blade scale infinite cascades coincide perfectly. This shows that the difference in Reynolds number between the two blade scales, resulting from a difference in chord length due to the blade scaling based on the maximum allowable mass flow rate (see subsection 3.2.3), has a negligible effect on the blade loading. Furthermore, the blade loading of the five- and seven-passage cascades matches the infinite cascade well for all conditions, except for the region behind the shock reflection on the suction-side of the blade. This is caused by a combination of factors.

First, for all blade loading curves except for the ideal five-passage cascade simulation, a shock reflected from the bottom tailboard impinges on the suction-side surface in the centre cascade. In some cases, like, for example, the five-pass cascade curve in Figure 4.3a, the second shock impingement can clearly be seen as a second pressure drop. However, in other cases, such as in the five-passage cascade curve in Figure 4.3c, the reflected shock impinges at the same location as the trailing edge shock. In this case, the curve shows only one pressure drop, which is larger than the one in the infinite cascade. To clearly show the shock structure for both the five- and seven-passage cascades, numerical Schlieren visualisations of the nonmonotonic condition are shown in Figure 4.4. Here, the infinite cascade passage results are overlaid on the blade below the centre passage, using a red colour scale.

Of the six cases, only one is not affected by a wall-reflected shock wave, which is the ideal expansion in the seven-passage cascade test section. Even without reflected shock disturbance, the blade loading of this case deviates from the infinite cascade blade loading close to the trailing edge on the blade suction-side. This indicates that there is a second factor that influences the flow in the centre passage.

When comparing the three conditions, it becomes clear that the pressure behind the trailing edge shock impingement deviates more from the infinite cascade with increasing nonideality. Similarly, the location of the shock impingement is offset more from the location in infinite cascade curves when nonideality increases. The change in the direction of the trailing edge shocks can also be clearly seen in Figure 4.4.

The analysis in section 4.1 shows that the flow angle behind the infinite cascade decreases with increasing nonideality. Considering that for all expansions, the tailboard angle is set to the design flow angle of 75°, this means that the tailboards of the nonideal and nonmonotonic conditions are increasingly misaligned with the actual flow angle seen in the infinite cascade flow fields. The results in Figure 4.2b show that for the ideal condition, the tailboard angle should be slightly increased, which explains why the finite cascade distributions are below the infinite cascade distribution. For the other conditions, the deviation between the flow angle and tailboard angle is larger, resulting in a larger difference between the blade loading curves. Furthermore, in these conditions, the tailboard angle is larger than the flow angle in the infinite cascade, resulting in higher pressures on the suction-side of the finite cascade blades compared to the infinite cascade.

The results show that the blade loading for both the five- and seven-passage cascade test sections match the infinite cascade well, except at the end of the suction-side blade surface. Additionally, the seven-passage cascade does not seem to have significantly better blade loading in this region compared to the five-passage cascade. Based on these results, it can be concluded that five passages are enough to produce centre passage flow that is not affected by wall effects except for the wall-reflected shocks. The larger blade scale of the five-passage cascade will allow for better measurement resolution when using optical techniques. For this reason, the five-passage cascade is chosen for the remainder of the analysis.

Furthermore, the analysis shows that centre passage blade loading is significantly affected when the tailboards are not aligned with the flow angle of the infinite cascade results. Since correct blade loading is critical for investigating stator performance, the next section investigates the effect of the tailboard angle in more detail.

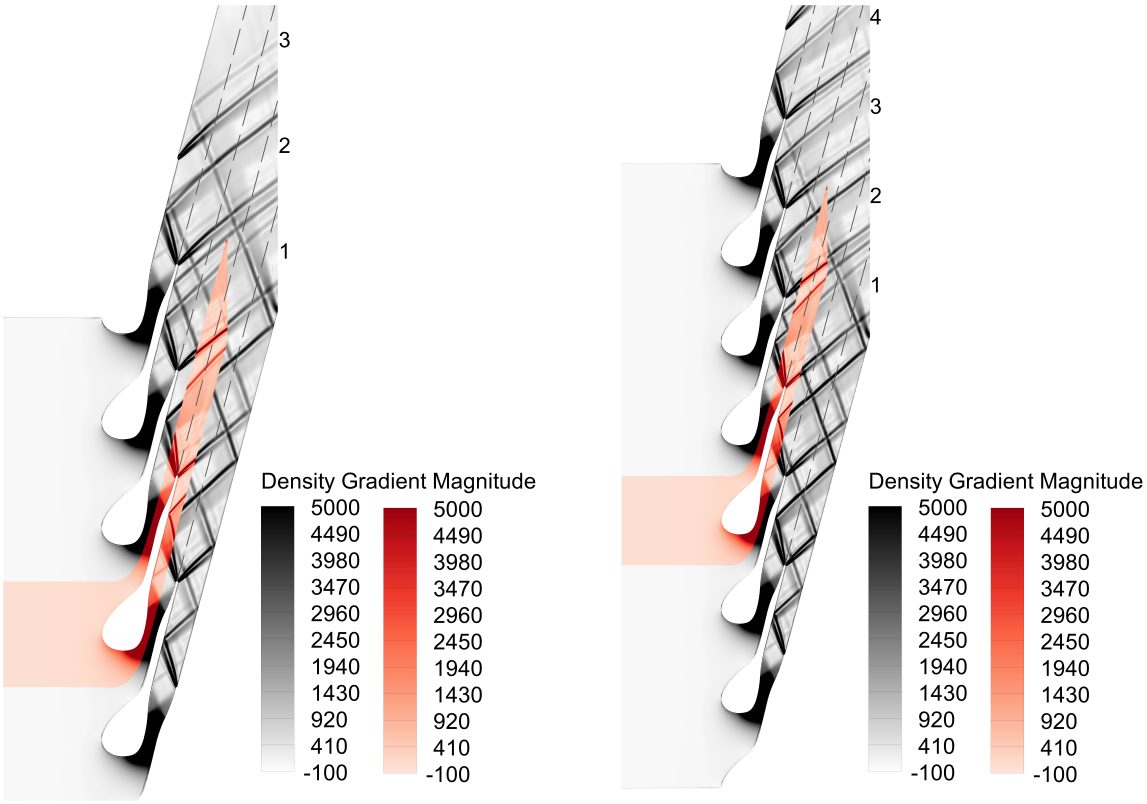

(a) Five passage cascade

(b) Seven passage cascade

Figure 4.4: Schlieren visualisations of the five and seven passage cascades with nonmonotonic expansion conditions compared to the infinite cascade flow field, including passage indicators

4.3. Effect of Tailboard Angle on Test Section Flow

With the number of passages to be used for the cascade test section selected, the angles of the cascade tailboards are the final remaining design consideration. The previous analyses show that, when the tailboards are aligned with the design flow angle, trailing edge shocks reflect off the bottom tailboard, back towards the cascade. Depending on the condition, one of these shocks impinges on the blade suction-side in the centre passage (as well as most other passages as shown in Figure 4.4), which is the intended measurement passage. This alters the blade loading, making it impossible to evaluate the stator performance as would be in an annular cascade. A solution to this could be to reduce the angle of either the bottom tailboard or both tailboards, so that the shock waves are reflected away from the cascade and more towards the outlet of the test section. In this section, the effect of different tailboard configurations on the test section flow field is investigated. For the analysis, only the nonmonotonic expansion condition is considered. First, flow fields with different tailboard angles are compared, where both tailboards are parallel. Then, the effect of the top tailboard will be analysed by keeping the bottom tailboard at a constant angle.

4.3.1. Parallel Tailboards

To investigate the effect of tailboard angle when both tailboards are parallel, four cascade test sections with different tailboard angles are compared to infinite cascade flow. For the first test section, the tailboard angle is equal to the blade design flow angle of 75°, like the one used in the analyses of the previous sections. A second test section design is used where the tailboards are angled to the average outlet flow angle determined in Table 4.1 (71°). Then for the third case, the tailboard angle is set at 68°, which is roughly equal to the outlet flow angle at the edges of the infinite passage domain, as shown in Figure 4.2b. Finally, the tailboards are angled such that the flow in the centre passage is free from shocks until one chord length downstream of the cascade, since this is the location of the line distribution in the infinite cascade domain. To verify that this is the case, a numerical Schlieren visualisation of the flow field in the 62° tailboard cascade is shown in Figure 4.6d, where the red line indicates the centre passage one chord length downstream of the cascade. In addition to this case, the Schlieren images for the other three cases are also shown in Figure 4.6.

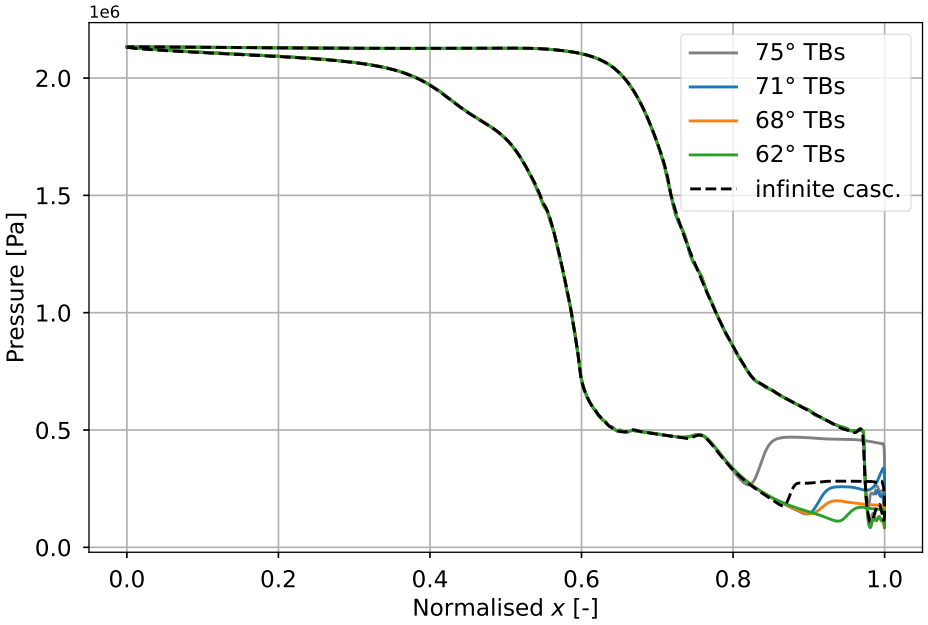

(a) Blade loading

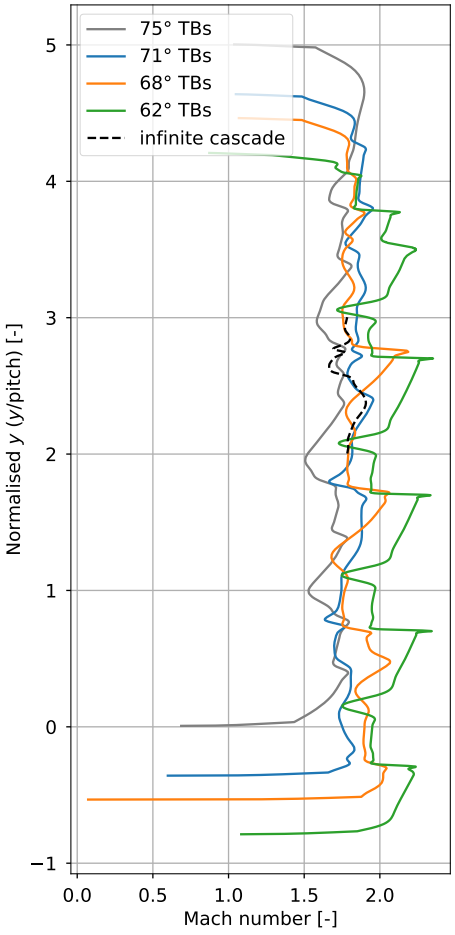

(b) Mach number distribution one chord length behind cascade (in flow direction)

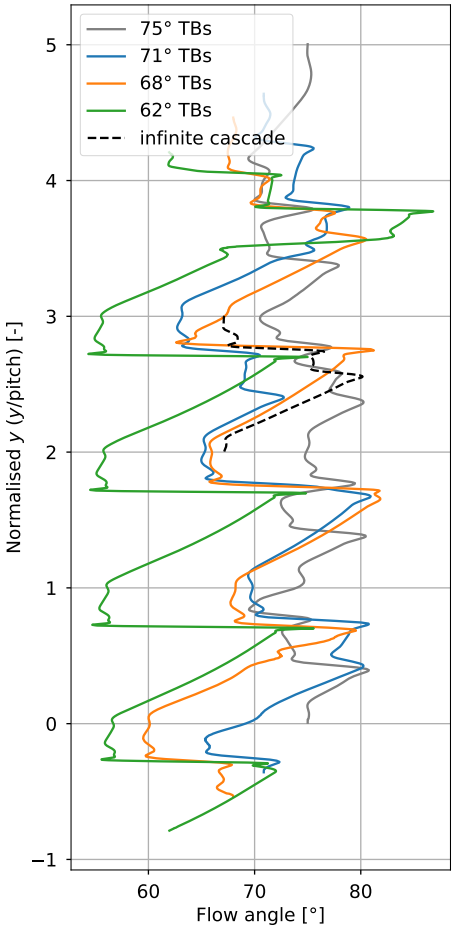

(c) Flow angle distribution one chord length behind cascade (in flow direction)

Figure 4.5: Comparison between different (parallel) tailboard angles for nonideal expansion condition for the five passage cascade test section

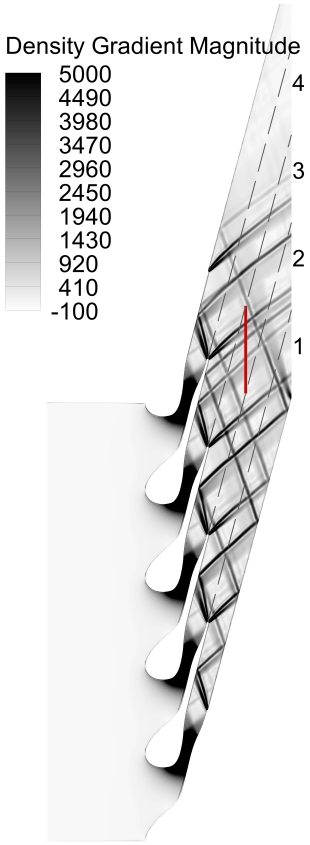

(a) 75° tailboards

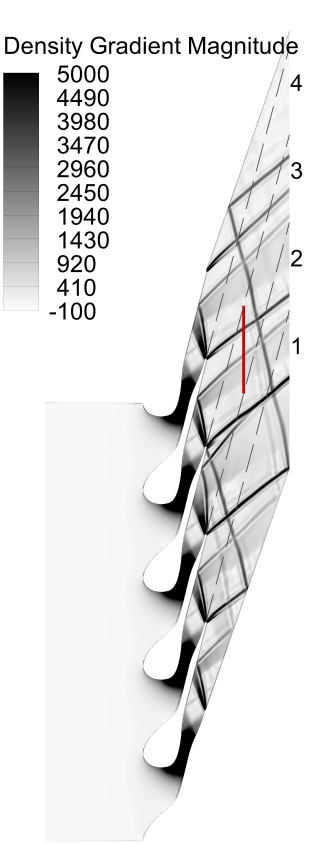

(b) 71° tailboards

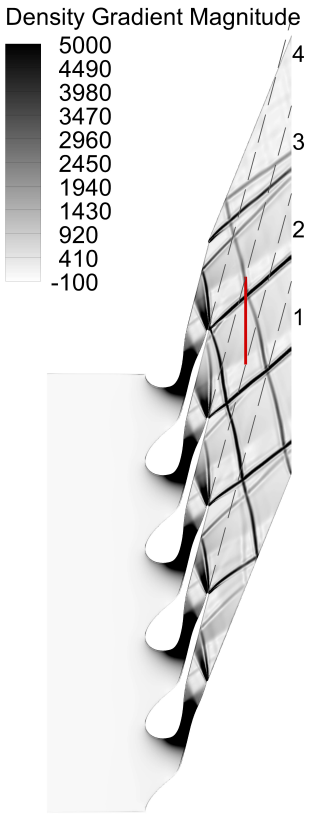

(c) 68° tailboards

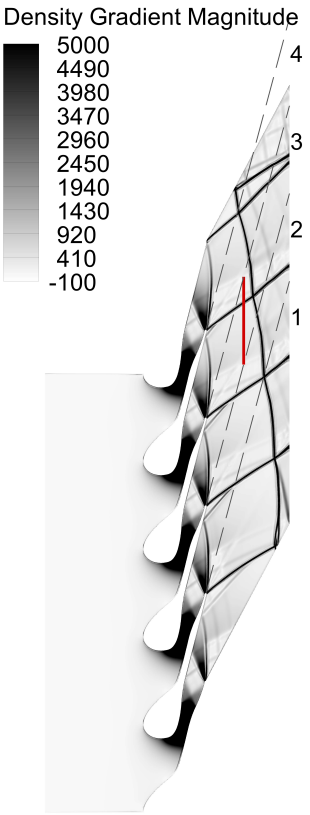

(d) 62° tailboards

Figure 4.6: Numerical Schlieren visualisation of the flow through the five passage cascade with different tailboard angles (both tailboards parallel) using nonmonotonic expansion conditions, where the red line indicates the line distribution in the centre passage

The blade loading curves in Figure 4.5a show that decreasing the angle of the tailboards shifts the impingement location of the trailing edge shock backward. This occurs because the trailing edge shocks rotate with the tailboards. The 71° tailboards give the closest blade loading to the infinite cascade. However, a wall-reflected shock just impinges on the trailing edge. From the blade loadings, it seems that there is a tailboard angle below 71° for which the blade loading will match the infinite cascade; however, there appears to be no way to avoid a wall-reflected shock inside the centre passage in this case. To determine this angle, it is recommended to calculate the average flow angle in a location closer to the trailing edge, since (as discussed in section 4.1) the flow angle downstream of the cascade is affected by multiple wall-reflected shocks.

Investigating the line distributions in Figure 4.5b and Figure 4.5c, it can again be concluded that the angle of the tailboards has a significant effect on the flow of the test section. Again, it seems that the 71° tailboards produce the flow most similar to the infinite cascade. However, with this tailboard angle, the flow in the line distribution is not free from wall-reflected shock waves. This is the case for the 62° tailboard cascade, shown in Figure 4.6. Without the influence of wall-reflected shocks, the line distributions of the 62° tailboard cascade show clear periodic flow for $-0.2 \lesssim y \lesssim 3.5$, until finally a reflected shock is reached within the fourth passage. However, the distribution is far from the one measured in the infinte cascade.

Interestingly, looking closely at the trailing edge shock pattern in Figure 4.6, it seems that the trailing edge shocks of the blade closest to the bottom tailboard are rotated more in the clockwise direction compared to the top blade. To investigate this in more detail, Figure 4.7 shows blade loading curves for the three middle passages of the same test section. Interestingly, the blade loading of the second passage shows a much better blade loading compared to the infinite cascade than the centre passage (passage three in the figure). Critically, the second passage is also free from the wall-reflected shock that is present in the centre passage. This suggests that, with the correct tailboard angle, the blade loading in the second passage could be representative of the blade loading in an infinite cascade. It is also recommended to investigate the flow through a three-passage cascade, since this would allow for an increased blade scale, and thus a better resolution optical measurements.

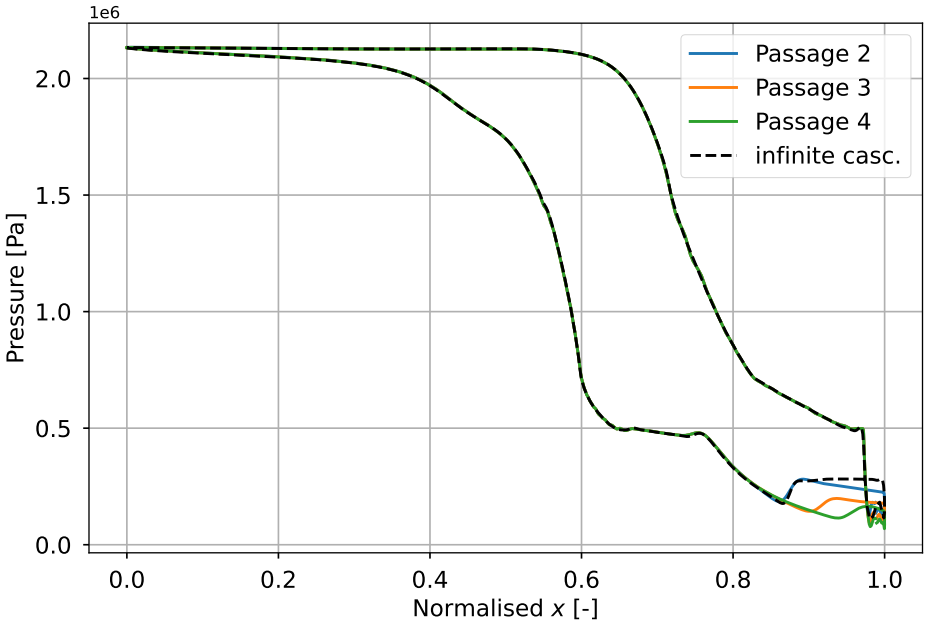

Figure 4.7: Comparison of the blade loading in different passages of the same cascade, with both tailboards at 68°

4.3.2. Effect of Top Tailboard Angle

From the previous section, it can be concluded that both the blade loading and the flow field behind the cascade are significantly affected when rotating both tailboards. There seems to be an exact angle

for each condition for which the blade loading in the centre passage matches the infinite cascade results. However, at this angle, a shock wave can still reflect on the bottom tailboard into the centre passage. For this reason, the following sections investigate whether it is possible to change the blade loading without changing the bottom tailboard angle. In this section, an attempt is made to rotate the top tailboard counterclockwise, in the hope that this pulls some of the flow towards the top tailboard. Hopefully, this will rotate the flow, improving blade loading in the centre passage.

To investigate this, Figure 4.8 shows blade loading curves for the centre passage in a five-passage cascade test section with nonmonotonic expansion conditions. The first cascade investigated has parallel tailboards at 68°. Next, the top tailboard is increasingly rotated counterclockwise, resulting in the other curves. The resulting graph shows that the blade loading in the centre passage is not affected by the top tailboard angle. Additionally, when the tailboards are no longer parallel, the test section area increases towards the outlet. Since the mass flow rate through the test section must be conserved, this would mean that the flow velocity (and thus Mach number) reduces towards the outlet. From the average flow properties listed in Table 4.2, it can be concluded that a slight reduction in the outflow Mach number occurs with increasing rotation of the upper tailboard, as expected. This would mean that, although the effect is minimal, the flow behind the cascade will no longer be representative of an infinite cascade when the tailboards are not parallel. For this reason, and since there is no improvement in the blade loading in the centre passage, it is advised to keep both tailboards parallel.

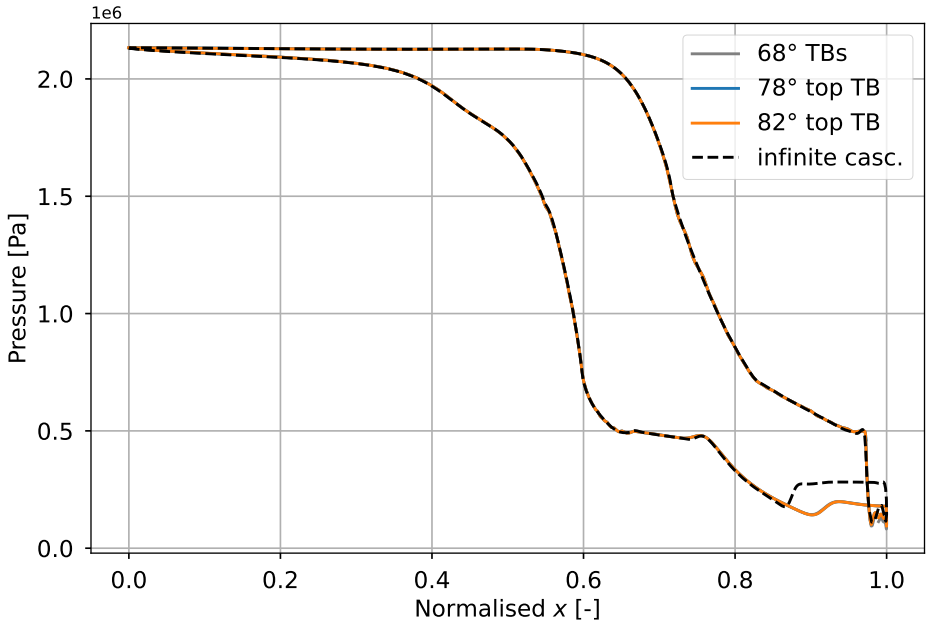

Figure 4.8: Comparison of the blade loading in test sections with different top tailboard angles, with a constant 68° bottom tailboard

Table 4.2: Average in- and outflow properties for the 2D cascade simulations with different angles of the top tailboard

		68° TBs	78° top TB	82° top TB
Outflow Mach number	M_{outlet} [−]	1.769	1.765	1.761
Cascade mass flow rate	$\dot{m}$ [kg/s]	0.947[1]	0.947[1]	0.947[1]
Inlet pressure	P_{inlet} [bar]	21.30	21.30	21.30
Outlet pressure	P_{outlet} [bar]	3.284	3.282	3.282
Total-to-static pressure ratio	β_{ts} [−]	6.497	6.500	6.500

[1] Calculation: $\dot{m} = \dot{m}_{2D} \cdot h_{bl}$

From the results discussed in this chapter, it can be concluded that the angle of the bottom tailbaord has a significant effect on the cascade blade loading. It is critical that the blade loading is representative of that of an infinite (annular) cascade to investigate stator performance. Furthermore, changing the angle of the top tailboard independently does not have a significant effect on blade load. It is expected that the angle of both tailboards must match the flow angle directly behind the cascade of the infinite cascade domain in order to achieve correct blade loading in the centre passage of the cascade test section. Since the three conditions have different flow angles behind the cascade, this will require the tailboards to be changed for each experiment. This can be achieved by using swappable or adjustable tailboards. However, both solutions will add complexity and cost to the project.

Because the angle of the bottom tailboard cannot be changed without adversely affecting the test section flow, the locations of the reflected shocks on the wall cannot be changed. Somewhat counter-intuitively, the results indicate that reducing the number of cascade passages to three could improve the centre passage blade loading by avoiding the wall-reflected shocks in the centre passage. This still means that wall-reflected shocks in the flow behind the cascade are unavoidable. Another solution could be to increase the design Mach number. A higher Mach number will result in a sharper trailing edge shock structure, meaning that the angle between the trailing edge shocks and the wake (see Figure 2.2) will be lower. This will cause the shock impingement location on the bottom tailboard to be further downstream. Thus, the wall-reflected shocks will also be further downstream. However, this approach does constrain the range of blade designs that can be tested.

4.4. Proposed Cascade Test Section Layout

Based on the results discussed in this chapter, some design desisions can be made for the final linear cascade test section. Although the results show that the design of the cascade side walls and specifically the tailboards still requires further research, the cascade design itself performs as expected and within the limits of the ORCHID facility. For this reason, the proposed cascade design is reported in this section.

Based on the comparison between the five- and seven-passage cascades, the five-passage cascade design is selected for the test section. The cascade specifications are summarised in Table 4.3. From the number of passages and the pitch of the cascade, the final cascade width can be determined to be 128.5 mm. This is smaller than the cascade width of 225 mm of the preliminary cascade design discussed in section 2.6. This means that only the height of the test section housing and the inserts for the cascade side walls need to be changed.

Table 4.3: Specifications of the final cascade test section

Specification		Value
Number of passages	n_{pass} [−]	5
Outflow Mach number	M_{outlet} [−]	1.83
Post-expansion ratio	$\beta_{\text{PE,opt}}$ [−]	1.06
Trailing edge-to-pitch ratio	t/p [%]	2
Design flow angle	ϕ_{a} [°]	75
Solidity	$\sigma(=\frac{C}{p})$ [−]	1.66
Trailing edge thickness	t [mm]	0.513
Blade height	h_{bl} [mm]	6.40
Throat width	w_{th} [mm]	3.20
Chord length	C [mm]	42.7
Pitch	p [mm]	25.7

In addition to the consideration of cascade size, other design considerations of the test section must be discussed. First, during the review of measurement techniques, it was discovered that the test section requires one-sided optical access and a replacable back wall behind the measurement area. In addition, the stator cascade must be exchangable, since one of the experimental goals is to develop design guidelines, which requires measurements of different stator geometries. The preliminary test

section housing design uses a rotatable and replacable disc attached to the back wall of the housing to attach the stator cascade, discussed in detail by Haur [74]. This allows for the easy replacement of both the back wall at the desired measurement area and replacement of the cascade. For this reason, the preliminary design of the test section housing is well suited for the intended experimental campaign.

A final consideration are the cascade side walls. As discovered during this research, the thermodynamic condition of the expansion has a significant effect on the flow angle behind the cascade. This requires different side walls to ensure that the flow behaves as it would in an annular cascade. For this reason, the side walls of the cascade must be replacable. Although this has been implemented in the preliminary housing design, the process is much more time-consuming than replacing the cascade because the entire test section housing must be unbolded. It is recommended to investigate whether this design aspect can be improved.

5

Conclusions & Recommendations

To conclude this report, section 5.1 summarises the findings of this work and formulates answers to the research questions. To help researchers who plan to continue the design process of a linear cascade test section, section 5.2 offers some recommendations for future research.

5.1. Conclusions

In chapter 1, the objective of this project was presented as a set of research questions. This section combines the relevant findings of this report to answer the research questions, starting with the subquestions listed below.

1. *What is the best measurement approach to acquire validation data which is unaffected by wall-reflected shock waves in on- and off-design conditions?*

   Based on a review of the state of the art of NICFD measurement techniques, it can be concluded that the use of intrusive measurement techniques like Pitot-tubes or hot-wire anemometry in NICFD flows is complicated by the high density supersonic flows involved. Additionally, these techniques require complicated sealing and traversing mechanisms if different measurement locations are to be considered. For these reasons, the experimental campaign should instead use optical measurement techniques, in combination with static pressure measurements using the static pressure measurement system already implemented in the *ORCHID* facility. Static pressure tap locations must be carefully placed when the final tailboard angle is determined, to avoid wall-reflected shock waves. In off-design conditions, wall-reflected shock locations will change. If measurements in off-design conditions are considered, this must be taken into account when selecting the pressure tap locations.

   For the optical measurements, one-sided optical access was already considered in the preliminary test section housing design. Using this optical access, particle image velocimetry and double-passage Schlieren imaging can be used together with static pressure measurements to determine the pressure loss coefficient and exit flow uniformity coefficient to characterise stator performance. In addition, BOS can provide density data which can further advance the validation of numerical solvers for NICFD application. Lastly, although unproven in NICFD experiments, infrared thermal imaging can potentially provide insight into wall heat-transfer and boundary layer laminar to turbulent transition. Allowing researchers to validate the commonly used adiabatic flow modelling assumption, as well as the ability of numerical models to accurately predict boundary layer transition.

2. *How to design different linear stator cascades for different thermodynamic conditions, while maintaining the same blade height, Reynolds number and Mach number?*

Within this research, three expansion conditions were selected based on isentropic expansion line calculations. The three expansions were chosen to have different thermodynamic properties, where the ”ideal” expansion was as close as possible to ideal gas properties. The ”nonideal” condition had nonideal properties but monotonic evolution of the fundamental derivative of gas dynamics along the expansion line. Finally, the ”nonmonotonic” condition had the most nonideal fluid properties and a nonmonotonic evolution of the fundamental derivative along the expansion line. A constant exit Mach number between the three conditions was achieved by tailoring the total-to-static pressure ratio of each expansion line.

To determine the scale of the blades used in the cascade, the maximum allowable total throat area was determined based on the maximum thermal power of the *ORCHID* facility. This thermal power was determined based on the thermal power required for the currently installed planar nozzle test section and reducing this value by 20% to take into account the degradation of the *ORCHID* heat exchangers. Scaling the stator vanes to achieve the same Reynolds number showed that the blades for the ideal condition had to be roughly twice the size of those for the nonmonotonic condition. This was deemed infeasible to integrate into a single test section. Because of this, and to avoid having to switch out the cascade for each experiment, the constant Reynolds number requirement was removed. Ultimately, at the high Reynolds numbers found in supersonic turbomachinery, the difference in Reynolds number has little effect on the boundary layer losses.

Without the Reynolds number requirement, the decision was made to use a single cascade design for the all experimental conditions. The final blade scale and blade height were determined by setting the blade height-to-throat ratio to two-to-one, in order to ensure sufficient blade height such that no boundary layer effects are present in the midplane of the cascade. Then, the maximum throat area of a single passage is determined by dividing the total allowable throat area based on the thermal power constraint by the number of passages of the cascade. This area then decides the passage height and throat width and thus the blade scale.

3. *What is the optimal number of flow passages to achieve flow periodicity and minimise the effect of wall-reflected shock waves?*

A detail numerical analysis has been performed comparing the flow field through five- and seven-passage cascade test sections. The results show that the blade loading in the centre passage of the five-passage cascade test section already matches that of an infinite cascade closely, except at the location of the trailing edge shock impingement. The seven-passage cascade does not seem to improve this blade loading or the flow periodicity in the flow behind the cascade compared to the five-passage cascade. Since the five passage cascade has a larger blade scale, and since a larger blade scale provides better measurement resolution for optical measurement techniques, a five passage cascade is considered to be the better configuration.

Interestingly, results show that the passage below the centre passage of the cascade shows a blade loading which is closer to that of an infinite cascade. This is because the trailing edge shock wave that impinges the suction side of the top blade of the passage is less affected by the angle of the bottom tailboard. Furthermore, this passage is free from wall-reflected shock waves coming from the bottom tailboard, as opposed to the centre passage. These insight suggest that a three passage cascade could be a feasible, and possibly better, alternative to the five passage cascade test section.

Finally, the main research question can be answered:

What is the optimal design of a test section to investigate NICFD flows in a linear stator-vane cascade using the ORCHID facility?

Based on the analyses performed, the main criteria for an optimal linear stator-vane cascade test section can be summarised as follows:

- The cascade should consist of a maximum of five passages;
- Possibly, three passages could be used to achieve better blade loading if this avoids wall-reflected shock impingement in the centre passage;
- The test section tailboards should be parallel and their angle must be set carefully to avoid affecting the cascade blade loading;
- Since rotating the bottom tailboard influences the flow inside the cascade, other shock mitigation strategies like shock absorbing walls should be considered;
- Since the flow angle behind the cascade changes between different conditions, tailboards should be adjustable or swappable;
- A test section with a blade height of twice the cascade throat width is sufficiently high to achieve two-dimensional flow in the midplane of the test section;
- One-sided optical access is required and easy replacement of backplate and cascade is highly recommended.

5.2. Recommendations

The analysis within this report discovered multiple factors that complicate the design of a linear cascade test section for NICFD flows. As a result, additional research is required before the design of the linear cascade test section can be finalised. For this purpose, the following tasks and research topics are suggested:

- Adapt *SU2* so the Giles boundary condition can be applied to three-dimensional domains without periodic boundary conditions, to allow for evaluation of the complete test section without artificial shock reflections on the outflow boundary;
- Investigate the cause of the reduction in cascade exit flow angle with increasingly nonideal working fluid conditions in more detail;
- Compare the three expansion condition flow fields in infinite cascade domains using blade designs that are optimised for each expansion to better compare cascade losses;
- Confirm that the centre passage blade loading exactly matches the infinite cascade blade loading when the tailboards are aligned with the flow angle determined behind the stator trailing edge in the infinite cascade CFD results;
- Investigate if cascade blade loading improves when using cascade walls based on streamlines from infinite cascade numerical simulations close to the blade surface instead of straight tailboards;
- Investigate the effectiveness of shock absorbing tailboard techniques like slotted tailboards and their impact on test section flow;
- Conduct a detailed analysis of the application of infrared thermal imaging for investigating wall heat flux and boundary layer transition in the linear cascade test section;
- Finally, evaluate the preliminary design of the test section setup and integrate the final cascade and tailboard designs to create a detailed assembly design.

References

[1] D.-Y. Peng and D. B. Robinson. “A New Two-Constant Equation of State”. en. In: *Industrial & Engineering Chemistry Fundamentals* 15.1 (Feb. 1976), pp. 59–64. ISSN: 0196-4313, 1541-4833. DOI: 10.1021/i160057a011.

[2] E. Lemmon, M. Huber, and M. McLinden. “NIST Standard Reference Database 23: Reference Fluid Thermodynamic and Transport Properties-REFPROP, Version 9.1”. en. In: (May 2013). Publisher: Natl Std. Ref. Data Series (NIST NSRDS), National Institute of Standards and Technology, Gaithersburg, MD. URL: https://tsapps.nist.gov/publication/get_pdf.cfm?pub_id=912382.

[3] I. H. Bell et al. “Pure and Pseudo-pure Fluid Thermophysical Property Evaluation and the Open-Source Thermophysical Property Library CoolProp”. en. In: *Industrial & Engineering Chemistry Research* 53.6 (Feb. 2014), pp. 2498–2508. ISSN: 0888-5885, 1520-5045. DOI: 10.1021/ie4033999.

[4] A. Head. “Novel Experiments for the Investigation of Non-Ideal Compressible Fluid Dynamics: The ORCHID and First Results of Optical Measurements”. PhD thesis. Delft University of Technology, 2021. DOI: 10.4233/UUID:A3B03976-2DF6-435C-B7DF-1505718FCD3A.

[5] L. Bills. “Validation of the SU2 flow solver for classical non ideal compressible fluid dynamics”. MA thesis. Delft University of Technology, 2020. URL: https://resolver.tudelft.nl/uuid:d1cb88d5-7bcd-4c4f-88c3-d4818c272661 (visited on 03/18/2025).

[6] G. Hariharan. “Expansions in the Non-Ideal Compressible Flow Regime”. MA thesis. Delft University of Technology, Oct. 2021. URL: https://resolver.tudelft.nl/uuid:3525b371-6421-4845-b7c0-cec2cb74c796 (visited on 03/18/2025).

[7] R. Vello. “A validation infrastructure for non-ideal compressible fluid dynamics”. MA thesis. Delft University of Technology, 2021. URL: http://resolver.tudelft.nl/uuid:fa35f47e-1d1e-49f2-af3a-615eafea28c1 (visited on 03/18/2025).

[8] E. Rinaldi, R. Pecnik, and P. Colonna. “Unsteady Operation of a Highly Supersonic Organic Rankine Cycle Turbine”. en. In: *Journal of Turbomachinery* 138.12 (Dec. 2016), p. 121010. ISSN: 0889-504X, 1528-8900. DOI: 10.1115/1.4033973.

[9] S. Sudhof. “Development Techniques for Supersonic Turbines”. Dissertation. Lampoldshausen: Universität Stuttgart, Luft- und Raumfahrttechnik und Geodäsie, 2020. URL: https://elib.dlr.de/139719/ (visited on 01/24/2025).

[10] J. D. Denton and L. Xu. “The Trailing Edge Loss of Transonic Turbine Blades”. en. In: *Journal of Turbomachinery* 112.2 (Apr. 1990), pp. 277–285. ISSN: 0889-504X, 1528-8900. DOI: 10.1115/1.2927648.

[11] E. Rinaldi, R. Pecnik, and P. Colonna. “Exact Jacobians for implicit Navier–Stokes simulations of equilibrium real gas flows”. en. In: *Journal of Computational Physics* 270 (Aug. 2014), pp. 459–477. ISSN: 00219991. DOI: 10.1016/j.jcp.2014.03.058.

[12] M. Giovannini et al. “Evaluation of unsteady computational fluid dynamics models applied to the analysis of a transonic high-pressure turbine stage”. en. In: *Proceedings of the Institution of Mechanical Engineers, Part A: Journal of Power and Energy* 228.7 (Nov. 2014), pp. 813–824. ISSN: 0957-6509, 2041-2967. DOI: 10.1177/0957650914536170.

[13] J. D. van der Waals. “Over de continuiteit van den gas- en vloeistoftoestand”. PhD Thesis. Leiden: Universiteit Leiden, 1873.

[14] A. Guardone et al. “Nonideal Compressible Fluid Dynamics of Dense Vapors and Supercritical Fluids”. en. In: *Annual Review of Fluid Mechanics* 56.1 (Jan. 2024), pp. 241–269. ISSN: 0066-4189, 1545-4479. DOI: 10.1146/annurev-fluid-120720-033342.

[15] S. A. D. Wiesche. “Experimental Investigation Techniques for Non-Ideal Compressible Fluid Dynamics”. en. In: *International Journal of Turbomachinery, Propulsion and Power* 8.2 (Apr. 2023), p. 11. ISSN: 2504-186X. DOI: 10.3390/ijtpp8020011.

[16] L. D. Landau. “On shock waves”. In: *J. Phys.* 6 (1942), pp. 229–230.

[17] W. D. Hayes. “The Basic Theory of Gasdynamic Discontinuities”. In: *Fundamentals of Gas Dynamics*. Princeton University Press, Dec. 1958, pp. 416–481. ISBN: 978-1-4008-7753-9. DOI: 10.1515/9781400877539-006.

[18] P. A. Thompson. “A Fundamental Derivative in Gasdynamics”. en. In: *The Physics of Fluids* 14.9 (Sept. 1971), pp. 1843–1849. ISSN: 0031-9171. DOI: 10.1063/1.1693693.

[19] P. Post. “Development of Efficient Numerical Methods for Non-Ideal Compressible Fluid Flows in Propulsion and Power”. Dissertation. Bochum: Ruhr-Universitat, 2020. URL: https://hss-opus.ub.ruhr-uni-bochum.de/opus4/frontdoor/index/index/docId/7592 (visited on 01/28/2025).

[20] P. Colonna and P. Silva. “Dense Gas Thermodynamic Properties of Single and Multicomponent Fluids for Fluid Dynamics Simulations”. In: *Journal of Fluids Engineering* 125.3 (May 2003), pp. 414–427. ISSN: 0098-2202, 1528-901X. DOI: 10.1115/1.1567306.

[21] T. Van Der Stelt, N. Nannan, and P. Colonna. “The iPRSV equation of state”. en. In: *Fluid Phase Equilibria* 330 (Sept. 2012), pp. 24–35. ISSN: 03783812. DOI: 10.1016/j.fluid.2012.06.007.

[22] G. Soave. “Equilibrium constants from a modified Redlich-Kwong equation of state”. en. In: *Chemical Engineering Science* 27.6 (June 1972), pp. 1197–1203. ISSN: 00092509. DOI: 10.1016/0009-2509(72)80096-4.

[23] R. Span and W. Wagner. “Equations of State for Technical Applications. I. Simultaneously Optimized Functional Forms for Nonpolar and Polar Fluids”. In: *International Journal of Thermophysics* 24.1 (2003), pp. 1–39. ISSN: 0195928X. DOI: 10.1023/A:1022390430888.

[24] A. Guardone, A. Spinelli, and V. Dossena. “Influence of Molecular Complexity on Nozzle Design for an Organic Vapor Wind Tunnel”. en. In: *Journal of Engineering for Gas Turbines and Power* 135.4 (Apr. 2013), p. 042307. ISSN: 0742-4795, 1528-8919. DOI: 10.1115/1.4023117.

[25] A. bv. *FluidProp Details*. URL: https://asimptote.com/fluidprop/fluidprop-details/ (visited on 01/28/2025).

[26] K. Duff. “Non-Equilibrium Condensation of Carbon Dioxide in Supersonic Nozzles”. PhD Thesis. MA, USA: M.I.T. Dept. of Mechenical Engineering, 1966.

[27] G. Dettleff et al. “An experimental study of liquefaction shock waves”. en. In: *Journal of Fluid Mechanics* 95.2 (Nov. 1979), pp. 279–304. ISSN: 0022-1120, 1469-7645. DOI: 10.1017/S0022112079001476.

[28] S. S. Kutateladze, V. E. Nakoryakov, and A. A. Borisov. “Rarefaction Waves in Liquid and Gas-Liquid Media”. In: *Annual Review of Fluid Mechanics* 19 (1987), pp. 577–600. DOI: https://doi.org/10.1146/annurev.fl.19.010187.003045.

[29] K. Bier, F. Ehrler, and G. Theis. “Spontaneous Condensation in Stationary Nozzle Flow of Carbon Dioxide in a Wide Range of Density”. en. In: *Adiabatic Waves in Liquid-Vapor Systems*. Ed. by G. E. A. Meier and P. A. Thompson. Berlin, Heidelberg: Springer Berlin Heidelberg, 1990, pp. 129–141. ISBN: 978-3-642-83587-2. DOI: 10.1007/978-3-642-83587-2_12.

[30] J. B. Anders, W. K. Anderson, and A. V. Murthy. “Transonic Similarity Theory Applied to a Supercritical Airfoil in Heavy Gas”. en. In: *Journal of Aircraft* 36.6 (Nov. 1999), pp. 957–964. ISSN: 0021-8669, 1533-3868. DOI: 10.2514/2.2557.

[31] S. Fergason and B. Argrow. “Construction and operation of a dense gas shock tube”. en. In: *35th AIAA Thermophysics Conference*. Anaheim,CA,U.S.A.: American Institute of Aeronautics and Astronautics, June 2001. DOI: 10.2514/6.2001-2747.

[32] P. Colonna et al. “Design of the Dense Gas Flexible Asymmetric Shock Tube”. en. In: *Journal of Fluids Engineering* 130.3 (Mar. 2008), p. 034501. ISSN: 0098-2202, 1528-901X. DOI: 10.1115/1.2844585.

[33] T. Mathijssen et al. “The flexible asymmetric shock tube (FAST): a Ludwieg tube facility for wave propagation measurements in high-temperature vapours of organic fluids”. en. In: *Experiments in Fluids* 56.10 (Oct. 2015), p. 195. ISSN: 0723-4864, 1432-1114. DOI: 10.1007/s00348-015-2060-1.

[34] T. Delft. *Facilities*. URL: https://www.tudelft.nl/lr/organisatie/afdelingen/flow-physics-and-technology/facilities (visited on 01/20/2025).

[35] N. Chandrasekaran. “Nonclassical gasdynamics: theory and experiments on nonlinear wave propagation in BZT fluids”. PhD thesis. Delft University of Technology, 2023. URL: http://resolver.tudelft.nl/uuid:65d578ce-b904-466f-a57e-4086dbee4a98 (visited on 01/20/2025).

[36] F. J. Durá Galiana et al. “The effect of dense gas dynamics on loss in ORC transonic turbines”. In: *Journal of Physics: Conference Series* 821 (Mar. 2017), p. 012021. ISSN: 1742-6588, 1742-6596. DOI: 10.1088/1742-6596/821/1/012021.

[37] F. J. Durá Galiana, A. P. Wheeler, and J. Ong. “A Study of Trailing-Edge Losses in Organic Rankine Cycle Turbines”. en. In: *Journal of Turbomachinery* 138.12 (Dec. 2016), p. 121003. ISSN: 0889-504X, 1528-8900. DOI: 10.1115/1.4033473.

[38] D. Baumgärtner, J. J. Otter, and A. P. S. Wheeler. “The Effect of Isentropic Exponent on Transonic Turbine Performance”. en. In: *Journal of Turbomachinery* 142.8 (Aug. 2020), p. 081007. ISSN: 0889-504X, 1528-8900. DOI: 10.1115/1.4046528.

[39] M. White. “Workshop on experimental test facilities”. In: *Proceedings of the 4th International Seminar on Non-Ideal Compressible Fluid Dynamics (NICFD2022)*. London, UK: City University, Nov. 2022.

[40] M. Robertson et al. “Experimental and Numerical Study of Supersonic Non-ideal Flows for Organic Rankine Cycle Applications”. en. In: *Journal of Engineering for Gas Turbines and Power* 142.8 (Aug. 2020), p. 081007. ISSN: 0742-4795, 1528-8919. DOI: 10.1115/1.4046758.

[41] M. Carmine et al. “Evidence of complex flow structures in a converging-diverging nozzle caused by a recessed step at the nozzle throat”. en. In: *45th AIAA Fluid Dynamics Conference*. Dallas, TX: American Institute of Aeronautics and Astronautics, June 2015. ISBN: 978-1-62410-362-9. DOI: 10.2514/6.2015-2311.

[42] A. Spinelli et al. “Experimental Observation Of Non-Ideal Nozzle Flow Of Siloxane Vapor MDM”. In: *3rd International Seminar on ORC Power Systems*. Brussels, Belgium: University of Liège and Ghent University, Oct. 2015, pp. 232–243. ISBN: 978-2-9600059-2-9. URL: http://asme-orc2015.fyper.com/ (visited on 01/21/2025).

[43] A. Spinelli et al. “Experimental observation of non-ideal expanding flows of Siloxane MDM vapor for ORC applications”. en. In: *Energy Procedia* 129 (Sept. 2017), pp. 1125–1132. ISSN: 18766102. DOI: 10.1016/j.egypro.2017.09.237.

[44] A. Spinelli et al. “Experimental evidence of non-ideal compressible effects in expanding flow of a high molecular complexity vapor”. en. In: *Experiments in Fluids* 59.8 (Aug. 2018), p. 126. ISSN: 0723-4864, 1432-1114. DOI: 10.1007/s00348-018-2578-0.

[45] A. Spinelli et al. “Experimental observation and thermodynamic modeling of non-ideal expanding flows of siloxane MDM vapor for ORC applications”. en. In: *Energy* 168 (Feb. 2019). Publisher: Elsevier BV, pp. 285–294. ISSN: 0360-5442. DOI: 10.1016/j.energy.2018.11.071.

[46] M. Zocca et al. “Experimental observation of oblique shock waves in steady non-ideal flows”. en. In: *Experiments in Fluids* 60.6 (June 2019), p. 101. ISSN: 0723-4864, 1432-1114. DOI: 10.1007/s00348-019-2746-x.

[47] G. Cammi et al. “Experimental characterization of nozzle flow expansions of siloxane MM for ORC turbines applications”. English. In: *Energy* 218 (2021). Publisher: Elsevier Ltd. ISSN: 03605442 (ISSN). DOI: 10.1016/j.energy.2020.119249.

[48] C. Conti et al. “Shock losses and pitot tube measurements in non-ideal supersonic and subsonic flows of organic vapors”. en. In: (Nov. 2021). Medium: PDF Publisher: Technical University of Munich. DOI: 10.14459/2021MP1633108.

[49] M. Manfredi et al. “Design and commissioning of experiments for supersonic ORC nozzles in linear cascade configuration”. en. In: *Applied Thermal Engineering* 224 (Apr. 2023), p. 119996. ISSN: 13594311. DOI: 10.1016/j.applthermaleng.2023.119996.

[50] M. Manfredi et al. “Loss Measurement Strategy in ORC Supersonic Blade Cascades”. en. In: *Proceedings of the 4th International Seminar on Non-Ideal Compressible Fluid Dynamics for Propulsion and Power*. Ed. by M. White et al. Vol. 29. Series Title: ERCOFTAC Series. Cham: Springer Nature Switzerland, 2023, pp. 217–228. ISBN: 978-3-031-30936-6. DOI: 10.1007/978-3-031-30936-6_22.

[51] M. Manfredi et al. “Nitrogen Experiments on a Supersonic Linear Cascade For ORC Applications”. en. In: *Journal of Physics: Conference Series* 2511.1 (May 2023), p. 012022. ISSN: 1742-6588, 1742-6596. DOI: 10.1088/1742-6596/2511/1/012022.

[52] S. Gallarini et al. “Direct velocity measurements in high-temperature non-ideal vapor flows”. en. In: *Experiments in Fluids* 62.10 (Oct. 2021), p. 199. ISSN: 0723-4864, 1432-1114. DOI: 10.1007/s00348-021-03295-4.

[53] F. Beltrame et al. “First Experiments and Commissioning of the ORCHID Nozzle Test Section”. en. In: *Proceedings of the 3rd International Seminar on Non-Ideal Compressible Fluid Dynamics for Propulsion and Power*. Ed. by M. Pini et al. Vol. 28. Series Title: ERCOFTAC Series. Cham: Springer International Publishing, 2021, pp. 169–178. ISBN: 978-3-030-69306-0. DOI: 10.1007/978-3-030-69306-0_18.

[54] A. J. Head et al. “Mach Number Estimation and Pressure Profile Measurements of Expanding Dense Organic Vapors”. en. In: *Proceedings of the 4th International Seminar on Non-Ideal Compressible Fluid Dynamics for Propulsion and Power*. Ed. by M. White et al. Vol. 29. Series Title: ERCOFTAC Series. Cham: Springer Nature Switzerland, 2023, pp. 229–238. ISBN: 978-3-031-30935-9. DOI: 10.1007/978-3-031-30936-6_23.

[55] T. Michelis et al. “Assessment of particle image velocimetry applied to high-speed organic vapor flows”. en. In: *Experiments in Fluids* 65.6 (June 2024), p. 90. ISSN: 0723-4864, 1432-1114. DOI: 10.1007/s00348-024-03822-z.

[56] F. Reinker et al. “High subsonic flow of an organic vapor past a circular cylinder”. en. In: *Experiments in Fluids* 62.3 (Mar. 2021), p. 54. ISSN: 0723-4864, 1432-1114. DOI: 10.1007/s00348-021-03158-y.

[57] F. Reinker et al. “Performance of a Rotatable Cylinder Pitot Probe in High Subsonic Non-ideal Gas Flows”. en. In: *Proceedings of the 3rd International Seminar on Non-Ideal Compressible Fluid Dynamics for Propulsion and Power*. Ed. by M. Pini et al. Vol. 28. Series Title: ERCOFTAC Series. Cham: Springer International Publishing, 2021, pp. 144–152. ISBN: 978-3-030-69306-0. DOI: 10.1007/978-3-030-69306-0_15.

[58] S. Sundermeier et al. “Experimental and Numerical Study of Transonic Flow of an Organic Vapor Past a Circular Cylinder”. en. In: *Proceedings of the 4th International Seminar on Non-Ideal Compressible Fluid Dynamics for Propulsion and Power*. Ed. by M. White et al. Vol. 29. Series Title: ERCOFTAC Series. Cham: Springer Nature Switzerland, 2023, pp. 209–216. ISBN: 978-3-031-30935-9. DOI: 10.1007/978-3-031-30936-6_21.

[59] F. Reinker and S. Aus Der Wiesche. “Application of Hot-Wire Anemometry in the High Subsonic Organic Vapor Flow Regime”. en. In: *Proceedings of the 3rd International Seminar on Non-Ideal Compressible Fluid Dynamics for Propulsion and Power*. Ed. by M. Pini et al. Vol. 28. Series Title: ERCOFTAC Series. Cham: Springer International Publishing, 2021, pp. 135–143. ISBN: 978-3-030-69306-0. DOI: 10.1007/978-3-030-69306-0_14.

[60] L. Hake, S. Sundermeier, and S. A. D. Wiesche. “Profile Loss Prediction for Organic Rankine Cycle Turbines: An Experimental Case Study”. en. In: *International Journal of Turbomachinery, Propulsion and Power* 8.4 (Dec. 2023), p. 51. ISSN: 2504-186X. DOI: 10.3390/ijtpp8040051.

[61] L. Hake et al. “The Profile Loss of Additive Manufactured Blades for Organic Rankine Cycle Turbines”. en. In: *International Journal of Turbomachinery, Propulsion and Power* 7.1 (Mar. 2022), p. 11. ISSN: 2504-186X. DOI: 10.3390/ijtpp7010011.

[62] D. Baumgärtner, J. J. Otter, and A. P. S. Wheeler. “The Effect of Isentropic Exponent on Supersonic Turbine Wakes”. en. In: *Proceedings of the 3rd International Seminar on Non-Ideal Compressible Fluid Dynamics for Propulsion and Power*. Ed. by M. Pini et al. Vol. 28. Series Title: ERCOFTAC Series. Cham: Springer International Publishing, 2021, pp. 153–161. ISBN: 978-3-030-69306-0. DOI: 10.1007/978-3-030-69306-0_16.

[63] C. Antonini, G. Persico, and A. L. Rowe. “Prediction of the dynamic response of complex transmission line systems for unsteady pressure measurements”. In: *Measurement Science and Technology* 19.12 (Dec. 2008), p. 125401. ISSN: 0957-0233. DOI: 10.1088/0957-0233/19/12/125401.

[64] D. Baumgärtner. “Real gas effects in ORC turbines”. PhD thesis. Apollo - University of Cambridge Repository, Aug. 2020. DOI: 10.17863/CAM.69867.

[65] C. C. Conti et al. “Pneumatic system for pressure probe measurements in transient flows of non-ideal vapors subject to line condensation”. en. In: *Measurement* 192 (Mar. 2022), p. 110802. ISSN: 02632241. DOI: 10.1016/j.measurement.2022.110802.

[66] L. Hake et al. “Grid-Generated Decaying Turbulence in an Organic Vapour Flow”. en. In: *Proceedings of the 4th International Seminar on Non-Ideal Compressible Fluid Dynamics for Propulsion and Power*. Ed. by M. White et al. Vol. 29. Series Title: ERCOFTAC Series. Cham: Springer Nature Switzerland, 2023, pp. 181–190. ISBN: 978-3-031-30936-6. DOI: 10.1007/978-3-031-30936-6_18.

[67] G. Cammi. “MEASUREMENTS TECHNIQUES FOR NON-IDEAL COMPRESSIBLE FLUID FLOWS: APPLICATIONS TO ORGANIC FLUIDS”. Dissertation. Milan, Italy: Politecnico di Milano, 2019. URL: https://www.politesi.polimi.it/handle/10589/148759 (visited on 01/31/2025).

[68] C. C. Conti et al. “Schlieren Visualizations of Non-Ideal Compressible Fluid Flows”. In: Portoroz, Slovenia: University of Pretoria, July 2017, pp. 513–518. URL: http://hdl.handle.net/2263/62466 (visited on 01/31/2025).

[69] A. Spinelli et al. “Preliminary characterization of an expanding flow of siloxane vapor MDM”. en. In: *Journal of Physics: Conference Series* 821 (Mar. 2017), p. 012022. ISSN: 1742-6588, 1742-6596. DOI: 10.1088/1742-6596/821/1/012022.

[70] C. Hirsch, ed. *Advanced methods for cascade testing: = (Méthodes avancées pour les essais des grilles d’aubes)*. en. AGARDograph 328. Neuilly sur Seine: AGARD, 1993. ISBN: 978-92-835-0717-8.

[71] U. Fey, K. Groot de, and Y. Le Sant. *Thermography as a tool in wind tunnel testing*. Tech. rep. DLR, 2010. URL: https://elib.dlr.de/52019/.

[72] M. Sisti et al. “Infrared temperature measurements on high pressure turbine blades in the Oxford Turbine Research Facility: calibration and image processing techniques”. en. In: *European Conference on Turbomachinery Fluid Dynamics and Thermodynamics*. Gdansk, Poland: European Turbomachinery Society, 2021. DOI: 10.29008/etc2021-780.

[73] M. van der Groen. *The Design of a Cascade Vapor Tunnel Test Section*. Internship Report. Delft: Hogeschool InHolland, Jan. 2021.

[74] E. Haur. *Designing of the rotating cascade test section for the TU Delft ORCHID facility*. Internship Report. Delft: Hogeschool InHolland, Jan. 2021.

[75] D. Zuna. *Mechanical Design of the Linear Cascade*. Internship Report. Delft: Hogeschool InHolland, Jan. 2021.

[76] A. Giuffre and M. Pini. “NiceProp: An interactive Python-based educational tool for non-ideal compressible fluid dynamics”. en. In: *SoftwareX* 17 (Jan. 2022), p. 100897. ISSN: 23527110. DOI: 10.1016/j.softx.2021.100897.

[77] N. Anand. “Supersonic Turbine Design using Method of Characteristics”. en. MA thesis. 2016. URL: https://repository.tudelft.nl/record/uuid:f6b5bcbb-e894-4361-a1d0-48e6429e3ae4 (visited on 03/12/2025).

[78] A. Cappiello et al. “On the Influence of Stator-Rotor Radial Gap Size on the Fluid-Dynamic Performance of Mini-ORC Supersonic Turbines”. In: *Volume 10B: Turbomachinery — Axial Flow Turbine Aerodynamics; Deposition, Erosion, Fouling, and Icing; Radial Turbomachinery Aerodynamics*. Rotterdam, Netherlands: American Society of Mechanical Engineers, June 2022, V10BT35A015. ISBN: 978-0-7918-8610-6. DOI: 10.1115/GT2022-83309.

[79] N. Anand, P. Colonna, and M. Pini. “Design guidelines for supersonic stators operating with fluids made of complex molecules”. en. In: *Energy* 203 (July 2020), p. 117698. ISSN: 03605442. DOI: 10.1016/j.energy.2020.117698.

[80] J. D. Denton. “The 1993 IGTI Scholar Lecture: Loss Mechanisms in Turbomachines”. en. In: *Journal of Turbomachinery* 115.4 (Oct. 1993), pp. 621–656. ISSN: 0889-504X, 1528-8900. DOI: 10.1115/1.2929299.

[81] A. Ghidoni et al. “3D anisotropic unstructured grid generation”. en. In: *International Journal for Numerical Methods in Fluids* 51.9-10 (July 2006), pp. 1097–1115. ISSN: 0271-2091, 1097-0363. DOI: 10.1002/fld.1151.

[82] T. D. Economon et al. “SU2: An Open-Source Suite for Multiphysics Simulation and Design”. en. In: *AIAA Journal* 54.3 (Mar. 2016), pp. 828–846. ISSN: 0001-1452, 1533-385X. DOI: 10.2514/1.J053813.

[83] M. Pini et al. “SU2: the Open-Source Software for Non-ideal Compressible Flows”. In: *Journal of Physics: Conference Series* 821 (Mar. 2017), p. 012013. ISSN: 1742-6588, 1742-6596. DOI: 10.1088/1742-6596/821/1/012013.

[84] M. Thol et al. “Fundamental equation of state correlation for hexamethyldisiloxane based on experimental and molecular simulation data”. en. In: *Fluid Phase Equilibria* 418 (June 2015), pp. 133–151. ISSN: 03783812. DOI: 10.1016/j.fluid.2015.09.047.

[85] M. B. Giles. “Nonreflecting boundary conditions for Euler equation calculations”. en. In: *AIAA Journal* 28.12 (Dec. 1990), pp. 2050–2058. ISSN: 0001-1452, 1533-385X. DOI: 10.2514/3.10521.

A

Mesh Convergence Study

To verify that the meshes used to discretise the two numerical domains are sufficiently refined to accurately predict the flow behaviour, a mesh convergence study is performed. Separate studies are performed for the infinite cascade and finite test section domains. Both studies follow the same approach. Three separate meshes are generated for the same numerical domain with increasing mesh refinement: coarse, medium, and fine. In each refinement step, the cell sizes at all boundaries of the numerical domain are reduced with the same ratio. In this way, the mesh refinement is applied evenly throughout the domain. Cell refinement is chosen such that the average cell width of the coarse and medium mesh is at least 1.33, to ensure a significant refinement step is made. The same holds for the refinement from medium to fine mesh. Since quadrilateral cells are used, the average cell width is determined by taking the square root of the average cell area, defined as the total domain area divided by the total number of cells.

Infinite Cascade Domain

Starting with the infinite cascade domain convergence study, Figure A.1 shows the average Mach number and flow angle at the outflow boundary for the three mesh refinements as a percentage difference compared to the fine mesh. A maximum difference of only 0.25% was found for the course mesh. In addition to the average flow properties, it is critical to evaluate whether the mesh is sufficiently refined to accurately resolve the shock waves in the flow behind the cascade. To analyse this, the local Mach number and the flow angle are plotted along the passage pitch at one chord length behind the blade in Figure A.2. Again, values are represented as percentage difference to the fine mesh. Here, more significant differences are found, with a maximum deviation in the coarse mesh of approximately 4%. Although this is still quite accurate, the medium mesh is chosen for the numerical analysis of the infinite cascade, since the computational demands of this mesh are still quite low.

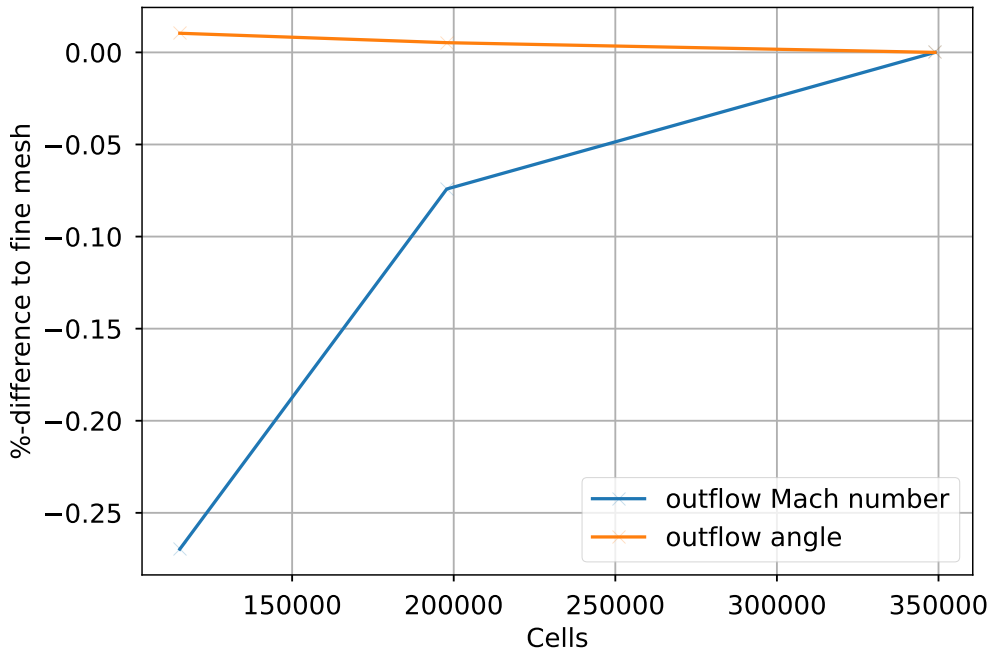

Figure A.1: Infinite cascade domain mesh convergence of the average Mach number and flow angle at the outflow boundary

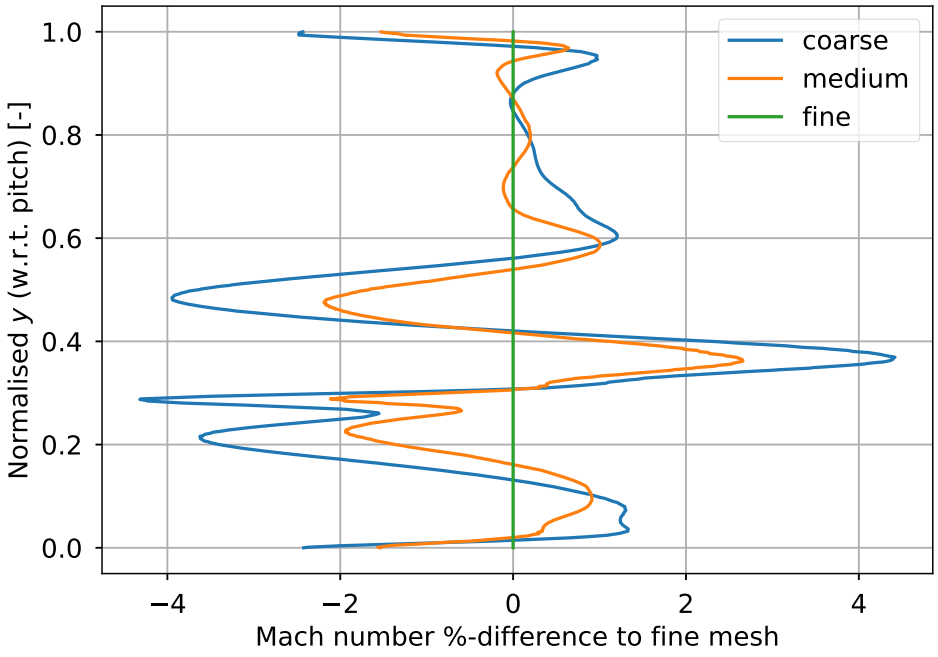

(a) Mach number

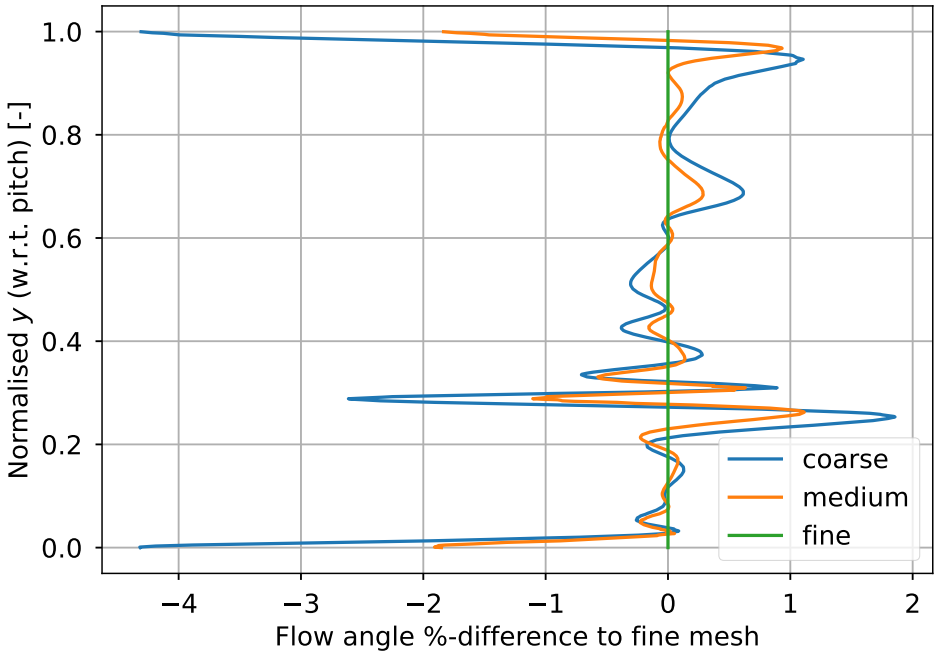

(b) Flow angle

Figure A.2: Infinite cascade domain mesh convergence of Mach number and flow angle along a line distribution across the passage, one chord length behind the blade

Finite Cascade Test Section Domain

For the finite cascade test section domain, the same approach is applied, where Figure A.3 shows the convergence of the average outlet properties and Figure A.4 shows the convergence of the local flow properties. Similarly to the infinite passage, the change in the average outflow properties is negligible, while the changes in the local properties remain small, reaching a maximum of approximately 5%. Again, the medium mesh is chosen for the numerical analysis since it shows some improvement over the coarse mesh and the computational requirements are within reason.

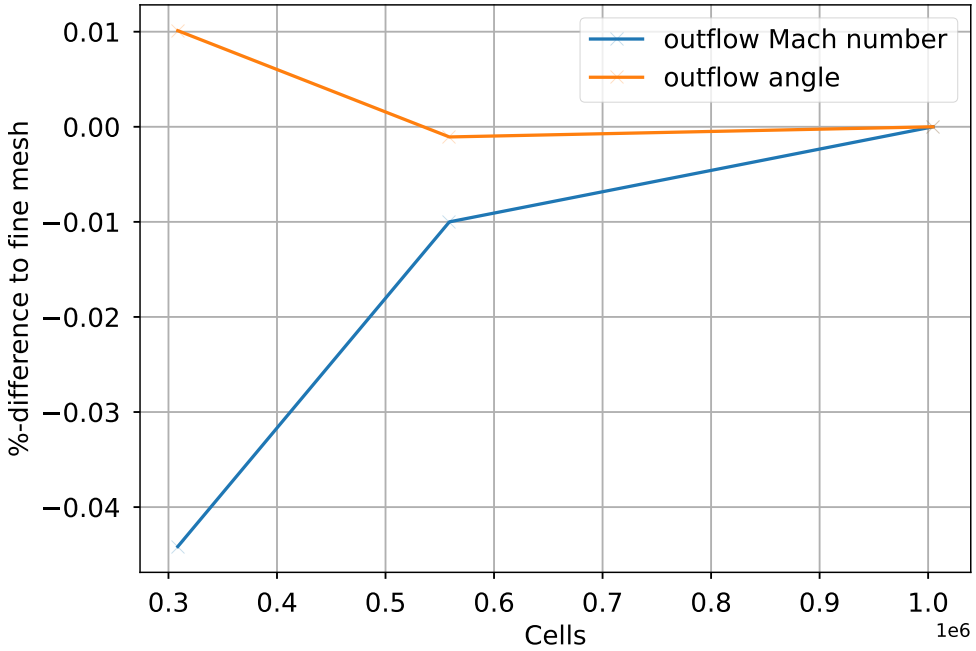

Figure A.3: Finite test section domain mesh convergence of the average Mach number and flow angle at the outflow boundary

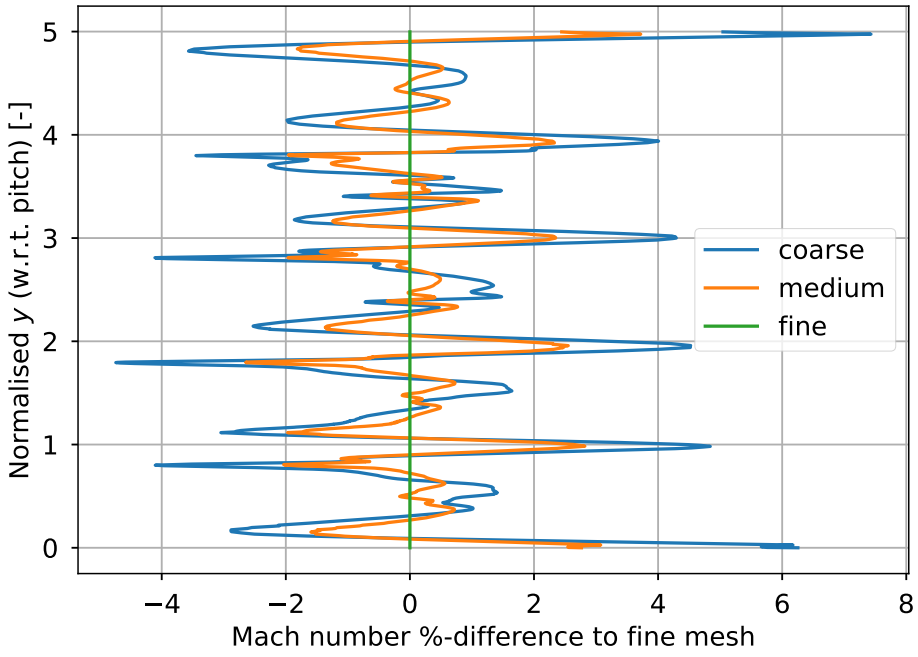

(a) Mach number

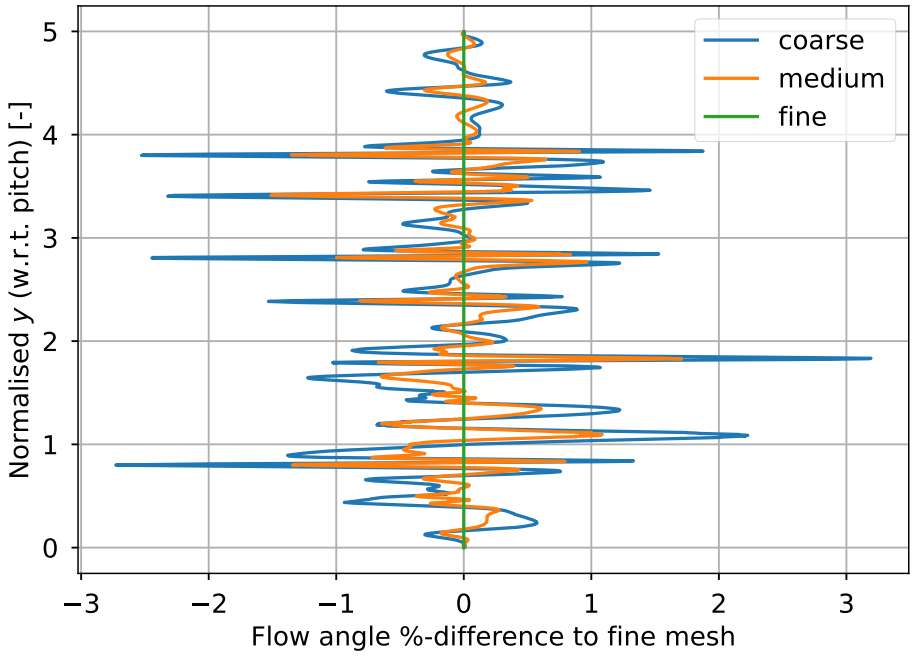

(b) Flow angle

Figure A.4: Finite test section domain mesh convergence of Mach number and flow angle along a line distribution across the passages, one chord length behind the blade

B

Example SU2 Configuration Files

First-Order Configuration

```
% Turbulent simulation (RANS)
SOLVER= RANS

% SA turbulence model
KIND_TURB_MODEL= SA
SA_OPTIONS= NONE

RESTART_SOL=NO
% Mach number (non-dimensional, based on the free-stream values)
MACH_NUMBER= 0.05

% Free-stream pressure
FREESTREAM_PRESSURE= 1.5558e+06

% Free-stream temperature
FREESTREAM_TEMPERATURE= 5.13513e+02

% Free-stream Turbulence Intensity
FREESTREAM_TURBULENCEINTENSITY = 0.1

% Free-stream Turbulent to Laminar viscosity ratio
FREESTREAM_TURB2LAMVISCRATIO = 100.0

FREESTREAM_OPTION= TEMPERATURE_FS

INIT_OPTION= TD_CONDITIONS

REF_DIMENSIONALIZATION= DIMENSIONAL

ITER=5000
CONV_RESIDUAL_MINVAL= -16

FLUID_MODEL= PR_GAS
FLUID_NAME= MM

% Ratio of specific heats (1.4 default and the value is hardcoded for the model
    STANDARD_AIR)
GAMMA_VALUE= 1.025
```

```
% Specific gas constant (287.058 J/kg*K default and this value is hardcoded for
    the model STANDARD_AIR)
GAS_CONSTANT= 51.2

% Critical Temperature (273.15 K by default)
CRITICAL_TEMPERATURE= 518.75

% Critical Pressure (101325.0 N/m^2 by default)
CRITICAL_PRESSURE= 1939000.0

% Acentric factor (0.035 (air))
ACENTRIC_FACTOR= 0.418

VISCOSITY_MODEL= CONSTANT_VISCOSITY

% Molecular Viscosity that would be constant (1.716E-5 by default)
MU_CONSTANT= 1.08144066e-05

% Sutherland Viscosity Ref (1.716E-5 default value for AIR SI)
MU_REF= 1.716E-5

% Sutherland Temperature Ref (273.15 K default value for AIR SI)
MU_T_REF= 273.15

% Sutherland constant (110.4 default value for AIR SI)
SUTHERLAND_CONSTANT= 110.4

CONDUCTIVITY_MODEL= CONSTANT_PRANDTL
PRANDTL_LAM= 7.87013030e-01
TURBULENT_CONDUCTIVITY_MODEL=CONSTANT_PRANDTL_TURB
PRANDTL_TURB= 7.87013030e-01

% Molecular Thermal Conductivity that would be constant (0.0257 by default)
THERMAL_CONDUCTIVITY_CONSTANT= 0.086

MARKER_HEATFLUX= (PRESSURESIDEWALL, 0.0, SUCTIONSIDEWALL, 0.0, BLADE1, 0.0, BLADE2
    , 0.0, BLADE3, 0.0, BLADE4, 0.0)
MARKER_GILES= (INFLOW, TOTAL_CONDITIONS_PT, 1.5558e+06, 5.13513e+02, 1.0, 0.0,
    0.0, 0.8, 0.8, OUTFLOW, STATIC_PRESSURE,2.5930e+05, 0.0, 0.0, 0.0, 0.0, 0.8,
    0.8)
SPATIAL_FOURIER=YES

% Kind of Average (ALGEBRAIC_AVERAGE, AREA_AVERAGE, MIXEDOUT_AVERAGE)
AVERAGE_PROCESS_KIND= MASSFLUX
MIXEDOUT_COEFF=(0.1, 1e-5, 15.0)
TURBOMACHINERY_KIND= AXIAL
TURBO_PERF_KIND=TURBINE
NUM_SPANWISE_SECTIONS= 1
% Specify ramp option for Outlet pressure (YES, NO) default NO
RAMP_OUTLET_PRESSURE= YES

% Parameters of the outlet pressure ramp (starting outlet pressure, updating-
    iteration-frequency, total number of iteration for the ramp)
RAMP_OUTLET_PRESSURE_COEFF= (1.5558e+06, 10, 200)

OBJECTIVE_FUNCTION=EFFICIENCY

MARKER_PLOTTING= (PRESSURESIDEWALL, SUCTIONSIDEWALL)
MARKER_MONITORING= (PRESSURESIDEWALL, SUCTIONSIDEWALL)
MARKER_TURBOMACHINERY= (INFLOW, OUTFLOW)
```

```
NUM_METHOD_GRAD= WEIGHTED_LEAST_SQUARES
CFL_NUMBER= 4
CFL_ADAPT= YES
CFL_ADAPT_PARAM= ( 0.99, 1.01, 1.0, 1000.0)

LINEAR_SOLVER= FGMRES
LINEAR_SOLVER_PREC= LU_SGS
LINEAR_SOLVER_ERROR= 1E-5
LINEAR_SOLVER_ITER= 20
CONV_NUM_METHOD_FLOW= ROE
MUSCL_FLOW= NO
ENTROPY_FIX_COEFF= 0.001
JST_SENSOR_COEFF= ( 0.5, 0.12 )
SLOPE_LIMITER_FLOW= VENKATAKRISHNAN
VENKAT_LIMITER_COEFF=0.5
TIME_DISCRE_FLOW= EULER_IMPLICIT
CONV_NUM_METHOD_TURB= SCALAR_UPWIND
MUSCL_TURB = NO
SLOPE_LIMITER_TURB= VENKATAKRISHNAN
TIME_DISCRE_TURB= EULER_IMPLICIT
CFL_REDUCTION_TURB= 0.01

MESH_FILENAME= /scratch/gwavandenheuve/run/mesh_files/fin_casc_2D_5pass_medium.
    cgns
MESH_FORMAT= CGNS
TABULAR_FORMAT= CSV
CONV_FILENAME= history_fin_casc_2D_5pass_nonid_medium_CEoS_firstorder
RESTART_FILENAME= restart_fin_casc_2D_5pass_nonid_medium_CEoS_firstorder
RESTART_ADJ_FILENAME= restart_adj.dat
SOLUTION_FILENAME=solution_EEoS_PINN
VOLUME_FILENAME= vol_solution_fin_casc_2D_5pass_nonid_medium_CEoS_firstorder
VOLUME_ADJ_FILENAME= adjoint
SURFACE_FILENAME =
    surf_solution_walls_fin_casc_2D_5pass_nonid_medium_CEoS_firstorder
SURFACE_ADJ_FILENAME= surface_adjoint
GRAD_OBJFUNC_FILENAME= of_grad.dat
OUTPUT_WRT_FREQ= 500
HISTORY_WRT_FREQ_INNER= 1
HISTORY_OUTPUT= (INNER_ITER, WALL_TIME, RMS_RES,EFFICIENCY,CFL_NUMBER,LINSOL_ITER,
    LINSOL_RESIDUAL,TURBO_PERF)
VOLUME_OUTPUT= (SOLUTION, PRIMITIVE, RESIDUAL, MPI)
OUTPUT_FILES=(RESTART)
```

Second-Order Configuration

```
% Turbulent simulation (RANS)
SOLVER= RANS

% SA turbulence model
KIND_TURB_MODEL= SA
SA_OPTIONS= NONE

RESTART_SOL=YES
% Mach number (non-dimensional, based on the free-stream values)
MACH_NUMBER= 0.05

% Free-stream pressure
FREESTREAM_PRESSURE= 1.5558e+06

% Free-stream temperature
FREESTREAM_TEMPERATURE= 5.13513e+02

% Free-stream Turbulence Intensity
FREESTREAM_TURBULENCEINTENSITY = 0.1

% Free-stream Turbulent to Laminar viscosity ratio
FREESTREAM_TURB2LAMVISCRATIO = 100.0

FREESTREAM_OPTION= TEMPERATURE_FS

INIT_OPTION= TD_CONDITIONS

REF_DIMENSIONALIZATION= DIMENSIONAL

ITER=40000
CONV_RESIDUAL_MINVAL= -16

FLUID_MODEL= PR_GAS
FLUID_NAME= MM

% Ratio of specific heats (1.4 default and the value is hardcoded for the model
    STANDARD_AIR)
GAMMA_VALUE= 1.025

% Specific gas constant (287.058 J/kg*K default and this value is hardcoded for
    the model STANDARD_AIR)
GAS_CONSTANT= 51.2

% Critical Temperature (273.15 K by default)
CRITICAL_TEMPERATURE= 518.75

% Critical Pressure (101325.0 N/m^2 by default)
CRITICAL_PRESSURE= 1939000.0

% Acentric factor (0.035 (air))
ACENTRIC_FACTOR= 0.418

VISCOSITY_MODEL= CONSTANT_VISCOSITY

% Molecular Viscosity that would be constant (1.716E-5 by default)
MU_CONSTANT= 1.08144066e-05

% Sutherland Viscosity Ref (1.716E-5 default value for AIR SI)
MU_REF= 1.716E-5
```

```
% Sutherland Temperature Ref (273.15 K default value for AIR SI)
MU_T_REF= 273.15

% Sutherland constant (110.4 default value for AIR SI)
SUTHERLAND_CONSTANT= 110.4

CONDUCTIVITY_MODEL= CONSTANT_PRANDTL
PRANDTL_LAM= 7.87013030e-01
TURBULENT_CONDUCTIVITY_MODEL=CONSTANT_PRANDTL_TURB
PRANDTL_TURB= 7.87013030e-01

% Molecular Thermal Conductivity that would be constant (0.0257 by default)
THERMAL_CONDUCTIVITY_CONSTANT= 0.086

MARKER_HEATFLUX= (PRESSURESIDEWALL, 0.0, SUCTIONSIDEWALL, 0.0, BLADE1, 0.0, BLADE2
    , 0.0, BLADE3, 0.0, BLADE4, 0.0)
MARKER_GILES= (INFLOW, TOTAL_CONDITIONS_PT, 1.5558e+06, 5.13513e+02, 1.0, 0.0,
    0.0, 0.8, 0.8, OUTFLOW, STATIC_PRESSURE,2.5930e+05, 0.0, 0.0, 0.0, 0.0, 0.8,
    0.8)
SPATIAL_FOURIER=YES

% Kind of Average (ALGEBRAIC_AVERAGE, AREA_AVERAGE, MIXEDOUT_AVERAGE)
AVERAGE_PROCESS_KIND= MASSFLUX
MIXEDOUT_COEFF=(0.1, 1e-5, 15.0)
TURBOMACHINERY_KIND= AXIAL
TURBO_PERF_KIND=TURBINE
NUM_SPANWISE_SECTIONS= 1
% Specify ramp option for Outlet pressure (YES, NO) default NO
RAMP_OUTLET_PRESSURE= NO

% Parameters of the outlet pressure ramp (starting outlet pressure, updating-
    iteration-frequency, total number of iteration for the ramp)
RAMP_OUTLET_PRESSURE_COEFF= (1.5558e+06, 10, 200)

OBJECTIVE_FUNCTION=EFFICIENCY

MARKER_PLOTTING= (PRESSURESIDEWALL, SUCTIONSIDEWALL)
MARKER_MONITORING= (PRESSURESIDEWALL, SUCTIONSIDEWALL)
MARKER_TURBOMACHINERY= (INFLOW, OUTFLOW)

NUM_METHOD_GRAD= WEIGHTED_LEAST_SQUARES
CFL_NUMBER= 4
CFL_ADAPT= YES
CFL_ADAPT_PARAM= ( 0.99, 1.01, 1.0, 1000.0)

LINEAR_SOLVER= FGMRES
LINEAR_SOLVER_PREC= LU_SGS
LINEAR_SOLVER_ERROR= 1E-5
LINEAR_SOLVER_ITER= 20
CONV_NUM_METHOD_FLOW= JST
MUSCL_FLOW= NO
ENTROPY_FIX_COEFF= 0.001
JST_SENSOR_COEFF= ( 0.5, 0.12 )
SLOPE_LIMITER_FLOW= VENKATAKRISHNAN
VENKAT_LIMITER_COEFF=0.5
TIME_DISCRE_FLOW= EULER_IMPLICIT
CONV_NUM_METHOD_TURB= SCALAR_UPWIND
MUSCL_TURB = NO
SLOPE_LIMITER_TURB= VENKATAKRISHNAN
TIME_DISCRE_TURB= EULER_IMPLICIT
```

```
CFL_REDUCTION_TURB= 0.01

MESH_FILENAME= /scratch/gwavandenheuve/run/mesh_files/fin_casc_2D_5pass_medium.
    cgns
MESH_FORMAT= CGNS
TABULAR_FORMAT= CSV
CONV_FILENAME= history_fin_casc_2D_5pass_nonid_medium_CEoS_secondorder
RESTART_FILENAME= restart_fin_casc_2D_5pass_nonid_medium_CEoS_secondorder
RESTART_ADJ_FILENAME= restart_adj.dat
SOLUTION_FILENAME=restart_fin_casc_2D_5pass_nonid_medium_CEoS_firstorder
VOLUME_FILENAME= vol_solution_fin_casc_2D_5pass_nonid_medium_CEoS_secondorder
VOLUME_ADJ_FILENAME= adjoint
SURFACE_FILENAME =
    surf_solution_walls_fin_casc_2D_5pass_nonid_medium_CEoS_secondorder
SURFACE_ADJ_FILENAME= surface_adjoint
GRAD_OBJFUNC_FILENAME= of_grad.dat
OUTPUT_WRT_FREQ= 500
HISTORY_WRT_FREQ_INNER= 1
HISTORY_OUTPUT= (INNER_ITER, WALL_TIME, RMS_RES,EFFICIENCY,CFL_NUMBER,LINSOL_ITER,
    LINSOL_RESIDUAL,TURBO_PERF)
VOLUME_OUTPUT= (SOLUTION, PRIMITIVE, RESIDUAL, MPI)
OUTPUT_FILES=(RESTART, TECPLOT_ASCII, SURFACE_TECPLOT_ASCII)
```